Appendix A

Šimeček, J.; Zemek, O.; Hermann, P.; Wester, H.-J.; Notni, J. A Monoreactive Bifunctional Triazacyclononane Phosphinate Chelator with High Selectivity for Gallium-68. *ChemMedChem* **2012**, *7* (8), 1375–1378. https://doi.org/10.1002/cmdc.201200261.

Appendix A

DOI: 10.1002/cmdc.201200261

A Monoreactive Bifunctional Triazacyclononane Phosphinate Chelator with High Selectivity for Gallium-68

Jakub Šimeček,[a, b] Ondřej Zemek,[b] Petr Hermann,[b] Hans-Jürgen Wester,[a] and Johannes Notni*[a]

In recent years, the significance of the radioisotope ^{68}Ga ($t_{1/2}$ = 68 min; $E_{\beta^+,max}$ = 1.89 MeV) for positron emission tomography (PET) has been widely recognized,[1] particularly in light of the success of ^{68}Ga-labeled somatostatin analogues, such as ^{68}Ga-DOTATOC, in neuroendocrine tumor imaging.[2] The main advantages of ^{68}Ga are easy handling, quick and uncomplicated labeling procedures, and cyclotron-independent on-site production in radioisotope generators. In such devices, ^{68}Ga is constantly generated by the decay of ^{68}Ge ($t_{1/2}$ = 270.8 days, EC), similar to ^{99m}Tc production in ^{99}Mo/^{99m}Tc generators. This facilitates the implementation of global coverage of PET, an imaging modality which, in view of its high sensitivity and spatial resolution relative to scintigraphy, is considered an extremely valuable tool in functional molecular imaging and personalized healthcare.

Targeted ^{68}Ga radiopharmaceuticals, e.g., for peptide receptor imaging, are usually bioconjugates that consist of one or more bioactive vectors and a chelating unit for $^{68}Ga^{3+}$ binding. As the inherent complexation properties of the chelator readily determine the labeling efficiency and thus the specific activity of the tracers, chelator optimization is a pivotal issue in tracer improvement.[3]

About two decades ago, 1,4,7-triazacyclononanes with phosphinic acid side chains were found to be good chelators for various metal ions, including Ga^{3+}.[4] More recently, our research groups reported a novel bifunctional triazacyclononane triphosphinic acid chelator (TRAP), which complexes $^{68}Ga^{3+}$ much more efficiently than the established bifunctional chelator NODAGA and also constitutes an ideal framework for the preparation of trimeric bioconjugates.[5–8] Pursuing this approach, we devised the related structure NOPO (see Scheme 1), which possesses only one site for bioconjugation. It is therefore ideally suited for synthetic tasks in which strictly monoconjugation is desired, such as for conjugates of somatostatin receptor agonists which internalize into cells after binding. NOPO therefore perfectly complements the portfolio of TRAP-like chelators in terms of synthetic strategy.

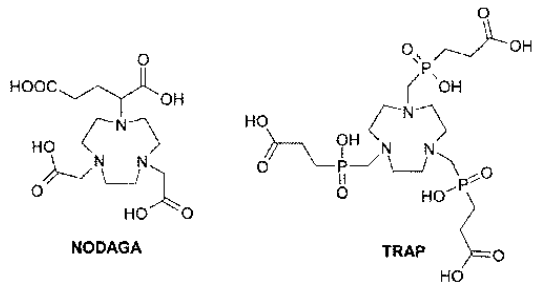

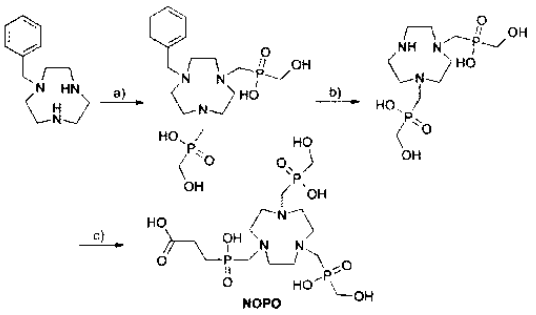

Scheme 1. Synthesis of the NOPO chelator. *Reagents and conditions:* a) H_3PO_2, H_2C=O, 6 M HCl, RT, 24 h; b) Pd/C in H_2O, H_2, RT, 12 h; c) (2-carboxyethyl)phosphinic acid, H_2C=O, 6 M HCl, 70 °C, 24 h. Overall yield: 18–30 %.

NOPO was synthesized by a multistep Moedritzer–Irani reaction,[9] as shown in Scheme 1 (see the Supporting Information for details). As expected, owing to the lower basicity of phosphinate-containing ligands relative to those featuring carboxylates, the stability constant of the $[Ga(NOPO)]^-$ complex ($\log K$ = 25.01, determined by potentiometry) is lower than that of [Ga(NOTA)] ($\log K$ = 29.60),[7] but similar to that of $[Ga(TRAP)]^{3-}$ ($\log K$ = 26.24).[6] Nevertheless, the $[Ga(NOPO)]^-$ complex was found to possess pronounced kinetic inertness against acid-promoted decomplexation. No disintegration of the complex was observed in 6 M $HClO_4$ over a period of three months at room temperature.

For proof-of-concept studies, two well-investigated peptidic receptor ligands, cyclo(RGDfK) ("RGDfK", targeting of $\alpha_v\beta_3$ integrins)[10] and Nal-octreotide ("NOC", targeting of somatostatin receptor subtypes 2 and 5),[11] were conjugated to the carboxylic acid moiety of NOPO by amide formation (see also Supporting Information). Because chelator conjugates of these targeting groups are very well investigated, their choice allows comparison with a sound basis of prior data. Conjugation of NOPO is particularly convenient, as no protection of the phosphinate moieties is required during the reaction.

[a] J. Šimeček, Prof. Dr. H.-J. Wester, Dr. J. Notni
Pharmazeutische Radiochemie, Technische Universität München
Walther-Meißner-Str. 3, 85748 Garching (Germany)
E-mail: johannes.notni@tum.de
Homepage: http://www.prc.ch.tum.de

[b] J. Šimeček, O. Zemek, Prof. Dr. P. Hermann
Department of Inorganic Chemistry
Faculty of Science, Charles University in Prague
Hlavova 2030, 12840 Prague 2 (Czech Republic)

Supporting information for this article is available on the WWW under http://dx.doi.org/10.1002/cmdc.201200261.

CHEMMEDCHEM

ChemPubSoc Europe

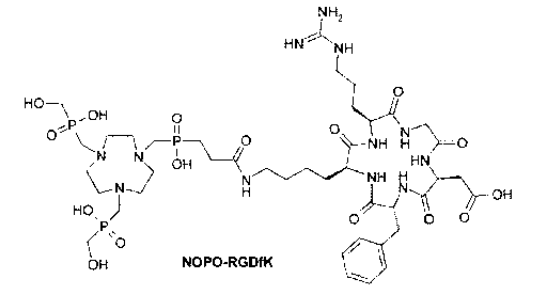

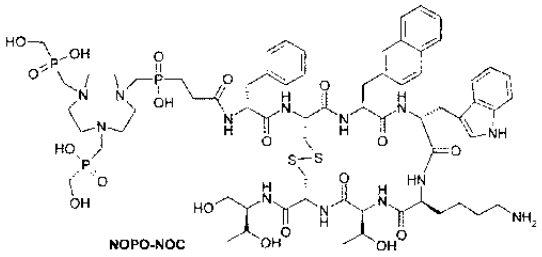

In line with previous studies that outlined the superior ^{68}Ga labeling efficiency of 1,4,7-triazacyclononane phosphinate ligands relative to their carboxylate analogues,[5,6] NOPO was shown to incorporate ^{68}Ga at very low ligand concentrations, which is typical for TRAP-type chelators. Moreover, bioconjugation does not significantly change ^{68}Ga labeling performance; Figure 1 shows that the radioactivity incorporation into NOPO and NOPO–RGDfK is essentially identical within the margins of error. For both compounds, near-quantitative (>95%) labeling can be achieved at chelator concentrations as low as 0.1 μM. ^{68}Ga-NOPO–RGDfK showed no loss of activity, neither over a period of 3 h in PBS or 0.25 M EDTA at 37 °C, nor in vivo.

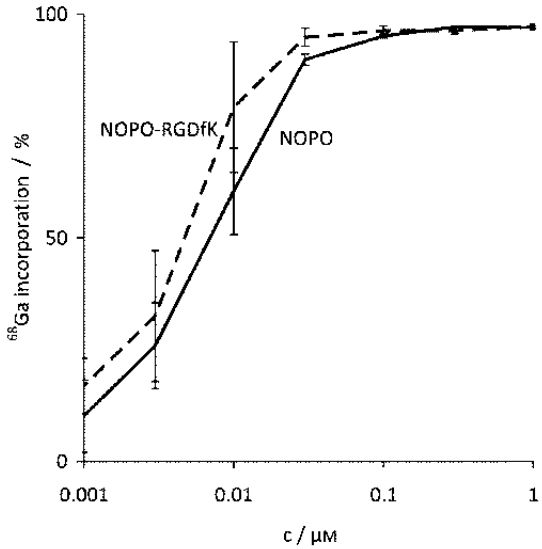

Figure 1. Radioactivity incorporation (%) by NOPO and NOPO–RGDfK as functions of precursor concentration (T = 95 °C, t = 5 min, pH 2.8).

Due to competition with $^{68}Ga^{3+}$ for the chelator, contamination of ^{68}Ge/^{68}Ga generator eluates with various metal ions originating from the column matrix or the eluents was recognized earlier as being responsible for considerably decreased radiochemical yields during ^{68}Ga labeling. In view of the very similar coordination behavior of Ga^{3+} and Fe^{3+}, the latter ion is considered particularly problematic. Moreover, the presence of Zn^{2+} in the eluate cannot be circumvented, as ^{68}Zn is constantly formed as a stable daughter of ^{68}Ga. To avoid potential problems caused by these metal ion contaminants during subsequent complexation, various strategies for eluate purification, i.e., removal of non-Ga^{3+} cations, have been developed.[12–14] However, Figure 2 shows a pronounced selectivity

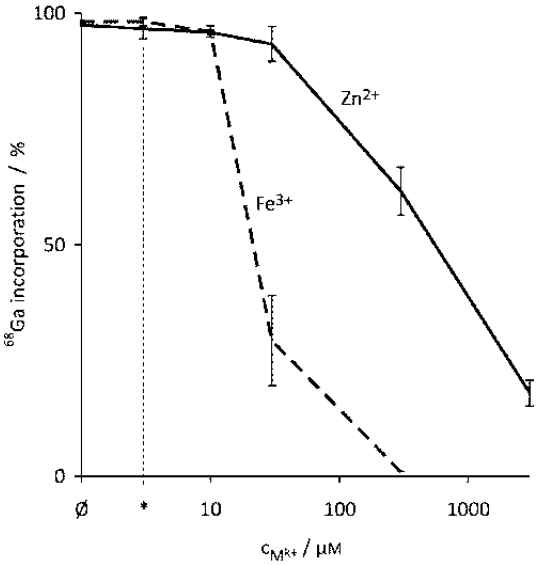

Figure 2. Radioactivity incorporation (%) by NOPO as a function of concentration of added metal ions (c_{NOPO} = 3 μM, T = 95 °C, t = 5 min, pH 3.3); Ø: none added; *: [NOPO]/[M^{k+}] = 1 (3 μM).

of NOPO for Ga^{3+}. Almost quantitative ^{68}Ga binding is observed even in the presence of 30 μM Zn^{2+} or 10 μM Fe^{3+} (i.e., 10 and 3.3 equiv of NOPO, respectively), which exceeds by far the single-digit ppm concentration range in which these ions are maximally present in generator eluates.[15–17] For NOPO, the usual contents of Fe^{3+} and particularly Zn^{2+} in eluates can therefore be considered irrelevant, rendering the removal of these ions unnecessary.

GMP-compliant production of radiopharmaceutical formulations of ^{68}Ga-NOPO–peptides was performed in a fully automated process as described before.[5,18] Exceptionally high specific activities can be achieved reproducibly; for example, labeling reactions with 100 pmol NOPO–RGDfK and 970±60 MBq ^{68}Ga (≈10 pmol) yielded formulations of ^{68}Ga-NOPO–RGDfK

Appendix A

with radiochemical yields of 77.2±2.1% (decay-corrected), while specific activities (calculated for $t=30$ min after the start of synthesis)[19] reached 5600±500 GBq μmol^{-1}. For a typical dose used in small-animal imaging, such as 15 MBq, this results in a total injected amount of both labeled and unlabeled NOPO–RGDfK of ~2.7 pmol or 3.1 ng, which is impressively low. Accordingly, a hypothetical patient dose of 185 MBq (5 mCi) would contain only ~33 pmol or 38 ng of RGDfK conjugates. ^{68}Ga-NOPO–peptides can therefore be considered ideal radiotracers and even meet concentration requirements far below the microdosing approach. Due to their extremely high specific activity without the need for a purification step, NOPO–peptide conjugates allow convenient adjustment to an ideal specific activity by the addition of cold reference and thus are very useful for studies of the influence of the specific activity of ^{68}Ga-labeled peptides on specific tracer uptake in vivo.

The suitability of ^{68}Ga-NOPO–peptides for molecular imaging was proven in preliminary PET studies. ^{68}Ga-NOPO–RGDfK was used for mapping of $\alpha_v\beta_3$ integrin expression in a nude mouse bearing human melanoma xenografts M21 (high $\alpha_v\beta_3$ expression) and M21L (low $\alpha_v\beta_3$ expression) on the right and left shoulders, respectively. Figure 3 (left) shows that M21 is clearly delineated in the PET image. In accordance with previous studies, we also observed considerable uptake in the abdominal region.[5,18,20] However, all of this uptake was shown to be integrin-specific, as nearly complete blocking was achieved by co-injection of excess NOPO–RGDfK (5 mg kg^{-1}; see Supporting Information figure S5). PET imaging of an AR42J-xenografted mouse using ^{68}Ga-NOPO–NOC (Figure 3, right) shows low background and high tracer uptake in the tumor, while only insignificant amounts of activity remain in the kidneys. Again, specificity of binding was proven by complete extinction of tumor uptake by administration of a blocking dose of 5 mg kg^{-1} NOPO–NOC (see Supporting Information figure S6).

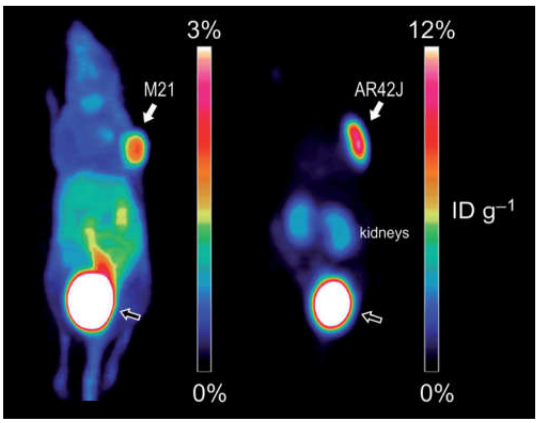

Figure 3. PET images (MIP, 75 min p.i.) of nude mouse tumor xenografts. Left: ^{68}Ga-NOPO–RGDfK (M21 human melanoma); right: ^{68}Ga-NOPO–NOC (AR42J rat pancreas carcinoma). Accumulation of activity is observed in the urinary bladder (indicated by outline arrows) due to renal excretion.

We conclude that our novel chelator NOPO is highly appropriate for the preparation of ^{68}Ga PET radiopharmaceuticals. Its radiochemical properties, namely excellent efficiency and selectivity in $^{68}Ga^{3+}$ complexation, are of outstanding value for clinical daily practice. In addition, due to the eradication of undesired pharmacological or saturation effects, the high specific activity achievable for NOPO peptides is of high importance for preclinical studies in rodents. In view of the convincing results of the proof-of-concept PET study, we assume that NOPO has a bright future in the design of next-generation monomeric ^{68}Ga PET tracers.

Acknowledgements

Financial support by the Grant Agency of Charles University (Grant No. 19310), the Ministry of Education of the Czech Republic (Grant No. MSM0021620857), the Deutsche Forschungsgemeinschaft (SFB 824, Project Z1), and EU COST Actions CM0802 and TD1004, is gratefully acknowledged. The Authors thank Jana Havlíčková and Jan Plutnar (Charles University) for potentiometry measurements and recording of NMR spectra, respectively.

Keywords: bioconjugates · gallium-68 · macrocyclic ligands · phosphinic acid · positron emission tomography

[1] a) C. Decristoforo, R. D. Pickett, A. Verbruggen, *Eur. J. Nucl. Med. Mol. Imaging* **2012**, *39*, S31–S40; b) I. Velikyan, *Med. Chem.* **2011**, *7*, 338–372.
[2] a) W. A. P. Breeman, E. de Blois, H. S. Chan, M. Konijnenberg, D. J. Kwekkeboom, E. P. Krenning, *Semin. Nucl. Med.* **2011**, *41*, 314–321; b) M. Fani, J. P. André, H. R. Mäcke, *Contrast Media Mol. Imaging* **2008**, *3*, 67–77.
[3] J. Notni, *Nachr. Chem.* **2012**, *6*, 645–649.
[4] a) K. Bazakas, I. Lukeš, *J. Chem. Soc. Dalton Trans.* **1995**, 1133–1137; b) E. Cole, D. Parker, G. Ferguson, J. F. Gallagher, B. Kaitner, *J. Chem. Soc. Chem. Commun.* **1991**, 1473–1475; c) C. J. Broan, E. Cole, K. J. Jankowski, D. Parker, K. Pulukkody, B. A. Boyce, N. R. A. Beeley, K. Millar, A. T. Millican, *Synthesis* **1992**, 63–68; d) C. J. Broan, K. J. Jankowski, R. Kataky, D. Parker, *J. Chem. Soc. Chem. Commun.* **1990**, 1738–1739; e) E. Cole, R. C. B. Copley, J. A. K. Howard, D. Parker, G. Ferguson, J. F. Gallagher, B. Kaitner, A. Harrison, L. Royle, *J. Chem. Soc. Dalton Trans.* **1994**, 1619–1625; f) M. I. M. Prata, A. C. Santos, C. F. G. C. Geraldes, J. J. P. de Lima, *Nucl. Med. Biol.* **1999**, *26*, 707–710.
[5] J. Notni, J. Šimeček, P. Hermann, H. J. Wester, *Chem. Eur. J.* **2011**, *17*, 14718–14722.
[6] J. Notni, P. Hermann, J. Havlíčková, J. Kotek, V. Kubíček, J. Plutnar, N. Loktionova, P. J. Riss, F. Rösch, I. Lukeš, *Chem. Eur. J.* **2010**, *16*, 7174–7185.
[7] J. Šimeček, M. Schulz, J. Notni, J. Plutnar, V. Kubíček, J. Havlíčková, P. Hermann, *Inorg. Chem.* **2012**, *51*, 577–590.
[8] J. Notni, J. Plutnar, H. J. Wester, *EJNMMI Res.* **2012**, *2*, 13.
[9] K. Moedritzer, R. R. Irani, *J. Org. Chem.* **1966**, *31*, 1603–1607.
[10] M. Schottelius, B. Laufer, H. Kessler, H. J. Wester, *Acc. Chem. Res.* **2009**, *42*, 969–980.
[11] D. Wild, J. S. Schmitt, M. Ginj, H. R. Mäcke, B. F. Bernard, E. Krenning, M. de Jong, S. Wenger, J. C. Reubi, *Eur. J. Nucl. Med. Mol. Imaging* **2003**, *30*, 1338–1347.
[12] K. P. Zhernosekov, D. V. Filosofov, R. P. Baum, P. Aschoff, H. J. Adrian, H. Bihl, A. A. Razbash, M. Jahn, M. Jennewein, F. Rösch, *J. Nucl. Med.* **2007**, *48*, 1741–1748.

CHEMMEDCHEM

ChemPubSoc Europe

[13] G. J. Meyer, H. R. Mäcke, J. Schuhmacher, W. H. Knapp, M. Hofmann, *Eur. J. Nucl. Med. Mol. Imaging* **2004**, *31*, 1097 – 1104.
[14] N. S. Loktionova, A. N. Belozub, D. V. Filosofov, K. P. Zhernosekov, T. Wagner, A. Türler, F. Rösch, *Appl. Radiat. Isot.* **2011**, *69*, 942 – 946.
[15] E. de Blois, H. S. Chan, C. Naidoo, D. Prince, E. P. Krenning, W. A. P. Breeman, *Appl. Radiat. Isot.* **2011**, *69*, 308 – 315.
[16] W. A. P. Breeman, M. de Jong, E. de Blois, B. F. Bernard, M. Konjinenberg, E. P. Krenning, *Eur. J. Nucl. Med. Mol. Imaging* **2005**, *32*, 478 – 485.
[17] D. D. Rossouw, W. A. P. Breeman, *Appl. Radiat. Isot.* **2012**, *70*, 171 – 175.
[18] K. Pohle, J. Notni, J. Bussemer, H. Kessler, M. Schwaiger, A. J. Beer, *Nucl. Med. Biol.* **2012**, DOI: 10.1016/j.nucmedbio.2012.02.006.
[19] Specific activities were calculated from molar amounts of precursor and product activity, as described previously.[5,18] As our ^{68}Ga tracer production logistics commonly allow tracer administration 30 min after the start of synthesis, specific activities are given for that time point to provide realistic data.
[20] R. A. Dumont, F. Deininger, R. Haubner, H. R. Maecke, W. A. Weber, M. Fani, *J. Nucl. Med.* **2011**, *52*, 1276 – 1284.

Received: May 21, 2012
Published online on June 12, 2012

Appendix A

CHEMMEDCHEM
Chemistry & Drug Discovery

Supporting Information

A Monoreactive Bifunctional Triazacyclononane Phosphinate Chelator with High Selectivity for Gallium-68

Jakub Šimeček,[a, b] Ondřej Zemek,[b] Petr Hermann,[b] Hans-Jürgen Wester,[a] and Johannes Notni*[a]

cmdc_201200261_sm_miscellaneous_information.pdf

Table of Contents

Appendix A

1. Materials & Methods

Instrumentation: NMR spectra were recorded using Varian Unity Inova (400 MHz), VNMRS (300 MHz) or Bruker Avance-III (600 MHz) NMR systems. ^{1}H and ^{13}C NMR shifts are referenced to *tert*-butanol signal (internal standard; 1.25 and 30.29 ppm, respectively), ^{31}P NMR shifts are referenced relative to 85 % aq. H_3PO_4 solution as external standard (0.0 ppm) and ^{71}Ga NMR shifts are referenced to 0.2 M aq. $[Ga(OH)_4]^-$ (222 ppm) or $[Ga(H_2O)_6]^{3+}$ (0 ppm) solutions as external standards. ESI-MS spectra in positive and/or negative modes were measured on Bruker Esquire 3000 or Varian Ion-trap 500 spectrometers. Ultrafiltration was performed using an Amicon (Millipore) apparatus (50 mL stirred cell model 8050, CDS10 selector valve and RC800 mini-reservoir), in combination with cellulose acetate membranes (Ultracel, filter code YC05, cut-off 500 Da). Elemental analysis was performed using a Perkin Elmer CHN/S Elemental analyser 2400 II. The thermodynamic stability constant of the $[Ga(NOPO)]^-$ complex was determined by potentiometry as described before.[1]

Starting materials: The solvents and reagents used for syntheses were commercially available. 1-Benzyl-1,4,7-triazacyclononane was purchased from Chematech (Dijon, France). (2-carboxy-ethyl)phosphinic acid was prepared as described before.[2] Peptides were synthesized according to standard Fmoc protocol on solid phase support.

HPLC, TLC: Bioconjugates were purified using preparative HPLC, consisting of a Sykam system with two separate solvent pumps, on a YMC C18ec column (250 × 30 mm, 5 µm particle size) and UV detection (220 nm and 254 nm), flow rate 20 mL/min. Analytical HPLC was performed using a Sykam HPLC system with low-pressure gradient mixer, equipped with a Nucleosil C18-RP column (100 × 4.6 mm, 5 µm particle size) and UV detection (220 nm), flow rate 1 mL/min. Radio-HPLC was performed on a Sykam system using a Chromolith column (Merck, 100 × 4.6 mm) with radioactivity and UV detection (220 nm), flow rate 2 mL/min, eluents were water and acetonitrile, both containing 0.1 % TFA (isocratic elution with 3 % MeCN for 2 min followed by a gradient to 60 % MeCN in 6 min and isocratic elution with 95 % MeCN for 3 min). Radio-TLC was done on silica gel 60 with 0.1 M aqueous sodium citrate as mobile phase (TLC1) and on Varian silica impregnated chromatography paper with a 1:1 (v/v) mixture of 1 M aqueous NH_4OAc and MeOH as mobile phase (TLC2).

2. Synthesis of NOPO and its gallium(III) complex

1,4,7-triazacyclononane-1,4-bis[methylene(hydroxymethyl)phosphinic acid]-7-[methylene(2-carboxyethyl)phosphinic acid] (NOPO): 1-benzyl-1,4,7-triazacyclononane (1.28 g, 5.88 mmol) and paraformaldehyde (0.44 g, 14.7 mmol) were suspended in 50 % aq. H_3PO_2 (6.60 mL, 60.3 mmol) and water (5 mL). Reaction mixture was stirred for 12 h at ambient temperature and then purified on cationic exchanger (Dowex 50 in H^+ cycle). The column was washed with water and the triazacyclononane-containing compounds were eluted with a 1:1 (v/v) mixture of 6 M aq. HCl and EtOH. The eluate was evaporated and crude product was dissolved in 6 M aq. HCl (20 mL), paraformaldehyde (0.73 g, 24.3 mmol) was added and solution was refluxed for 5 h. Then the solvent was evaporated and the residue was purified on silicagel with a 3:1:2 mixture (by volumes) of MeCN, MeOH, and NH_4OH as mobile phase. Fractions containing pure product (as monitored by ^{31}P NMR spectroscopy) were collected and the eluent evaporated in vacuo to give 1.20 g of a dark-yellow solid. This was dissolved in water (5 mL), 10 % Pd/C (0.10 g) was added and the mixture was stirred under H_2 atmosphere at ambient temperature for 12 h. ^{31}P NMR reaction monitoring showed that after this time, deprotection was quantitative. The catalyst was filtered off with a fine glass frit, and the solvent evaporated in vacuo, resulting in 0.90 g of crude intermediate. This was dissolved in 6 M aq. HCl, 2-(carboxyethyl)phosphinic acid (0.53 g, 3.80 mmol) was added, and the mixture heated to 75 °C. Paraformadehyde (0.35 g, 11.7 mmol) was added in small portions during 24 h. Then, the solvent was removed in vacuo, the residue repeatedly co-evaporated with water in order to remove HCl, and loaded on cation exchange resin (Dowex 50 in H^+ cycle). The resin was eluted with water and the fractions containing the product were identified by ^{31}P NMR. These were collected, the eluent removed in vacuo, the residue dissolved again in water and lyophilized, yielding 0.53 g (18 %) of a microcrystalline, pale yellow solid (NOPO·0.6 H_2O).

^1H NMR (600 MHz, D_2O), δ/ppm: 3.58 (s, ring C$\underline{H}_2$, 4H), 3.61 (s, ring C$\underline{H}_2$, 2H), 3.495 (d, $^2J_{PH}$ = 6.4 Hz, N–C$\underline{H}_2$–P, 2H), 3.83 (d, $^2J_{PH}$ = 5.8 Hz, P–C$\underline{H}_2$–OH, 4H), 3.50 (d, $^2J_{PH}$ = 5.5 Hz, N–C$\underline{H}_2$–P, 4H), 2.09 (m, P–C$\underline{H}_2$–CH_2, 2H), 2.69 (m, P–CH_2–C$\underline{H}_2$, 2H); $^{13}C\{^1H\}$ NMR (150 MHz, D_2O), δ/ppm: 52.29 (s, ring $\underline{C}H_2$, 2C), 52.39 (s, ring $\underline{C}H_2$, 4C), 53.82 (d, $^1J^{PC}$ = 86.6 Hz, N–$\underline{C}H_2$–P, 2C), 60.20 (d, $^1J_{PC}$ = 112.9 Hz, P–$\underline{C}H_2$–OH, 2C), 55.38 (d, $^1J_{PC}$ = 90.4 Hz, N–$\underline{C}H_2$–P, 1C), 25.51 (d, $^1J_{PC}$ = 94.7 Hz, P–$\underline{C}H_2$–CH_2, 1C), 27.52 (d, $^1J_{PC}$ = 3.5 Hz, P–CH_2–$\underline{C}H_2$, 1C), 177.91 (d, $^3J_{PC}$ = 12.6 Hz, C=O, 1C); $^{31}P\{^1H\}$ NMR (121 MHz, D_2O), δ/ppm: 34.7 (s, 2P), 40.3 (s, 1P). ESI-MS(+): m/z = 496 $(M+H^+)^+$. Elemental analysis calculated (%) for $C_{14}H_{32}N_3O_{10}P_3$·0.6 H_2O: C 33.22, H 6.61, N 8.30; found C 32.31, H 6.67, N 8.22.

[Ga(NOPO)]$^-$ solution for NMR: Solutions of NOPO and $Ga(NO)_3$ (2 mL of 2 mM of each) were mixed in NMR tube. $^{31}P\{^1H\}$ NMR (121.4 MHz, D_2O), δ/ppm: 37.3 (s, $\underline{P}$–CH_2–OH, 2P), 41.6 (s, $\underline{P}$–

$(CH_2)_2CO_2H$, 1P). ^{71}Ga NMR (122 MHz, D_2O), δ/ppm: 136 (s). ESI-MS(–): *m/z* = 560 $(M–H^+)^-$, 596 $(M+K^+–2H^+)^-$. ESI-MS(+): *m/z* = 562 $(M+H^+)^+$, 584 $(M+Na^+)^+$, 600 $(M+K^+)^+$.

3. Synthesis of the NOPO peptide conjugates

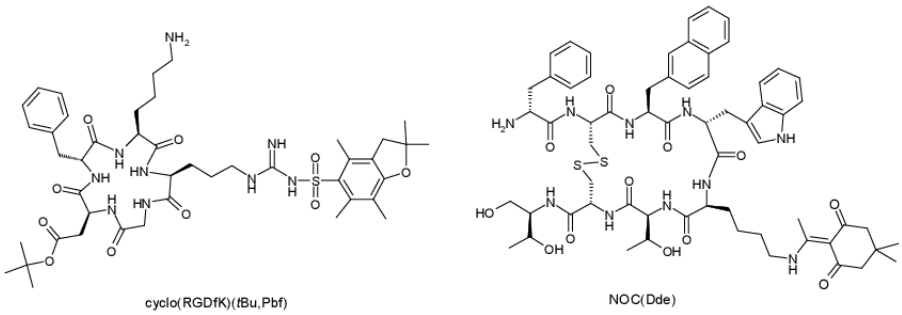

Figure S1: Structures of the protected peptides used as starting compounds for synthesis of conjugates.

NOPO-RGDfK: NOPO·0.6 H_2O (24.8 mg, 49 µmol) and cyclo(RGDfK)(Pbf,*t*Bu) (50.0 mg, unknown TFA content, ca. 50 µmol) were dissolved in dry DMSO (0.5 mL), and DIPEA (86.0 µL, 63.8 mg, 494 µmol) was added. Then HATU (57.2 mg, 150 µmol) was added and the solution was stirred for 10 min at ambient temperature. The precipitate obtained by addition of the reaction mixture to sat. aq. NaCl solution was separated by centrifugation, the solid was dissolved in water and subjectied to diafiltration with water (ca. 200 mL). The retentate was lyophilized, and TFA (80 %, 1 mL) was added for removal of acid-sensititive protecting groups Pbf and *t*Bu. The product was precipitated by addition into diethyl ether (10 mL), the precipitate centrifuged off and purified by preparative HPLC (gradient: 27 % to 37 % MeCN in water, both containing 0.1 % TFA, in 30 min). Fractions containing the product were collected, the organic solvent evaporated in vacuo and the remaining aqueous solution lyophilized to give 21 mg (40 %) of NOPO-RGDfK.

Analytical HPLC: gradient 20 % to 80 % MeCN in water, both containing 0.1 % TFA, in 24 min. t_R = 6.5 min. ESI-MS(+): *m/z* =1081 $(M+H^+)^+$, ESI-MS(–): *m/z* = 1079 $(M–H^+)^-$.

[Ga(NOPO-RGDfK)] solution: Solutions of $Ga(NO_3)_3$ and NOPO-RGDfK (0.1 mL of 2 mM of each) were mixed. The complex was identified by ESI-MS(+): *m/z* = 1147 $(M+H^+)$.

NOPO-NOC: This compound was prepared as described for NOPO-RGDfK, starting out from NOC(Dde) (10.0 mg, unknown TFA content, ca 7.5 µmol), NOPO (5.5 mg, 11.1 µmol) and using DMSO (0.5 mL), DIPEA (14.3 mg, 19.3 µL, 111 µmol) and HATU (21.1 mg, 55.5 µmol). Deprotection (removal of Dde) was done with 2 % hydrazine in DMF. Purification was done by preparative HPLC (gradient 25 % to 45 % MeCN in water, both containing 0.1 % TFA, in 60 min), yield 5.9 mg (51 %).

Analytical HPLC: gradient 20 % to 60 % MeCN in water, both containing 0.1 % TFA, in 16 min. t_R = 8.5 min. ESI-MS(+): *m/z* = 1528 $(M–H_2O+H^+)^+$, 774 $(M–H_2O+2H^+)^{2+}$

[Ga(NOPO-NOC)] solution: Solutions of $Ga(NO_3)_3$ and NOPO-NOC (0.1 mL of 2 mM of each) were mixed. ESI-MS(+): *m/z* = 1612 $(M+H^+)^+$, 806 $(M+2H^+)^{2+}$.

4. Automated ^{68}Ga labeling

^{68}Ga-labeling was performed using a synthesis module (GallElut$^+$ by Scintomics, Fürstenfeldbruck, Germany) as described before, the synthetic procedures being carried out in full automation, controlled by a computer program. Briefly, ^{68}Ga was obtained from a generator with SnO_2 matrix (IThemba LABS, South Africa, distributed by IDB Holland) which was eluted with 1 M aq. HCl. NOPO-RGDfK or NOPO-NOC (0.1–1 nmol) and HEPES (0.4 mL of solution resulting from mixing 7.2 g of HEPES with 6 mL of water) were placed in a 5 mL conical reaction vial (AllTech). For labeling, a 1.25 mL fraction of the generator eluate, containing the highest activity (between 900 and 1000 MBq) was added, resulting in pH of 1.8. The vial was heated to 100 °C for 5 min. Then, the reaction mixture was passed through an SPE cartridge (Waters SepPak C18 classic), the cartridge was purged with 10 mL of water in order to remove non-complexed $^{68}Ga^{3+}$, other ions, and HEPES, and purged with air. The product was eluted with ethanol (1 mL) into a 10 mL flask. In order to obtain a formulation suitable for animal experiments, water (2 mL) and PBS (1 mL) were added and the solution concentrated in vacuo until a final volume of 1 mL was reached, the solution thus possessing suitable pH and osmolality for injection. Product purity was determined by radio-TLC and radio-HPLC.

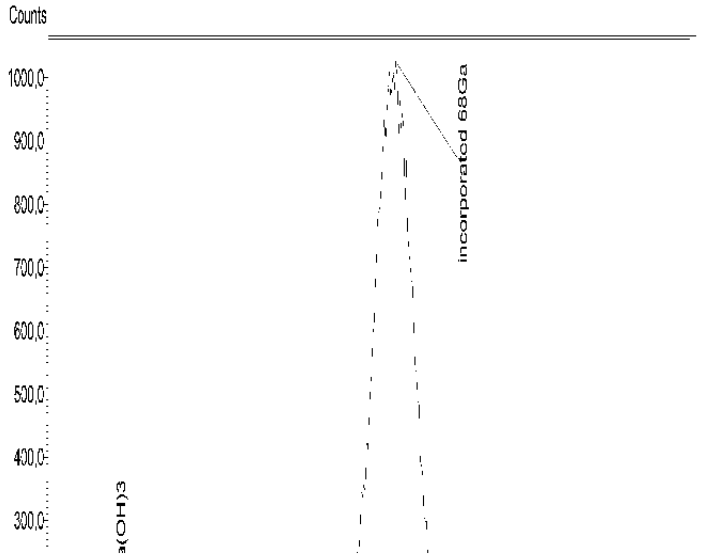

Appendix A

Figure S2: Radio-TLC of ^{68}Ga-NOPO-RGDfK (TLC1).

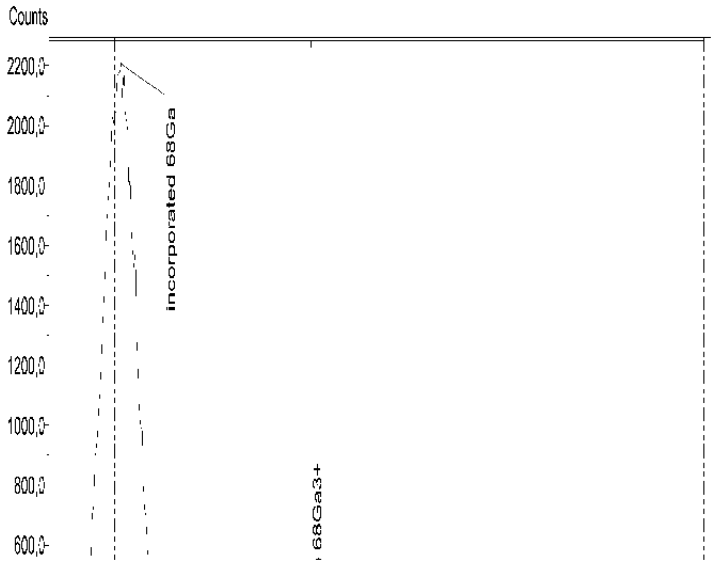

Figure S3: Radio-TLC of ^{68}Ga-NOPO-RGDfK (TLC2).

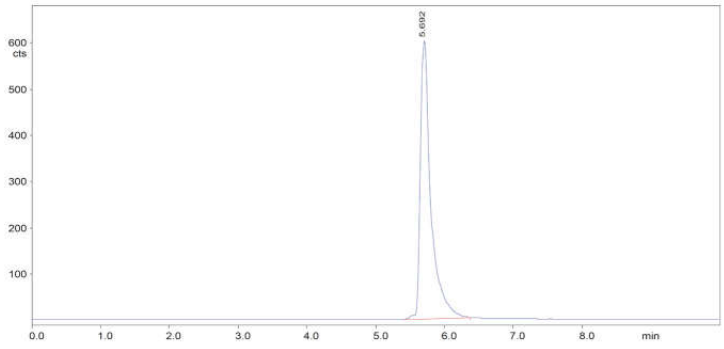

Figure S4: Radio-HPLC of ^{68}Ga-NOPO-RGDfK.

5. Manual radiolabeling and radiolabeling in the presence of Zn^{2+} and Fe^{3+}

A 1.25 mL fraction of the ^{68}Ga eluate was mixed with 800 μL of HEPES solution (7.2 g of HEPES dissolved in 6 mL of water) resulting in pH 2.8. 90 μL of that solution was added to 10 μL of NOPO or NOPO-RGDfK (0.01–10 μM stock solutions), which resulted in total labeling volume of 0.1 mL (0.001–1 μM solutions containing 100 pm–0.1 nmol of a ligand). Such solution was heated to 95 °C for 5 min and then cooled down in a water bath. $^{68}Ga^{3+}$ incorporation was evaluated by radio-TLC.

Labeling in the presence of Fe^{3+} or Zn^{2+} was done at a constant ligand concentration of 3 μM and pH 3.3. Stock solutions of $ZnCl_2$ (3.63 mM) or $FeCl_3$ (72.7 mM) were prepared in 1 M aq. HCl in order to prevent formation of colloidal hydroxides, keeping the pH constant after mixing with the generator eluate. A fraction of the eluate was "contaminated" with these solutions, resulting in a total volume of 1.25 mL. Then, 930 μL of standard HEPES solution (see above) was added. The labeling procedure and analysis were identical as described above. For example, labeling in the presence of Fe^{3+} in concentration of 30 μM was done as following: $FeCl_3$ stock solution (10 μL) was mixed with 1 M aq. HCl (990 μL). 100 μL of that solution was mixed with generator eluate (1.15 mL) and HEPES solution (930 μL). 90 μL of that solution was added to a 30 μM solution of NOPO (10 μL) (resulting in $c_{NOPO} = 3$ μM and $c_{Fe^{3+}} = 30$ μM). This mixture was heated to 95 °C for 5 min, the reaction stopped by cooling in a water bath, and the radioactivity incorporation assessed by radio-TLC.

6. Stability studies

Stability studies in vitro were done with approximately 10 MBq of ^{68}Ga-NOPO-RGDfK solution formulated for injection into the animals (see below). A sample was mixed with PBS or 0.25 M aq. disodium EDTA (0.5 mL) and incubated at 37 °C for 3 h. Radio-HPLC was done at 0.5, 1, 2, and 3 h after mixing. For in vivo experiments, nude mice (see below) were administered approximately 30 MBq of ^{68}Ga-NOPO-RGDfK or ^{68}Ga-NOPO-NOC and sacrificed after 30 min. Dissected organs were frozen in liquid nitrogen, homogenized using a ball mill, and suspended PBS (0.5 mL) containing 10 μg of the precursor. The solid and liquid phases were separated by centrifugation at 1500 rpm for 5 min. The suspension was washed with PBS and subjected to ultrafiltration (30 kDa MWCO). Both pellet and supernatant were measured in a γ-counter (1480 WIZARD™, PerkinElmer Wallac) in order to determine the extraction efficiency. The extracts of liver, kidney, tumour, blood and the urine sample were chromatographed on silica-impregnated chromatography paper (Varian) using 1 M aq. ammonium acetate as mobile phase. Chromatograms were analyzed by autoradiography (using BAS-IP MS 2025 Imaging Plates by Fujifilm, a Dürr Medical CR35BIO for readout and Aida image analyser v 4.24 program for data analysis). No decomposition of the tracer was observed in any of the experiments.

7. Animal models and PET imaging

All animal experiments were performed in accordance with general animal welfare regulations in Germany, and necessary permissions were obtained from the responsible authorities (approval #55.2-1-54-2531-35-06). CD-1 nude mice (Charles River, Germany) were injected subcutaneously with M21 and M21L cells (human melanoma) to the right and to the left shoulder, respectively, as the tumor xenograft models for evaluation of NOPO-RGDfK. For evaluation of NOPO-NOC, the animals were injected with AR42J cells (rat pancreatic carcinoma) to the right shoulder. The animals were anaesthetized with isoflurane, and ~15 MBq of ^{68}Ga-NOPO-RGDfK or ^{68}Ga-NOPO-NOC (prepared as described above) were injected into the tail vein. Anaesthesia was interrupted between injection and imaging. PET scans were recorded 75 min p.i. for 15 min. For blockade, 100 µg of the respective unlabeled compounds in 100 µL PBS were injected 10 min prior to tracer administration. The images were reconstructed using a 3D ordered subsets expectation maximum (OSEM3D) algorithm without scanner and attenuation correction.

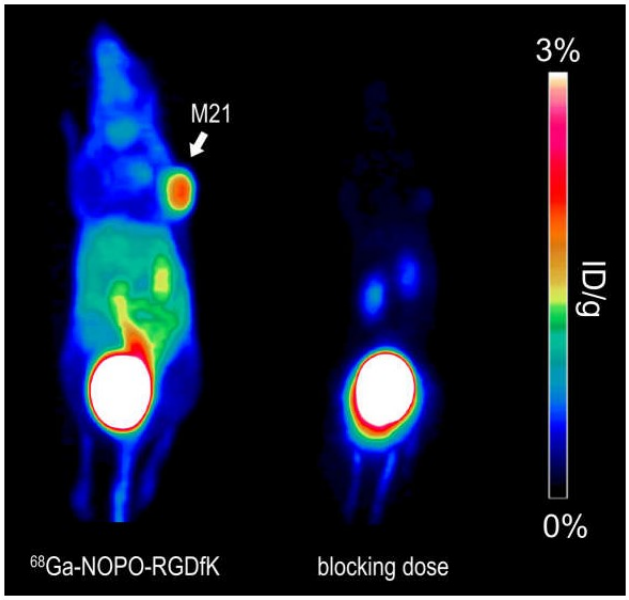

Figure S5: PET images (maximum intensity projections, 75 min p.i.) of nude mouse tumor xenografts (M21 human melanoma) using ^{68}Ga-NOPO-RGDfK (left) and with a blocking dose of excess unlabeled (5 mg per kg body weight) (right).

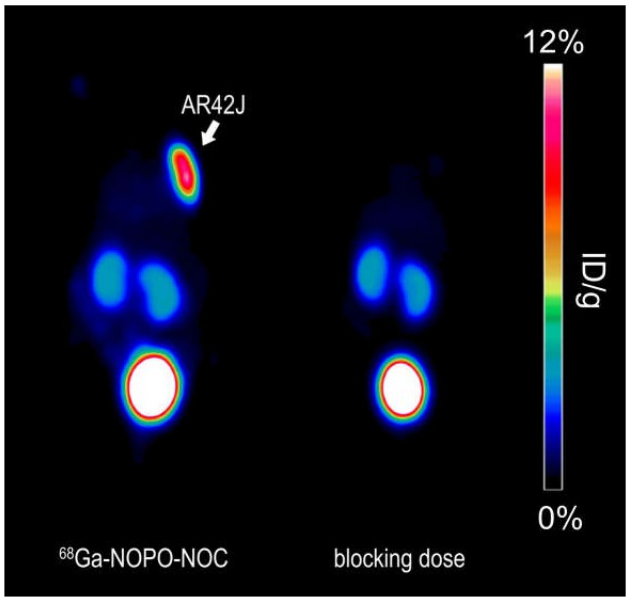

Figure S6: PET images (maximum intensity projections, 75 min p.i.) of nude mouse tumor xenografts (AR42J rat pancreas tumor) using ^{68}Ga-NOPO-NOC (left) and with a blocking dose of excess unlabeled (5 mg per kg body weight) (right).

Appendix A

References

[1] Notni, J.; Hermann, P.; Havlíčková, J.; Kotek, J.; Kubíček, V.; Plutnar, J.; Loktionova, N.; Riss, P. J.; Rösch, F.; Lukeš, I. *Chem. Eur. J.* **2010**, 16, 7174–7185.

[2] Řezanka, P.; Kubíček, V.; Hermann, P.; Lukeš, I. *Synthesis* **2008**, 9, 1431–1435.

Appendix B

Šimeček, J.; Zemek, O.; Hermann, P.; Notni, J.; Wester, H.-J. Tailored Gallium(III) Chelator NOPO: Synthesis, Characterization, Bioconjugation, and Application in Preclinical Ga-68-PET Imaging. *Mol. Pharmaceutics* **2014**, *11* (11), 3893–3903. https://doi.org/10.1021/mp400642s.

Appendix B

molecular pharmaceutics

Article

pubs.acs.org/molecularpharmaceutics

Tailored Gallium(III) Chelator NOPO: Synthesis, Characterization, Bioconjugation, and Application in Preclinical Ga-68-PET Imaging

Jakub Šimeček,[†] Ondřej Zemek,[‡] Petr Hermann,[‡] Johannes Notni,*[,†] and Hans-Jürgen Wester[†]

[†]Lehrstuhl für Pharmazeutische Radiochemie, Technische Universität München, Walther-Meissner-Str. 3, D-85748 Garching, Germany

[‡]Department of Inorganic Chemistry, Charles University in Prague, Hlavova 2030, 12840 Prague 2, Czech Republic

Supporting Information

ABSTRACT: The bifunctional chelator NOPO (1,4,7-triazacyclononane-1,4-bis[methylene(hydroxymethyl)phosphinic acid]-7-[methylene(2-carboxyethyl)phosphinic acid]) shows remarkably high Ga^{III} complexation efficiency and comprises one carboxylic acid moiety which is not involved into metal ion coordination. An improved synthetic protocol affords NOPO with 45% overall yield. Stepwise protonation constants (log K_a), determined by potentiometry, are 11.96, 5.22, 3.77, and 1.54; the stability constant of the Ga(III) complex is log K_{GaL} = 25.0. Within 5 min, ^{68}Ga(III) incorporation by NOPO is virtually quantitative at room temperature between pH 3 and 4, and at 95 °C at pH ranging from 0.5 to 7, at NOPO concentrations of 30 μM and 10 μM, respectively. During amide bond formation at the distant carboxylate using the HATU coupling reagent, an intramolecular phosphinic acid ester (phosphilactone) is formed, which is cleaved during ^{68}Ga complexation or in acidic media, such as trifluoroacetic acid (TFA). Phosphilactone formation can also be suppressed by complexation of Zn^{2+} prior to conjugation, the resulting zinc-containing conjugates nevertheless being suitable for direct ^{68}Ga-labeling. In AR42J (rat pancreatic carcinoma) xenografted CD-1 nude mice, ^{68}Ga-labeled NOPO−Nal^3−octreotide conjugate (^{68}Ga−NOPO−NOC) showed high and fully blockable tumor uptake (13.9 ± 5% ID/g, 120 min p.i., compared to 0.9 ± 0.4% ID/g with 5 mg/kg of nonlabeled peptide). Uptake in other tissues was generally below 3% ID/g, except appearance of excretion-related activity accumulation in kidneys. NOPO-functionalized compounds tend to be more hydrophilic than the corresponding DOTA- and NODAGA-conjugates, thus promoting fast and extensive renal excretion of ^{68}Ga-NOPO-radiopharmaceuticals. NOPO-functionalized peptides provide suitable pharmacokinetics in vivo and meet all requirements for efficient ^{68}Ga-labeling even at room temperature in a kit-like manner.

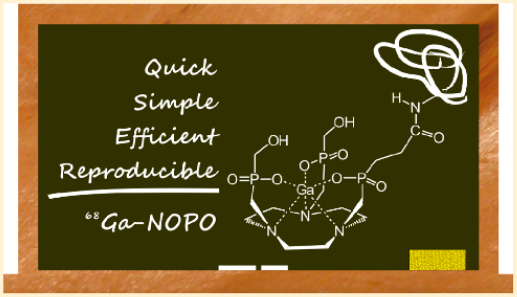

KEYWORDS: *gallium-68, radiopharmaceuticals, phosphinic acid, positron emission tomography, peptides*

INTRODUCTION

^{68}Ga is a positron-emitting radionuclide, which is increasingly used in positron emission tomography (PET).[1] Its physical properties ($t_{1/2}$ = 67.9 min, 89% β^+-decay, E(β^+)$_{max}$ = 1.9 MeV) are suitable for use with targeting vectors possessing fast biokinetics, for example, small molecules and particularly peptides.[2−5] Similarly to ^{99m}Tc, which is widely used in scintigraphy and single photon emission computed tomography (SPECT), ^{68}Ga is generator-produced and therefore readily accessible without an on-site cyclotron.[6] Such a generator can be used for up to one year due to the long half-life of the parent nuclide ^{68}Ge (271 days), and ^{68}Ga can be eluted several times a day. Hence, it represents a constant source of the nuclide, rendering it particularly attractive for routine supply of PET radiopharmaceuticals at facilities with limited access to cyclotron-produced (i.e., radiofluorinated) tracers.[7]

Clinical implementation of ^{68}Ga-PET requires robust and reproducible radiolabeling procedures, which enable a reliable, automated production of ^{68}Ga-radiopharmaceuticals according to standards of good manufacturing practice (GMP).[8] However, protocols developed for the established nuclides ^{18}F or ^{11}C cannot be simply applied to ^{68}Ga, as incorporation of $^{68}Ga^{3+}$ into radiopharmaceuticals is done by complex formation instead of covalent bonding, requiring targeting vectors to be decorated with dedicated chelate ligands. As a result, recent years have seen an increase in research activities directed at efficient bifunctional chelators for $^{68}Ga^{3+}$ (see Chart 1).[9−22]

In this respect, macrocyclic hexadentate ligands, derived from 1,4,7-triazacyclononane (TACN) by *N*,*N*′,*N*″-trisubstitution, have proven particularly valuable. Above all, their Ga^{III} complexes are of extraordinarily high stability, effectively

Special Issue: Positron Emission Tomography: State of the Art

Received: October 30, 2013
Revised: December 4, 2013
Accepted: December 10, 2013
Published: December 10, 2013

Chart 1. Structural Motifs of Some Bifunctional Chelators That Have Recently Been Used in Novel ^{68}Ga-Radiopharmaceuticals[a]

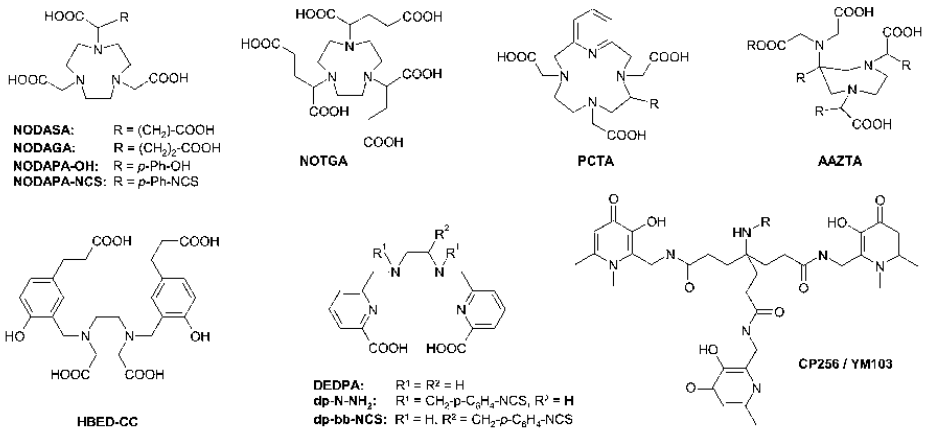

[a]Formulae comprising unspecified "R" represent a family of related structures.

preventing loss of the radiolabel in vivo. This is because such ligands provide almost optimal octahedral coordination geometry on Ga^{III} centers and fully encapsulate the metal ion. In contrast, the hexacoordinate coordination mode of inherently octadentate ligands of the 1,4,7,10-tetraazacyclononane-1,4,7,10-tetraacetic acid (DOTA)[23] type is less suitable for smaller metal ions, resulting in less pronounced kinetic inertness of the respective complexes.[24,25] However, TACN-triacetic acid (NOTA)[26] and its many bifunctional derivatives (such as NODASA,[14] NODAGA,[15] NODAPA,[16] or NOTGA,[17] see Chart 1) show significantly slower complex formation compared to open-chain ligands (such as DEDPA[19] or HBED-CC[20]), since the complexation reaction of the first involves a higher activation barrier than observed for the latter. In terms of ^{68}Ga-radiochemistry, this translates to higher chelator concentration or temperature required for radiolabeling of the macrocycles, which is detrimental either to achievable specific activity of the radiotracers, or to compatibility with heat-sensitive biomolecules. On the other hand, metal complexes of open-chain ligands generally show a lower degree of kinetic stability, compared to their cyclic analogues.

To overcome the only disadvantage of NOTA-like chelators, which is their comparably slow Ga^{III} complex formation, exchange of the pendant arm carboxylates by phosphinates has proven a successful approach. TACN-*N*,*N*′,*N*″-tris-(methylenephosphinic acid) chelators (TRAP, see Chart 2) were recognized to possess not only much faster Ga^{III} complexation kinetics, but the resulting complexes show higher resistance to acid- and particularly base-catalyzed demetalation.[12,27] Although TRAP chelators with simple *P*-substituents, for example, TRAP-H and TRAP-Ph (Chart 2), have been synthesized and characterized more than two decades ago,[28] the potential of tailored TRAP ligands for application in ^{68}Ga-PET was reported just recently.[4,13,29,30] Their most remarkable feature is a pronounced selectivity for $^{68}Ga^{3+}$ in presence of certain contaminants typically found in ^{68}Ge/^{68}Ga generator eluates, namely, Zn^{2+}, Fe^{3+}, and Cu^{2+},[31] which is rooted in the fact that TRAP complexes of many metal ions are able to undergo swift metal exchange to form the thermodynamically most stable Ga^{III} chelates.[32]

Chart 2. 1,4,7-Triazacyclononane-1,4,7-tris(methylenephosphinic acid) ("TRAP") Chelators

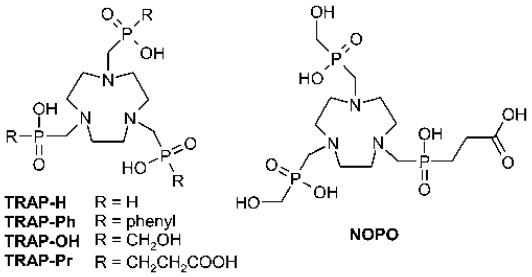

A comparison of a small series of TRAP chelators revealed the advantages of presence of additional heteroatoms in the side chains; those featuring 2-carboxyethyl- and hydroxymethyl-*P*-substituents (TRAP−Pr and TRAP−OH, respectively, see Chart 2) showed the best ^{68}Ga-labeling characteristics upon variation of experimental conditions like pH, temperature, time, and precursor concentration.[29] As the three terminal carboxylic acid functions of TRAP-Pr allow for facile functionalization via amide coupling, this structure is a particularly suitable scaffold for conjugates comprising three targeting vectors or other functional molecules.[4,29,33] By decorating the TACN backbone with the side arm motifs of both TRAP-Pr and TRAP−OH, we obtained NOPO (1,4,7-triazacyclononane-1,4-bis[methylene-(hydroxymethyl)phosphinic acid]-7-[methylene(2-carboxyethyl)phosphinic acid], see Chart 2),[13] which possesses one pendant arm with a carboxylic acid moiety for bioconjugation, and two hydroxymethyl-end-capped pendant arms. As a complement to the trimer-scaffold TRAP-Pr, NOPO has been specifically designed for applications where mono-conjugation is preferred and presence of more than one functional group for conjugation would be disturbing, but at the same time, maximal ^{68}Ga labeling performance is required. Here we report an improved synthesis as well as detailed chemical and radiochemical investigations of NOPO.

dx.doi.org/10.1021/mp400642s | *Mol. Pharmaceutics* 2014, 11, 3893−3903

Appendix B

EXPERIMENTAL SECTION

General Methods. If not denoted otherwise, all reactants and solvents were commercially available analytical grade chemicals. 1-Benzyl-1,4,7-triazacyclononane was purchased from Chematech (France), 2-[(*t*-butyloxycarbonyl)ethyl]-phosphinic acid, and NOPO-NOC were prepared according to published procedures.[13,34] NMR spectra were recorded on VARIAN UNITY Inova (400 MHz), VNMRS (300 MHz), and Bruker AVANCE-III (600 MHz) NMR systems. ^{1}H and ^{13}C NMR shifts are referenced to *t*-butanol (1.25 and 30.29 ppm, respectively), ^{31}P NMR shifts are referenced to 85% aq H_3PO_4 solution as external standard (0.0 ppm), and ^{71}Ga shifts are referenced to 0.2 M aq $[Ga(OH)_4]^-$ (222 ppm) or $[Ga(H_2O)_6]^{3+}$ (0 ppm) solutions as external standards. Mass spectra were measured on Bruker Esquire 3000 and Varian Ion-trap 500 spectrometers with ESI as an ion source and ion trap as a detector in positive or negative modes. pH was measured with a SevenEasy pH-meter (Mettler Toledo). ^{68}Ga−NOPO−NOC for preclinical studies was prepared in a fully automated procedure as described in refs 13, 30, and 33.

*1,4,7-Triazacyclononane-1-benzyl-4,7-bis[methylene-(hydroxymethyl)phosphinic acid] (**2**).* 1-Benzyl-1,4,7-triazacyclononane (1.28 g, 5.88 mmol) and paraformaldehyde (0.44 g, 14.6 mmol) were dissolved in a mixture of 50% aq H_3PO_2 (6.6 mL, 60.6 mmol) and water (5 mL). The reaction mixture was stirred for 12 h at r.t., then three times coevaporated with water and chromatographed on strong cation exchanger (DOWEX 50, H^+-form). Triazacyclononane-based products were eluted with a mixture of 6 M aq HCl and EtOH, 1:1 by volume. The eluate was evaporated and the crude product dissolved in 6 M HCl (20 mL). Paraformaldehyde (0.73 g, 24.3 mmol) was added, and the solution refluxed for 5 h, then evaporated and purified on silica gel (mobile phase: acetonitrile−MeOH−[25% aq NH_3], 2:1:3 by volume). Fractions containing the pure product were identified by ^{31}P NMR, collected, and evaporated in vacuo, yielding **2** (1.20 g, 96%) in form of a dark-yellow solid. ^{1}H NMR (300 MHz, D_2O): δ = 2.61−3.25 (m, ring-CH_2, 12H and N−CH_2−P, 4H), 3.47 (d, $^{2}J_{PH}$ = 6.00 Hz, P−CH_2−OH, 4H), 4.24 (s, N−CH_2−C_6H_5, 2H), 7.37−7.47 (m, −C_6H_5, 5H). ^{13}C{^{1}H} NMR (75 MHz, D_2O): δ = 48.24 (s, ring-CH_2, 2C), 50.81 (s, ring-CH_2, 4C), 52.27 (d, $^{1}J_{PC}$ = 94.0 Hz, N−CH_2−P, 2C), 58.89 (s, N−CH_2−C_6H_5, 1C), 59.96 (d, $^{1}J_{PC}$ = 82.2 Hz, P−CH_2−OH, 2C), 129.35 (s, *C*H(Ar), 2C), 130.69 (s, *C*H(Ar), 2C), 129.82 (s, *C*H(Ar), 1C), 131.10 (s, CH_2−*C*H(Ar), 1C). ^{31}P{^{1}H} NMR (121 MHz, D_2O): δ = 35.22. ^{31}P NMR (121 MHz, D_2O): δ = 35.65. MS (ESI, negative): m/z = 434 [M + H^+].

*1,4,7-Triazacyclononane-1,4-bis[methylene-(hydroxymethyl)phosphinic acid] (**4**).* **2** (1.20 g) was dissolved in glacial acetic acid, 0.12 g of 10% Pd/C was added, and a hydrogen atmosphere was maintained overnight. The mixture was filtered and the filtrate evaporated in vacuo, yielding **4** (0.90 g, 93%) as a colorless solid. ^{1}H NMR (300 MHz, D_2O): δ = 2.00 (s, N−H, 1H), 2.92 (s, ring −CH_2−, 4H), 3.05 (d, $^{2}J_{PH}$ = 7.2 Hz, N−CH_2−P, 4H), 3.12 (t, $^{3}J_{HH}$ = 5.7 Hz, ring-CH_2, 4H), 3.25 (t, $^{3}J_{HH}$ = 5.4 Hz, ring-CH_2, 4H), 3.68 (d, $^{2}J_{PH}$ = 6.30 Hz, P−CH_2−OH, 4H). ^{13}C{^{1}H} NMR (75 MHz, D_2O): δ = 43.59 (s, ring-CH_2, 2C), 48.46 (s, ring-CH_2, 2C), 52.28 (d, $^{3}J_{PC}$ = 6.0 Hz, ring-CH_2, 2C), 52.27 (d, $^{1}J_{PC}$ = 94.0 Hz, N−CH_2−P, 2C), δ 59.74 (d, $^{1}J_{PC}$ = 106.7 Hz, P−CH_2−OH, 2C). ^{31}P{^{1}H} NMR(121 MHz, D_2O): δ = 35.61. ^{31}P NMR (121 MHz, D_2O): δ = 35.64. MS (ESI, positive): m/z = 346 [M + H^+].

1,4,7-Triazacyclononane-1,4-bis[methylene-(hydroxymethyl)phosphinic acid]-7-[methylene(2-carboxyethyl)phosphinic acid] (NOPO). **4** (0.90 g) and (2-carboxyethyl)phosphinic acid (0.63 g, 4.6 mmol) were dissolved in 6 M aq HCl and heated to 75 °C. Paraformadehyde (0.35 g, 11.6 mmol) was added during 24 h in small portions. The reaction mixture was three times coevaporated with water (5 mL) to remove HCl and loaded on cation exchange column (DOWEX 50, H^+-form). The column was eluted with water. Fractions containing pure NOPO were identified by ^{31}P NMR, collected and evaporated in vacuo, and dried in a vacuum desiccator over P_2O_5. NOPO·0.6 H_2O (0.91 g, 50%) was obtained as a pale-yellow oil which solidifies upon standing.

Potentiometric Measurements. Potentiometric studies were carried out using a titration system consisting of PHM 240 pH-meter, 2-mL automatic piston buret ABU 900, and combined glass AgCl electrode GK 2401B (Radiometer).[35] $Ga(NO_3)_3$ stock solution was stabilized by addition of a known amount of nitric acid to prevent hydrolysis. Titrations were performed at 25.0 ± 0.1 °C under argon saturated with water vapors, pK_w = 13.81, at ionic strength I = 0.1 M NMe_4Cl, pH range 1.8−12.0 for ligand and 1.5−12 for Ga^{III}:NOPO system. The initial volume was V_0 = 5 mL. The ligand concentration in titrated solutions was 4 mM. The ligand titration ("in-cell") was repeated four times in parallel (each titration curve consisted of approximately 40 points). "Out-of-cell" method was used for titrations of Ga^{III}:NOPO. Solutions for "out-of-cell" titrations were kept in tightly closed tubes (pH < 6) or in flame-sealed ampules (pH > 6) to avoid contamination with atmospheric CO_2 during standing over two weeks. The pH of each solution for "out-of-cell" titration was measured with a freshly calibrated electrode. The protonation and stability constants were calculated using OPIUM.[36] The calibration function used was $E = E_0 + S \times \log[H^+] + j_1 \times [H^+] + j_2 \times [OH^-]$, where E_0 stands for standard potential of the electrodes and contains a contribution of inert ions to the liquid-junction potential, S corresponds to the Nernst slope, and $j_1 \times [H^+]$ and $j_2 \times [OH^-] = j_2 \times K_w/[H^+]$ are the contributions of H^+ and OH^- ions to the liquid/junction potential (j_1 and j_2 comprise a deviation from linear potential −log[H^+] dependency in strongly acidic or alkaline regions, respectively). The electrode calibration parameters were determined from titration of standard HCl solution with standard NMe_4OH solution before each titration to give a pair calibration-titration that was then used for equilibrium constant determination. Stability constants of gallium(III) hydroxo complexes were taken from literature.[37] The constants determined are concentration constants.

Conjugation. Investigation of the coupling reaction was performed in NMR tubes, while each step was monitored by ^{31}P NMR and ESI-MS. NOPO·0.6H_2O (20 mg, 40 μmol) and equimolar amounts of the respective amine component (10.3 mg L-phenylalanine *t*-butyl ester hydrochloride or 2.7 mg $MeNH_2$·HCl) were dissolved in dry DMSO (dimethyl sulfoxide, 0.3 mL), whereafter dry DIPEA (diisopropylethylamine, 52 mg, 404 μmol) and subsqequently HATU (*O*-(7-aza-1*H*-benzotriazole-1-yl)-1,1,3,3-tetramethyluronium hexafluorophosphate, 46 mg, 120 μmol) were added.

Manual Radiolabeling. A ^{68}Ge/^{68}Ga generator with SnO_2 matrix (iTHEMBALabs, South Africa), was eluted with 1 M aq HCl (prepared from Ultrapur water and conc. HCl, Merck, Darmstadt, Germany), using automated module (GallElut$^+$, Scintomics, Fürstenfeldbruck, Germany). A fraction of 1.25 mL,

containing the highest activity (≈ 900 MBq), was used for labeling purposes without further purification. A pH of 2.8 was adjusted by addition of aq 2-[4-(2-hydroxyethyl)-piperazin-1-yl]-ethanesulfonic acid (HEPES, 2.7 M, 800 μL). 90 μL of this solution was mixed with 10 μL of chelator stock solution (0.3−30 μM) in 1.5 mL Eppendorf cups (total reaction volume was 0.1 mL). The labeling mixtures were incubated at r.t. for 5 min or placed in a water bath (95 °C) for 5 min and subsequently cooled down in another water bath (20−25 °C). ^{68}Ga incorporation was evaluated by TLC (Varian chromatography paper, mobile phase: 1 M aq NH_4OAc−MeOH, 1:1 by volumes). The adjustment of different pH values for assessment of pH dependence was completed as follows: pH 0.5 and 1 were achieved by diluting neat eluate with appropriate amounts of water; pH 2−4 were adjusted solely with HEPES, higher pH with further addition of 1 M aq NaOH.

Determination of Octanol−Water Distribution Coefficients (log *D*). *n*-Octanol−water distribution coefficients were determined by addition of 1−2 MBq of ^{68}Ga-labeled compound, prepared in automated procedure as described previously,[13,30,33] to an Eppendorf cup containing *n*-octanol (0.5 mL) and isotonic phosphate-buffered saline (PBS, 0.5 mL). After 2 min of vigorous stirring, the phases were separated by centrifugation at 11500 *g*, and the activities in 100 μL aliquots of each phase determined with a γ-counter. Each experiment was repeated 8 times.

Animal Models. All animal experiments were performed in accordance with current animal welfare regulations in Germany. Permission was obtained from the responsible authorities (Regierung von Oberbayern, Germany, no. 55.2-1-54-2531-35-06). The AR42J xenograft models were produced as described before.[38] In short, athymic CD-1 nude mice (Charles River, Germany) were injected subcutaneously with AR42J cells (rat pancreatic carcinoma, 5−10 million) to the right shoulder, whereupon tumors grew to a size of 3−5 mm in diameter within 7−10 days.

PET Imaging and Biodistribution. The animals were anaesthetized with isoflurane, and ^{68}Ga−NOPO−NOC (≈ 15 MBq) was injected into the tail vein. Anaesthesia was interrupted between injection and imaging. PET scans were recorded 75 min p.i.; the acquisition time was 15 min. The images were reconstructed using a 3D ordered subsets expectation maximum (OSEM3D) algorithm without scanner- and attenuation correction. Biodistribution and metabolite studies were performed as described before.[33]

RESULTS AND DISCUSSION

For the sake of brevity, charge and protonation state of NOPO and its Ga^{III} complex is not denoted, unless a particular species is addressed and distinction is necessary for comprehension. In all other cases, we refer to any protonated or ionic form that may apply.

Synthesis. The synthesis of NOPO employing the Moedritzer−Irani[39] (Mannich-type) reaction according to Scheme 1 was optimized to afford NOPO with 45% yield based on 1-benzyl-TACN (**1**), which constitutes a significant improvement of the 18% obtained by the previously reported procedure.[13] Reaction monitoring of reaction step **a** and **d** by ^{31}P NMR and mass spectroscopy revealed that the main side reaction responsible for lowering the overall reaction yield is reductive *N*-methylation[27,40] resulting in compounds **3** and particularly **5**, the respective phosphinic acid component acting as a reductive agent.

Scheme 1. Synthesis of NOPO[a]

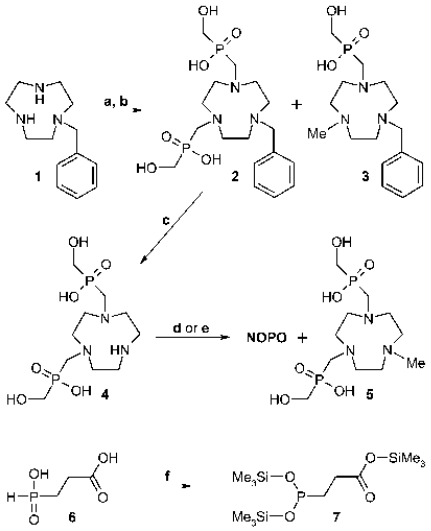

[a]a: $H_2C{=}O$, H_3PO_2, H_2O, r.t., 12 h; b: $H_2C{=}O$, 6 M aq HCl, 100 °C, 5 h, 96% of **2**; c: H_2, 10% Pd/C, H_2O, r.t., 12 h, 93%; d: **6**, 6 M aq HCl, 75 °C, 24 h, 50%; e: (i) **7**, HMDS, $H_2C{=}O$, Ar atmosphere, 130 °C, 12 h; (ii) MeOH, ion exchanger chromatography, 47%; f: hexamethyldisilazane, Ar atmosphere, 130 °C, 24 h, quantitative according to ^{31}P NMR.

After an almost quantitative reaction according to path **a**, followed by chromatographic purification and deprotection (step **c**) of **2**, the intermediate **4** was obtained with 89% yield based on **1**. Contrary to step **a**, a higher temperature of 75 °C is necessary for the second amine phosphomethylation in step **d**, because 2-carboxyethylphosphinic acid (**6**) is less reactive than phosphinic acid. Thus, a significantly higher amount of *N*-methylated byproduct **5** (22% determined by ^{31}P NMR spectroscopy, compared to 3% of **3** for reaction **a**) was formed. After final purification on strong cationic exchanger (DOWEX 50), NOPO was obtained with yields of 50% or 45%, based on compounds **4** and **1**, respectively.

As an alternative to step **d**, reaction path **e** was evaluated (for details see Supporting Information), employing the fully silylated phosphite derivative **7**. However, we found that the reaction according to **d** is to be preferred, because for path **e**, the necessity of working under inert gas considerably increases expenditure of work, but the yield actually was not superior to path **d**. Notwithstanding this, syntheses along path **e** could be well-suited for functionalization of acid-sensitive substrates with methylene(2-carboxyethyl)phosphinic acid moieties, since path **d** inevitably affords strongly acidic conditions and elevated temperatures.

Equilibrium Studies. Stepwise protonation constants of NOPO (Table 1 and Supporting Information, Table S1) were determined by potentiometry, and a protonation sequence is proposed in analogy to other TACN-based chelators. Table 1 shows that the first protonation constant of NOPO is somewhat higher compared to its parent ligands TRAP−OH and TRAP−Pr[12,27] but much lower than that of NOTA.[41] The second protonation occurs at another ring nitrogen, while the third (log K_3 = 3.77) occurs at the terminal carboxylate and is

Appendix B

Table 1. Stepwise Protonation Constants (log K_a) of NOPO and Comparison with those of TRAP−OH, TRAP−Pr, and NOTA (25 °C, I = 0.1 M Me_4NCl)

no. protons	NOPO	TRAP−OH[27]	TRAP-Pr[12]	NOTA[41]
1	11.96	11.47	11.48	13.17
2	5.22	3.85	5.44	5.74
3	3.77	1.30	4.84	3.22
4	1.54		4.23	1.96
5			3.45	
6			1.66	

within the range of carboxylate acidities of TRAP-Pr (log K_{3-5} = 4.84−3.45). The last protonation, which we assume to occur on one of the phosphinates, shows that acidity of the phosphinic acid moieties of NOPO (log$K_4 \leq 1.54$) represents an intermediate of the values found for TRAP-Pr (log $K_6 \leq$ 1.66) and TRAP−OH (log $K_3 \leq 1.30$).

Since potentiometry only delivers information about protonation states of certain species, ^{31}P NMR spectroscopy was employed to obtain additional structural information about the equimolar Ga^{III}−NOPO system. Figure 1 shows that, at pH 3, two signals in 1:2 ratio are observed, corresponding to the two structurally nonequivalent phosphorus atoms of NOPO. Furthermore, the ^{71}Ga-NMR spectrum (see Supporting Information, Figure S2) displays one narrow singlet, indicating that Ga^{III} possesses a highly symmetrical coordination environment, with a shift of δ_{Ga} = 135 ppm which is very similar to

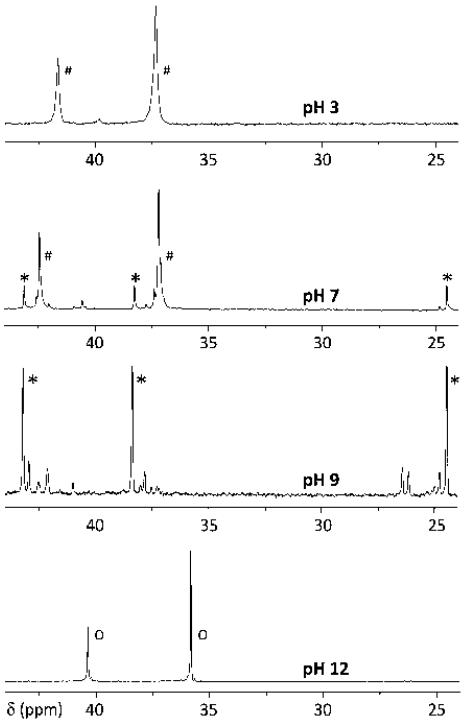

Figure 1. Equilibrium $^{31}P\{^1H\}$ NMR spectra of [Ga(NOPO)] at different pH (c_{NOPO} = 100 mM in H_2O). #: signals of [Ga(NOPO)]; *: signals of $[Ga(NOPO)(OH)]^{2-}$; ○: signals of metal-free NOPO.

previously reported "in-cage"-Ga^{III} complexes of TRAP-type ligands.[12,27] Altogether, we thus assume that Ga^{III} ion, comprised in [Ga(NOPO)] species below neutral pH, adopts a pseudo-octahedral (or trigonal-antiprismatic) geometry, coordinating three ring nitrogen atoms and three phosphinate oxygen atoms in an "in-cage" manner.

Apart from formation of tetrahydroxogallate due to decomplexation in the highly basic region, the distribution diagram of the Ga^{III}−NOPO system shows the release of two additional protons between pH 7 and 11 (Figure 2), with corresponding pK_a values of 7.43 and 9.46 (Table 2). Unfortunately, potentiometry only determines the number of protons released. It does not allow to distinguish whether these protons originate from dissociation of H_2O enforced by complexation of the hydroxide ion, or from ligand deprotonation, for example, of a side arm hydroxyl group. However, Figure 1 shows that, at pH 7, the formation of a second species can be observed by ^{31}P NMR, which is the prevailing one at pH 9. The spectra display three signals with equal intensity (labeled with asterisks), corresponding to three different P atoms. Hence, a substantial change of coordination geometry can be assumed. In addition, the aforementioned narrow ^{71}Ga NMR signal is lost, indicating a more asymmetrical coordination sphere,[42] which is not consistent with further presence of the "in-cage"-complex.

For the closely related equimolar Ga^{III}−(TRAP−OH) system, a similar distribution of species was observed by potentiometry, and possible structures have been elucidated by density functional calculation.[27] In analogy to these results, we assume that the species with highest abundance at approximately pH 9 (see Figure 2) is an "out-of-cage"-complex with the formula $[Ga(NOPO)(OH)]^{2-}$, wherein Ga^{III} is not bound by the ring nitrogen atoms anymore. The rearrangement also involves a proton shift from a side arm OH-group to a highly basic, free ring amine. The deprotonated hydroxyl group, the three phosphinate oxygen atoms, and one monodentate hydroxide ligand are coordinating Ga^{III} ion in a pentadentate manner (see Scheme 2). This interpretation is well in accordance with $^{31}P\{^1H\}$ NMR spectrum recorded at pH 9. As required, the proposed structure comprises three different phosphorus atoms, consistent with the three distinct singlets observed. Of these, the signal at approximately 25 ppm most likely corresponds to the hydroxymethylphosphinate side arm with deprotonated hydroxyl group, since the additional negative charge entails an enhancement of electron density at the adjacent phsophorus atom, resulting in high-field shift.

Release of another proton, observed upon further increase of pH, most likely occurs on the second side arm hydroxyl group, which subsequently engages into Ga^{III} complexation.[27] Since this last deprotonation goes beyond the common conception of NOPO as a tetra-basic ligand, the corresponding species, $[Ga(H_{-1}NOPO)(OH)]^{3-}$, is denoted with a negative proton index for NOPO. The ^{31}P NMR signals with low intensity, which are observed at pH 9, are probably related to presence of several conformers of this species.

However, it must be noted that that all of these substantial changes of the Ga^{III} coordination mode upon pH variation occurred within a time scale of days and thus are not pertinent to ^{68}Ga radiochemistry due to the short half-life of the nuclide. Most importantly, at pH 7, no measurable out-of-cage complex formation was observed by ^{31}P NMR within one day. The equilibrium between $[Ga(NOPO)]^-$ and $[Ga(NOPO)(OH)]^{2-}$ was reached after 11 days. Therefore, potentiometric

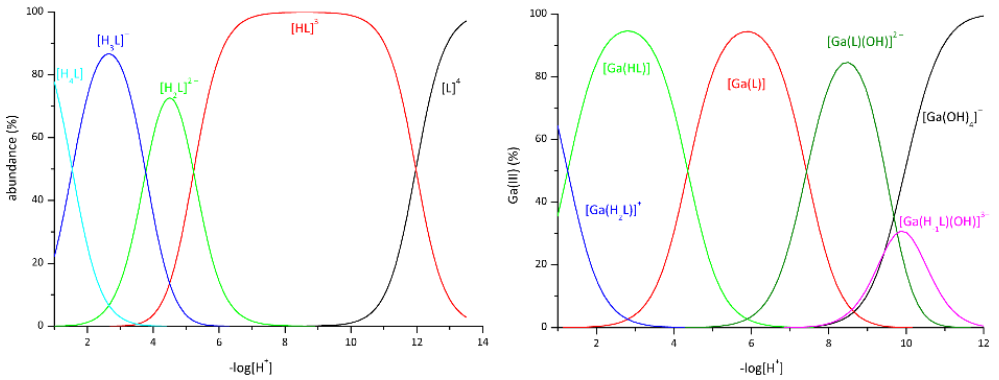

Figure 2. Species distribution diagrams for NOPO (left, c_{NOPO} = 4 mM) and the Ga^{III}–NOPO system (right, $c_{Ga} = c_{NOPO}$ = 4 mM). Fully (4-fold) deprotonated NOPO is abbreviated by L.

Table 2. Stability and Stepwise Protonation Constants for the Ga^{III}–NOPO System (25°C, I = 0.1 M Me_4NCl)

equilibrium	log K_{GaL} or log K_a
$Ga^{3+} + NOPO^{4-} \leftrightarrow [Ga(NOPO)]$	25.0
$[Ga(NOPO)]^- + H^+ \leftrightarrow [Ga(HNOPO)]$	4.4
$[Ga(HNOPO)] + H^+ \leftrightarrow [Ga(H_2NOPO)]^+$	1.2
$[Ga(NOPO)(OH)]^{2-} + H^+ \leftrightarrow [Ga(NOPO)]^- + H_2O$	7.4
$[Ga(H_{-1}NOPO)(OH)]^{3-} + H^+ \leftrightarrow [Ga(NOPO)(OH)]^{2-}$	9.8

Scheme 2. Proposed Change of the Solution Structure of the Ga^{III}-Complex of NOPO at Slightly Alkaline pH, as Inferred from Potentiometric and ^{31}P NMR Data as well as Previous DFT Calculations[27]

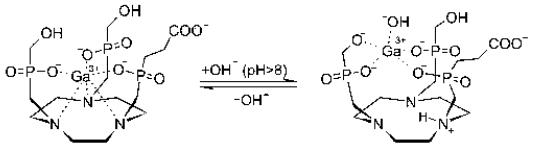

determination of the equilibrium constants of the equimolar Ga-NOPO system (Table 2) had to be done by out-of-cell titration, allowing the equilibration of titrated samples for two weeks. The thermodynamic stability constant of [Ga(NOPO)], log K_{GaL} = 25.0, is between those of [Ga(TRAP−Pr)] and [Ga(TRAP−OH)] (logK_{GaL} = 26.24 and 23.3, respectively)[12,27] and supports the perception of NOPO as a hybrid of its parent ligands, TRAP−Pr and TRAP−OH. Values of the stability constants of the Ga^{III} complexes of NOTA-like ligands show a linear correlation with ligand basicity (see Supporting Information, Figure S1). In addition, [Ga(NOPO)] chelates were found inert toward acid-promoted hydrolysis, as even in 6 M aq $HClO_4$, no decomposition could be detected by ^{31}P NMR after three months.

Conjugation Chemistry. In our pilot study on first NOPO bioconjugates, we reported preliminary in vivo imaging of the somatostatin-receptor (sstr) status using ^{68}Ga–NOPO–NOC.[13] For the conjugate of NOPO with the sst2-targeting cyclic octapeptide NOC (NaI^3-octreotide), the molecular peak, detected by ESI-MS, possessed a lower mass than expected (m/z = 1528 instead of 1546). Since the difference of 18 indicates loss of water, which is very common in MS and which can have a plethora of causes, we did not pursue this issue further at that time. However, this phenomenon was also observed upon coupling of other amines using HATU, and a detailed study revealed an unexpected reactivity of NOPO, namely formation of intramolecular phosphinic acid esters (phosphilactones).

The regio- and stereochemistry was investigated on the example of the reactions with methylamine, L-*O*-*t*-butyl phenylalanate, and without addition of amine, that is, upon addition of only the coupling reagents, as negative control. We found that generally, the phosphilactone **A** according to Chart 3

Chart 3. Possible Regioisomers of Intramolecular Phosphinic Acid Esters (Phosphilactones)[a]

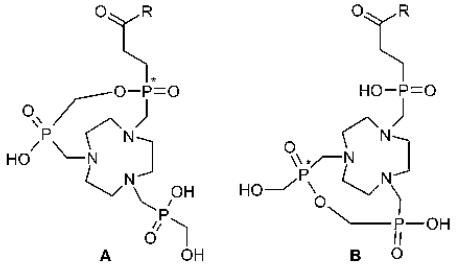

[a]Chiral phosphorus atoms are marked with asterisks. Isomer **A** is quantitatively formed in the course of the reaction of NOPO with amines, HATU, and DIPEA in DMSO.

is formed quantitatively within minutes of addition of the coupling reagents, with one chiral phosphorus center being formed in the course of the reaction. With chiral substrates, such as L-amino acids, two diastereomers were formed in equal amounts, meaning that no chiral induction occurs on the phosphorus atom.

Figure 3 illustrates, on the example of methylamide formation, how ^{31}P NMR shifts and $^3J_{pp}$ coupling constants allowed for unambiguous identification of the products. In the course of the reaction, the singlet of the (2-carboxyethyl)-substituted phosphorus atom disappears, and two novel doublets show up, the value of 16.4 Hz for the coupling constant being characteristic for a $^3J_{pp}$ interaction. In addition, the ^{31}P NMR shift of 53 ppm is characteristic for phosphinic

Appendix B

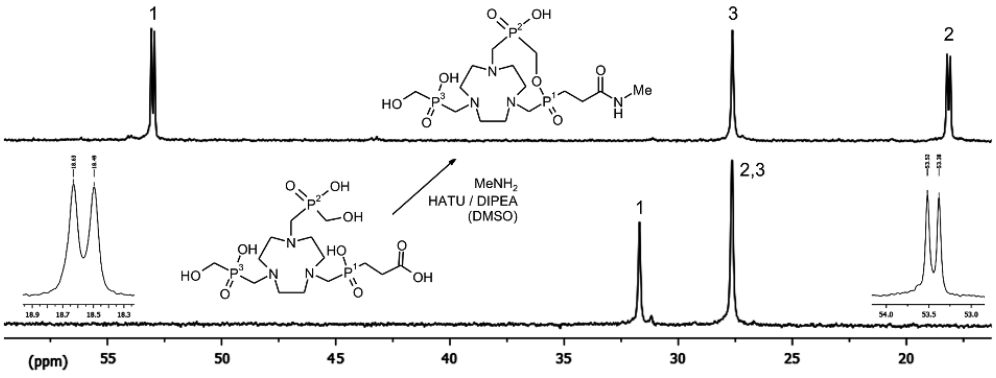

Figure 3. $^{31}P\{^{1}H\}$ NMR spectra of NOPO in DMSO with addition of DIPEA (lower) and after subsequent addition of methylamine hydrochloride and HATU (upper).

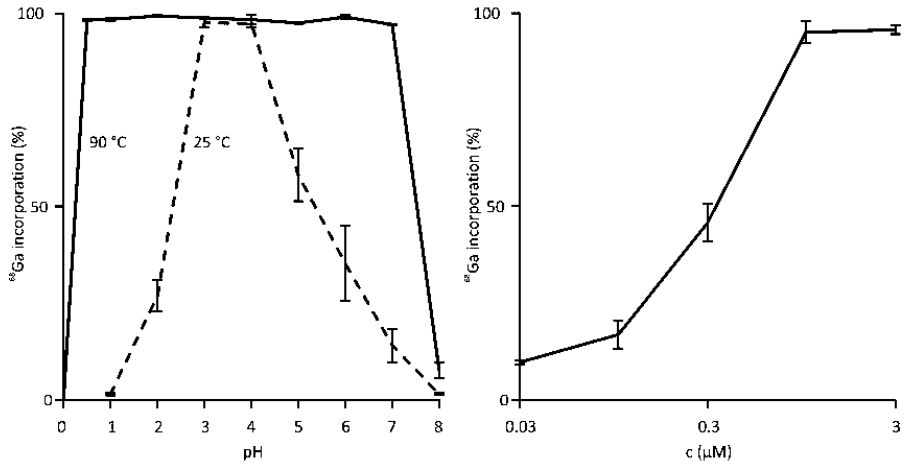

Figure 4. Left: ^{68}Ga incorporation into NOPO (t = 5 min) as functions of pH (solid line: T = 95 °C, c = 10 μM; dashed line: T = 25 °C, c = 30 μM). Right: Labeling of phosphilactone-NOPO-NOC as function of precursor concentration (t = 5 min, T = 95 °C, pH 2.8).

acid esters, which are usually found in the range of 50−55 ppm. Hence, formation of only the isomer **A** can be concluded; corresponding spectra are shown in Supporting Information, Figures S3−S5.

Substantial amounts of the isomer **B** are formed only with substoichiometric amounts or in absence of an amine. No evidence for formation of intramolecular esters involving the terminal carboxylic acid was observed. Furthermore, the addition of only DIPEA to a DMSO solution of NOPO did not result in any reaction, indicating the phosphilactone formation is effected by HATU. However, upon addition of DIPEA a shift of the ^{31}P NMR signals of NOPO is observed, because these are sensitive to the protonation state of the ligand (see Supporting Information, Figure S6).

The free phosphinic acid moiety can be restored easily by addition of trifluoroacetic acid (TFA) or HCl. The cleavage reactions with neat TFA or 50% and 10% aqueous TFA solutions were monitored by MS and showed that cleavage is quantitative at 25 °C after ≈45, 180, or 720 min, respectively. In 1 M aq HCl, full cleavage takes around 2 h, whereas in 0.1 M aq HCl or weaker organic acids (acetic or formic acid) the reaction was not finished after 48 h. A control sample of a neutral aqueous solution of **A** was found unchanged after 48 h.

As an alternative, the formation of the phosphilactone can be elegantly avoided in the first place by addition of one equivalent of Zn^{2+} to the solution of NOPO in DMSO. Formation of the Zn^{II}−NOPO complex engages all phosphinate moieties into zinc(II) coordination, which effectively prevents ester formation with the hydroxymethyl groups during amide coupling using DIPEA and HATU. In this manner, the conjugate will of course be obtained as the zinc(II) complex (for an example, see Supporting Information, Figure S7). However, it has been shown earlier that Zn^{II}−NOPO complexes can be efficiently labeled with ^{68}Ga as well (that is, by Zn^{II}−$^{68}Ga^{III}$ transmetalation).[31] Hence, protection of NOPO by Zn^{II}-complexation can be considered a useful method with practical relevance, immediately yielding precursors suitable for ^{68}Ga-labeling. Moreover, distribution diagrams of Zn^{II}-TRAP systems show the presence of free Zn^{2+} below pH 2.[12] Thus, Zn^{II}−NOPO conjugates can be demetalated under these conditions, provided an excess of suitable scavenger ligand

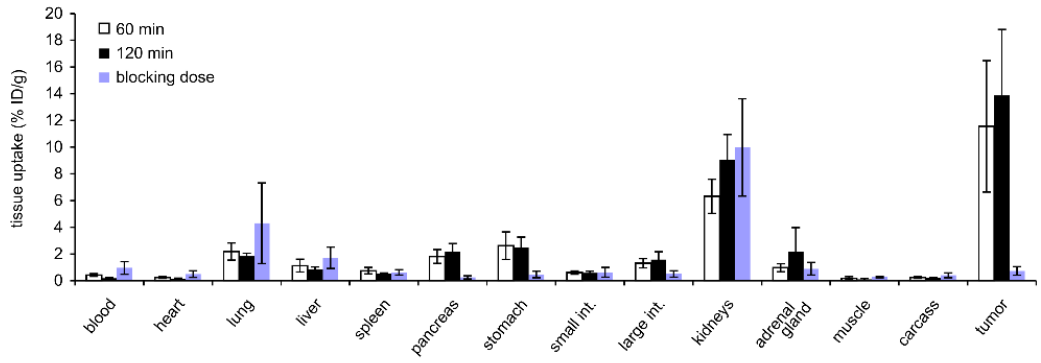

Figure 5. Distribution of ^{68}Ga–NOPO–NOC (15 MBq, ≈ 500 GBq/μmol) in AR42J rat pancreatic carcinoma xenografted CD-1 nude mice, 60 min (N = 7) and 120 min (N = 5) post injection. Blockade (60 min p.i., N = 4) was done by administration of ^{nat}Ga–NOPO–NOC (5 mg/kg body weight).

capable of forming highly stable Zn^{II}-complexes (for example, NOTA) is added.

^{68}Ga Radiochemistry. In a preliminary experiment, ^{68}Ga-labeling of NOPO and NOPO-conjugates was already proven to proceed extraordinarily efficiently. Full ^{68}Ga incorporation was achieved at 0.1 μM concentration of the chelator, labeling at pH 2.8 and 95 °C for 5 min, allowing routine production of NOPO radiopharmaceuticals with specific activities of >5000 GBq/μmol.[13] In order to complement these data, ^{68}Ga-labeling was investigated at room temperature, where NOPO can be labeled virtually quantitatively at pH 3–4 (Figure 4). At 95 °C, quantitative ^{68}Ga incorporation is observed between pH 0.5 and 7. In contrast to carboxylate chelators, labeling in highly acidic media is possible due to the low pK_a of the phosphinic acid moieties (see Table 1 and Figure 2). At pH < 1, these are still present mainly in deprotonated form and therefore able to form complexes with metal ions. However, a particularly interesting feature of NOPO is the ability to readily label at pH values substantially higher than 5. In this pH region, formation of colloidal $Ga(OH)_3$[43] or Ga(O)OH[44] is usually favored, particularly at temperatures around the boiling point of water, which seriously hampers formation of $^{68}Ga^{III}$ chelates. NOPO is apparently capable of largely inhibiting hydroxide polymerization and/or dehydration, either due to very fast chelation of hexaaqua-Ga^{III} complex, or due to an ability of ligand exchange with initially formed, monomeric Ga^{III}-hydroxido species.

In view of the formation of phosphilactones during NOPO conjugation, we were interested whether these structures are suitable for ^{68}Ga-labeling as well. Apart from cleavage of the intramolecular ester during labeling, Ga^{III} complexation by an intact phosphilactone also appears a plausible scenario, because in this structure, five of the six major coordination sites are unchanged and available. However, our previously published data already indicated that, at conditions commonly employed for automated ^{68}Ga-labeling, Ga^{III} complexation by NOPO-NOC in its phosphilactone form (for structure see Supporting Information, Scheme S1) readily occurred with simultaneous cleavage of the intramolecular ester; formation of the Ga^{III}-complex of regular NOPO-NOC was confirmed by MS.[13] For more detailed characterization, the concentration dependency of ^{68}Ga-labeling of phosphilactone-NOPO-NOC was determined. Figure 4 reveals that labeling efficiency of this precursor is comparable to NODAGA-peptides,[31] which allows for the conclusion that formation of intramolecular esters of NOPO never constitutes a fundamental problem for Ga^{III} complexation because functionality of the precursors is always granted.

Preclinical Studies. Proof-of-concept for applicability of NOPO in ^{68}Ga-peptides was delivered using aforementioned ^{68}Ga–NOPO–NOC,[13] a conjugate of NOPO with the octreotide-analogue NaI^3-octreotide (for structure, see Supporting Information, Scheme S1).[45] In form of its ^{68}Ga-labeled DOTA conjugate ^{68}Ga–DOTA–NOC,[46] the latter is currently being successfully applied for clinical PET imaging of neuroendocrine tumors.[2]

Especially when compared to the corresponding NODAGA analogues, NOPO conjugates tend to display a higher hydrophilicity, because unlike DOTA conjugates, the NOTA motif in NODAGA conjugates does not retain a non-coordinating, hydrophilic carboxylate upon Ga^{III} complexation. The inherently higher polarity of phosphinates compared to carboxylates is further enhanced by the two noncoordinating hydroxyl groups. A striking example is provided by ^{68}Ga-NODAGA-c(RGDfK)[47] and ^{68}Ga-NOPO-c(RGDfK),[24] wherein the metal chelates have a particularly pronounced impact on overall polarities due to the small size of the cyclic pentapeptide c(RGDfK), resulting in markedly different log D values of −3.27 and −4.64, respectively. Although not being statistically significant, a similar trend is observed for ^{68}Ga–NOPO–NOC and ^{68}Ga–DOTA–NOC (log D = −1.82 ± 0.11 and −1.75 ± 0.16 at pH 7.4, respectively).

^{68}Ga–NOPO–NOC was prepared in a fully automated GMP-compliant synthesis as described before[13] and evaluated in CD-1 athymic nude mice bearing AR42J (sst2-overexpressing rat pancreatic carcinoma) xenografts. The biodistribution profile shows high tumor uptake of ^{68}Ga–NOPO–NOC and low uptake in other organs and tissues (Figure 5). The intermediate kidney uptake is considered to be excretion-related; however, it might also result partly from reabsorption in microtubuli,[48] since no kidney protection was performed. Specificity was proven by administration of a blocking dose of ^{nat}Ga–NOPO–NOC (5 mg per kg body weight) 10 min prior to the tracer injection, which markedly reduced uptake in the tumor, pancreas, and stomach (for complete experimental data in numerical form, including tumor-to-organ ratios, see Supporting Information, Tables S3 and S4).

Appendix B

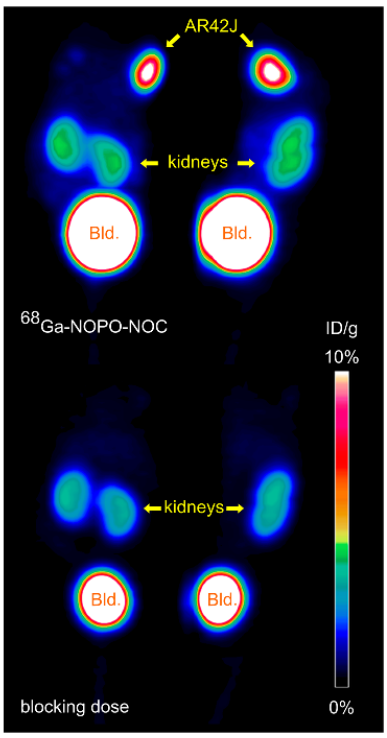

Figure 6. PET images (MIP, 75 min p.i.) of AR42J (rat pancreatic carcinoma) xenografts, dorsal (left) and sagittal (right) views. Top: ^{68}Ga−NOPO−NOC, bottom: ^{68}Ga−NOPO−NOC + blocking dose (5 mg of ^{nat}Ga−NOPO−NOC per kg body weight). "Bld." = bladder.

Both the biodistribution pattern (Figure 5) and the results of microPET imaging at 75 min p.i. (Figure 6) demonstrate clear tumor visualization and a very low background. In addition, ^{68}Ga−NOPO−NOC can be considered metabolically stable as only intact tracer was found in blood, liver, kidneys, and urine at 30 min p.i. (see Supporting Information, Table S5 and Figure S9).

■ CONCLUSION

In summary, the bifunctional triazacyclononane-based triphosphinate chelator NOPO was characterized in terms of protonation constants, solution structures of its Ga^{III} complexes, bioconjugation by amide formation, and ^{68}Ga labeling properties. An improved synthesis is reported, yielding the compound in 45% overall yield based on benzyl-TACN. Interestingly, an intramolecular phosphinic acid ester (a phosphilactone) is formed during amide functionalization on the single distal carboxylic acid moiety; this reaction can be prevented by previous formation of the zinc(II) complex. Cleavage of the phosphilactone occurs spontaneously during ^{68}Ga labeling, but it can also be hydrolyzed under moderately acidic conditions, for example, using TFA at ambient temperature. ^{68}Ga-labeling of NOPO is virtually quantitative at room temperature between pH 3 and 4 (30 μM) and at 95 °C over the range of pH 0.5−7 (10 μM). The ^{68}Ga-labeled NaI^3-octreotide conjugate ^{68}Ga−NOPO−NOC proved suitable for preclinical imaging of sst2-receptor-positive tumors, showing high tumor and low organ uptake. In addition, NOPO-functionalized compounds tend to be more hydrophilic than corresponding DOTA- and NODAGA-conjugates.

We conclude that NOPO is a highly useful bifunctional Ga^{III} chelator, particularly for application in ^{68}Ga-labeled PET radiopharmaceuticals, notwithstanding the fact that phosphilactones, which are obtained as primary conjugation products, could occasionally require further treatment to release the free NOPO conjugate. The excellent ^{68}Ga-labeling properties of NOPO facilitate implementation of kit-like labeling protocols at room temperature. Moreover, the hydrophilicity of NOPO-conjugates, fostering renal excretion, and the high in vivo stability of the corresponding ^{68}Ga complexes render NOPO an outstanding chelator for future ^{68}Ga-labeled radiopharmaceuticals.

■ ASSOCIATED CONTENT

Supporting Information

Experimental details on the alternative synthesis of NOPO, more potentiometric and NMR data for the Ga^{III}−NOPO system, figures showing formation of phosphilactones with other substrates, quality control of labeled conjugates, biodistribution tables, and data on in vivo conjugate stability. This material is available free of charge via the Internet at http://pubs.acs.org.

■ AUTHOR INFORMATION

Corresponding Author

*Phone: +49 89 4140 6333; fax: +49 89 4140 6493; e-mail: johannes.notni@tum.de.

Author Contributions

J.S. and O.Z. contributed equally.

Notes

The authors declare no competing financial interest.

■ ACKNOWLEDGMENTS

The authors thank Jana Havlíčková (Charles University) for potentiometry service, Katharina McGuire, Christina Lesti, Sybille Reder, Markus Mittelhäuser, and Marco Lehmann (TUM) for assistance with cell cultures and animal experiments, and the Deutsche Forschungsgemeinschaft (NO822/4-1 and SFB 824, projects Z1 and B5) and the Grant Agency of the Czech Republic (No. 13-08336S and TA03010878) for financial support.

■ REFERENCES

(1) (a) Decristoforo, C.; Pickett, R. D.; Verbruggen, A. Feasibility and availability of ^{68}Ga-labelled peptides. *Eur. J. Nucl. Med. Mol. Imaging* **2012**, *39*, S31−40. (b) Velikyan, I. Positron emitting [^{68}Ga]Ga-based imaging agents: chemistry and diversity. *Med. Chem.* **2011**, *7*, 345−379.

(2) (a) Breeman, W. A. P.; de Blois, E.; Chan, H. S.; Konijnenberg, M.; Kwekkeboom, D. J.; Krenning, E. P. ^{68}Ga-labeled DOTA-peptides and ^{68}Ga-labeled radiopharmaceuticals for positron emission tomography: current status of research, clinical applications, and future perspectives. *Semin. Nucl. Med.* **2011**, *41*, 314−321. (b) Fani, M.; Andre, J. P.; Maecke, H. R. ^{68}Ga-PET: a powerful generator-based alternative to cyclotron-based PET radiopharmaceuticals. *Contrast Media Mol. Imaging* **2008**, *3*, 67−77.

(3) (a) Demmer, O.; Gourni, E.; Schumacher, U.; Kessler, H.; Wester, H. J. PET Imaging of CXCR4 Receptors in Cancer by a New Optimized Ligand. *ChemMedChem* **2011**, *6*, 1789−1791. (b) Gourni, E.; Demmer, O.; Schottelius, M.; D'Alessandria, C.; Schulz, S.;

Dijkgraaf, I.; Schumacher, U.; Schwaiger, M.; Kessler, H.; Wester, H. J. PET of CXCR4 Expression by a Ga-68-Labeled Highly Specific Targeted Contrast Agent. *J. Nucl. Med.* **2011**, *52*, 1803−1810.

(4) Notni, J.; Pohle, K.; Wester, H. J. Be spoilt for choice with radiolabelled RGD peptides: preclinical evaluation of ^{68}Ga-TRAP-(RGD)$_3$. *Nucl. Med. Biol.* **2013**, *40*, 33−41.

(5) (a) Eder, M.; Schäfer, M.; Bauder-Wüst, U.; Hull, W. E.; Wängler, C.; Mier, W.; Haberkorn, U.; Eisenhut, M. Ga-68-Complex Lipophilicity and the Targeting Property of a Urea-Based PSMA Inhibitor for PET Imaging. *Bioconjugate Chem.* **2012**, *23*, 688−697. (b) Afshar-Oromieh, A.; Malcher, A.; Eder, M.; Eisenhut, M.; Linhart, H. G.; Hadaschik, B. A.; Holland-Letz, T.; Giesel, F. L.; Kratochwil, C.; Haufe, S.; Haberkorn, U.; Zechmann, C. M. PET imaging with a [Ga-68]gallium-labelled PSMA ligand for the diagnosis of prostate cancer: biodistribution in humans and first evaluation of tumour lesions. *Eur. J. Nucl. Med. Mol. Imaging* **2013**, *40*, 486−495.

(6) (a) Lin, M.; Rangahatan, D.; Mori, T.; Hagooly, A.; Rossin, R.; Welch, M. J.; Lapi, S. E. Long-term evaluation of TiO_2-based ^{68}Ge/^{68}Ga generators and optimized automation of [^{68}Ga]-DOTATOC radiosynthesis. *Appl. Radiat. Isot.* **2012**, *70*, 2539−2544. (b) de Blois, E.; Chan, H. S.; Naidoo, C.; Prince, D.; Krenning, E. P.; Breeman, W. A. P. Characteristics of SnO2-based 68Ge/68Ga generator and aspects of radiolabelling DOTA-peptides. *Appl. Radiat. Isot.* **2011**, *69*, 308−315.

(7) Notni, J. With Gallium into a New Era? *Nachr. Chem.* **2012**, *60*, 645−649.

(8) Wester, H. J. GMP-Production − Shaping the Future. *Nuklearmedizin* **2012**, *51*, N1−N4.

(9) (a) Bartholomä, M. D. Recent developments in the design of bifunctional chelators for metal-based radiopharmaceuticals used in Positron Emission Tomography. *Inorg. Chim. Acta* **2012**, *389*, 36−51. (b) Zeglis, B. M.; Lewis, J. S. A practical guide to the construction of radiometallated bioconjugates for positron emission tomography. *Dalton Trans.* **2011**, *40*, 6168−6195. (c) Wadas, T.; Wong, E. H.; Weisman, G. R.; Anderson, C. J. Coordinating Radiometals of Copper, Gallium, Indium, Yttrium, and Zirconium for PET and SPECT Imaging of Disease. *Chem. Rev.* **2010**, *110*, 2858−2902.

(10) Luyt, L. G.; Katzenellenbogen, J. A. A trithiolate tripodal bifunctional ligand for the radiolabeling of peptides with gallium(III). *Bioconjugate Chem.* **2002**, *13*, 1140−1145.

(11) Notni, J.; Pohle, K.; Peters, J. A.; Görls, H.; Platas-Iglesias, C. Structural study of Ga(III), In(III), and Fe(III) complexes of triazamacrocycle based ligands with N_3S_3 donor set. *Inorg. Chem.* **2008**, *48*, 3257−3267.

(12) Notni, J.; Hermann, P.; Havlíčková, J.; Kotek, J.; Kubíček, V.; Plutnar, J.; Loktionova, N.; Riss, P. J.; Rösch, F.; Lukeš, I. A triazacyclononane-based bifunctional phosphinate ligand for the preparation of multimeric ^{68}Ga tracers for positron emission tomography. *Chem.—Eur. J.* **2010**, *16*, 7174−7185.

(13) Šimeček, J.; Zemek, O.; Hermann, P.; Wester, H. J.; Notni, J. A monoreactive bifunctional triazacyclononane phosphinate chelator with high selectivity for gallium-68. *ChemMedChem* **2012**, *7*, 1375−1378.

(14) Andre, J. P.; Maecke, H. R.; Zehnder, M.; Macko, L.; Akyel, G. K. 1,4,7-Triazacyclononane-1-succinic acid-4,7-diacetic acid (NODA-SA): a new bifunctional chelator for radiogallium-labelling of biomolecules. *Chem. Commun.* **1998**, 1301−1302.

(15) Eisenwiener, K.-P.; Prata, M. I. M.; Buschmann, I.; Zhang, H.-W.; Santos, A. C.; Wenger, S.; Reubi, J. C.; Maecke, H. R. NODAGATOC, a New Chelator-Coupled Somatostatin Analogue Labeled with [$^{67/68}$Ga] and [^{111}In] for SPECT, PET, and Targeted Therapeutic Applications of Somatostatin Receptor (hsst2) Expressing Tumors. *Bioconjugate Chem.* **2002**, *13*, 530−541.

(16) Riss, P. J.; Kroll, C.; Nagel, V.; Rösch, F. NODAPA-OH and NODAPA-(NCS)n: Synthesis, ^{68}Ga-radiolabelling and in vitro characterisation of novel versatile bifunctional chelators for molecular imaging. *Bioorg. Med. Chem. Lett.* **2008**, *18*, 5364−5367.

(17) (a) Singh, A. N.; Liu, W.; Hao, G.; Kumar, A.; Gupta, A.; Oz, O. K.; Hsieh, J.-T.; Sun, X. Multivalent bifunctional chelator scaffolds for gallium-68 based positron emission tomography imaging probe design: signal amplification via multivalency. *Bioconjugate Chem.* **2011**, *22*, 1650−1662. (b) Guerra Gomez, F. L.; Uehara, T.; Rokugawa, T.; Higaki, Y.; Suzuki, H.; Hanaoka, H.; Akizawa, H.; Arano, Y. Synthesis and evaluation of diastereoisomers of 1,4,7-triazacyclononane-1,4,7-tris-(glutaric acid) (NOTGA) for multimeric radiopharmaceuticals of gallium. *Bioconjugate Chem* **2012**, *23*, 2229−−2238..

(18) (a) Waldron, B. P.; Parker, D.; Burchardt, C.; Yufit, D. S.; Zimny, M.; Roesch, F. Structure and stability of hexadentate complexes of ligands based on AAZTA for efficient PET labelling with gallium-68. *Chem. Commun.* **2013**, *49*, 579−581. (b) Baranyai, Z.; Uggeri, F.; Maiocchi, A.; Giovenzana, G. B.; Cavallotti, C.; Takács, A.; Tóth, I.; Bányai, I.; Bényei, A.; Brücher, E.; Aime, S. Equilibrium, Kinetic and Structural Studies of AAZTA Complexes with Ga^{3+}, In^{3+} and Cu^{2+}. *Eur. J. Inorg. Chem.* **2013**, 147−162. (c) Gugliotta, G.; Botta, M.; Tei, L. AAZTA-based bifunctional chelating agents for the synthesis of multimeric/dendrimeric MRI contrast agents. *Org. Biomol. Chem.* **2010**, *8*, 4569−4574.

(19) (a) Ferreirós-Martínez, R.; Esteban-Gómez, D.; Platas-Iglesias, C.; de Blas, A.; Rodríguez-Blas, T. Zn(II), Cd(II) and Pb(II) complexation with pyridinecarboxylate containing ligands. *Dalton Trans.* **2008**, 5754−5765. (b) Boros, E.; Ferreira, C. L.; Cawthray, J. F.; Price, E. W.; Patrick, B. O.; Wester, D. W.; Adam, M. J.; Orvig, C. Acyclic Chelate with Ideal Properties for ^{68}Ga PET Imaging Agent Elaboration. *J. Am. Chem. Soc.* **2010**, *132*, 15726−15733. (c) Boros, E.; Ferreira, C. L.; Yapp, D. T. T.; Gill, R. K.; Price, E. W.; Adam, M. J.; Orvig, C. RGD conjugates of the H_2dedpa scaffold: synthesis, labeling and imaging with ^{68}Ga. *Nucl. Med. Biol.* **2012**, *29*, 785−794.

(20) (a) Zöller, M.; Schuhmacher, J.; Reed, J.; Maier-Borst, W.; Matzku, S. Establishment and Characterization of Monoclonal Antibodies Against an Octahedral Gallium Chelate Suitable for Immunoscintigraphy with PET. *J. Nucl. Med.* **1992**, *33*, 1366−1372. (b) Eder, M.; Wängler, B.; Knackmuss, S.; LeGall, F.; Little, M.; Haberkorn, U.; Mier, W.; Eisenhut, M. Tetrafluorophenolate of HBED-CC: a versatile conjugation agent for ^{68}Ga-labeled small recombinant antibodies. *Eur. J. Nucl. Med. Mol. Imaging* **2008**, *35*, 1878−1886.

(21) Berry, D. J.; Ma, Y.; Ballinger, J. R.; Tavaré, R.; Koers, A.; Sunassee, K.; Zhou, T.; Nawaz, S.; Mullen, G. E. D.; Hider, R. C.; Blower, P. J. Efficient bifunctional gallium-68 chelators for positron emission tomography: tris(hydroxypyridinone) ligands. *Chem. Commun.* **2011**, *47*, 7068−7070.

(22) (a) Tircsó, G.; Benyó, E. T.; Suh, E. H.; Jurek, P.; Kiefer, G. E.; Sherry, A. D.; Kovaćs, Z. (S)-5-(p-Nitrobenzyl)-PCTA, a Promising Bifunctional Ligand with Advantageous Metal Ion Complexation Kinetics. *Bioconjugate Chem.* **2009**, *20*, 565−575. (b) Ferreira, C. L.; Yapp, D. T. T.; Mandel, D.; Gill, R. K.; Boros, E.; Wong, M. Q.; Jurek, P.; Kiefer, G. E. ^{68}Ga Small Peptide Imaging: Comparison of NOTA and PCTA. *Bioconjugate Chem.* **2012**, *23*, 2239−2246.

(23) Desreux, J. F. Nuclear magnetic resonance spectroscopy of lanthanide complexes with a tetraacetic tetraaza macrocycle. Unusual conformation properties. *Inorg. Chem.* **1980**, *19*, 1319−1324.

(24) Šimeček, J.; Wester, H. J.; Notni, J. Copper-64 labelling of triazacyclononane-triphosphinate chelators. *Dalton Trans.* **2012**, *41*, 13803−13806.

(25) Maheshwari, V.; Dearling, J. L. J.; Treves, S. T.; Packard, A. B. Measurement of the rate of copper(II) exchange for copper-64 complexes of bifunctional chelators. *Inorg. Chim. Acta* **2012**, *393*, 318−323.

(26) (a) Wieghardt, K.; Bossek, U.; Chaudhuri, P.; Herrmann, W.; Menke, B. C.; Weiss, J. 1,4,7-Triazacyclononane-N,N′,N″-triacetate, a Hexadentate Ligand for Divalent and Trivalent Metal Ions. Crystal Structures of [Cr^{III}(TCTA)], [Fe^{III}(TCTA)], and Na[Cu^{III}(TCTA)]·2NaBr·8H_2O. *Inorg. Chem.* **1982**, *21*, 4308−4314. (b) Broan, C. J.; Cox, J. P.; Craig, A. S.; Kataky, R.; Parker, D.; Harrison, A.; Randall, A.; Ferguson, G. J. Structure and Solution Stability of Indium and Gallium Complexes of 1,4,7-Triazacyclononanetriacetate and of Yttrium Complexes of 1,4,7,10-Tetraazacyclododecanetetraacetate and Related Ligands: Kinetically Stable Complexes for Use in Imaging and

Appendix B

Radioimmunotherapy. X-Ray Molecular Structure of the Indium and Gallium Complexes of 1,4,7-Triazacyclononane-1,4,7-triacetic Acid. *J. Chem. Soc., Perkin Trans.* **1991**, *1*, 87−99.

(27) Šimeček, J.; Schulz, M.; Notni, J.; Plutnar, J.; Kubíček, V.; Havlíčková, J.; Hermann, P. Complexation of Metal Ions with TRAP (1,4,7-Triazacyclononane Phosphinic Acid) Ligands and 1,4,7-Triazacyclononane-1,4,7-triacetic Acid: Phosphinate-Containing Ligands as Unique Chelators for Trivalent Gallium. *Inorg. Chem.* **2012**, *51*, 577−590.

(28) (a) Bazakas, K.; Lukeš, I. Synthesis and complexing properties of polyazamacrocycles with pendant N-methylenephosphinic acid. *J. Chem. Soc., Dalton Trans.* **1995**, 1133−1137. (b) Cole, E.; Parker, D.; Ferguson, G.; Gallagher, J. F.; Kaitner, B. Synthesis and Structure of Chiral Metal Complexes of Polyazacycloalkane Ligands Incorporating Phosphinic Acid Donors. *J. Chem. Soc., Chem. Commun.* **1991**, 1473−1475. (c) Broan, C. J.; Cole, E.; Jankowski, K. J.; Parker, D.; Pulukkody, K.; Boyce, B. A.; Beeley, N. R. A.; Millar, K.; Millican, A. T. Synthesis of New Macrocyclic Amino-Phosphinic Acid Complexing Agents and Their C-and P-Functionalised Derivatives for Protein Linkage. *Synthesis* **1992**, 63−68. (d) Broan, C. J.; Jankowski, K. J.; Kataky, R.; Parker, D. Synthesis and Complex Stability of Parent and C-Functionalised Derivatives of 1,4,7-Triazacyclononane-1,4,7-tris-[methylene(methylphosphinic acid)]: an Effective New Complexing Agent. *J. Chem. Soc., Chem. Commun.* **1990**, *23*, 1738−1739. (e) Cole, E.; Copley, R. C. B.; Howard, J. A. K.; Parker, D.; Ferguson, G.; Gallagher, J. F.; Kaitner, B.; Harrison, A.; Royle, L. 1,4,7-Triazacyclononane-1,4,7-triyltrimethylenetris-(phenylphosphinate) enforces Octahedral Geometry: Crystal and Solution Structures of its Metal Complexes and Comparative Biodistribution Studies of Radiolabelled Indium and Gallium Complexes. *J. Chem. Soc., Dalton Trans.* **1994**, 1619−1625.

(29) Notni, J.; Šimeček, J.; Hermann, P.; Wester, H. J. TRAP, a Powerful and Versatile Framework for Gallium-68 Radiopharmaceuticals. *Chem.—Eur. J.* **2011**, *17*, 14718−14722.

(30) Notni, J.; Pohle, K.; Wester, H. J. Comparative gallium-68 labeling of TRAP-, NOTA-, and DOTA-peptides: practical consequences for the future of gallium-68-PET. *EJNMMI Res.* **2012**, *2*, 28.

(31) Šimeček, J.; Hermann, P.; Wester, H. J.; Notni, J. How is ^{68}Ga Labeling of Macrocyclic Chelators Influenced by Metal Ion Contaminants in ^{68}Ge/^{68}Ga Generator Eluates? *ChemMedChem* **2013**, *8*, 95−103.

(32) (a) Notni, J.; Hermann, P.; Dregely, I.; Wester, H. J. Convenient Synthesis of Gallium-68 Labeled Gadolinium(III) complexes: Towards Bimodal Responsive Probes for Functional Imaging with PET/MRI. *Chem.—Eur. J.* **2013**, *19*, 12602−12606. (b) Notni, J.; Hermann, P.; Dregely, I.; Wester, H. J. Simultaneous in vivo PET/MRI imaging with a bi-metal bimodal tracer: Towards 68Ga-labeled responsive gadolinium contrast agents. *J. Label. Compd. Radiopharm.* **2013**, *56*, S62. (c) Notni, J.; Hermann, P.; Dregely, I.; Schwaiger, M.; Wester, H. J. Convenient Route towards Gallium-68 Labelled Gadolinium Contrast Agents for Simultaneous in vivo PET/MR Imaging. *Eur. J. Nucl. Med. Mol. Imaging* **2013**, *40*, S229.

(33) Notni, J.; Plutnar, J.; Wester, H. J. Bone-seeking TRAP conjugates: surprising observations and their implications on the development of gallium-68-labeled bisphosphonates. *EJNMMI Res.* **2012**, *2*, 13.

(34) Řezanka, P.; Kubíček, V.; Hermann, P.; Lukeš, I. Synthesis of a Bifunctional Monophosphinate DOTA Derivative Having a Free Carboxylate Group in the Phosphorus Side Chain. *Synthesis* **2008**, 1431−1435.

(35) Försterová, M.; Svobodová, I.; Lubal, P.; Táborský, P.; Kotek, J.; Hermann, P.; Lukeš, I. Thermodynamic study of lanthanide(III) complexes with bifunctional monophosphinic acid analogues of H_4dota and comparative kinetic study of yttrium(III) complexes. *Dalton Trans.* **2007**, 535−549.

(36) (a) Kývala, M.; Lukeš, I. *International Conference Chemometrics '95*, Pardubice, Czech Republic, Aug 2−Sep 2, 1995; p 63; (b) Kývala, M.; Lubal, P.; Lukeš, I. *IX. Spanish-Italian and Mediterranean Congress on Thermodynamics of Metal Complexes (SIMEC 98)*, Girona, Spain, Jun 2−5, 1998. The full version of the OPIUM program is available (free of charge) on http://www.natur.cuni.cz/~kyvala/opium.html.

(37) (a) Martell, A. E.; Smith, R. M. *Critical Stability Constants*, Vols. *1*−*6*; Plenum Press: New York, 1974−1989; (b) *NIST Standard Reference Database 46* (Critically Selected Stability Constants of Metal Complexes), Version 7.0; National Institute of Standards and Technology: Gaithersburg, MD, 2003; (c) Baes, C. F.; Mesmer, R. E. *The Hydrolysis of Cations*; Wiley: New York, 2003.

(38) Schottelius, M.; Wester, H. J.; Senekowitsch-Schmidtke, R.; Schwaiger, M. Improvement of pharmacokinetics of radioiodinated Tyr^3-octreotide by conjugation with carbohydrates. *Bioconjugate Chem.* **2002**, *13*, 1021−1030.

(39) Moedritzer, K.; Irani, R. R. The Direct Synthesis of α-Aminomethylphosphonic Acids. Mannich-Type Reactions with Orthophosphorous Acid. *J. Org. Chem.* **1966**, *31*, 1603−1607.

(40) Remore, D. Chemistry of phosphorous acid: new routes to phosphonic acids and phosphate esters. *J. Org. Chem.* **1978**, *43*, 992−996.

(41) Drahoš, B.; Kubíček, V.; Bonnet, C. S.; Hermann, P.; Lukeš, I.; Tóth, É. Dissociation kinetics of Mn^{2+} complexes of NOTA and DOTA. *Dalton Trans.* **2011**, *40*, 1945−1951.

(42) Akitt, J. W.; Kettle, D. ^{71}Ga nuclear magnetic resonance investigation of aqueous gallium(III) and its hydrolysis. *Magn. Reson. Chem.* **1989**, *27*, 377−379.

(43) Hacht, B. Gallium(III) Ion Hydrolysis under Physiological Conditions. *Bull. Korean Chem. Soc.* **2008**, *29*, 372−376.

(44) Uchida, M.; Okuwaki, A. Potentiometric Determination of the First Hydrolysis Constant of Gallium(III) in NaCl Solution to 100 °C. *J. Solution Chem.* **1998**, *27*, 965−978.

(45) Wild, G. J.; Schmitt, S.; Ginj, M.; Maecke, H. R.; Bernard, B. F.; Krenning, E.; de Jong, M.; Wengner, S.; Reubi, J. C. DOTA-NOC, a high-affinity ligand of somatostatin receptor subtypes 1, 3 and 5 for labelling with various radiometals. *Eur. J. Nucl. Med. Mol. Imaging* **2003**, *30*, 1338−1347.

(46) Antunes, P.; Ginj, M.; Zhang, H.; Waser, B.; Baum, R. P.; Reubi, J. C.; Maecke, H. R. Are radiogallium-labelled DOTA-conjugated somatostatin analogues superior to those labelled with other radiometals? *Eur. J. Nucl. Med. Mol. Imaging* **2007**, *34*, 982−993.

(47) Dumont, R. A.; Deininger, F.; Haubner, R.; Maecke, H. R.; Weber, W. A.; Fani, M. Novel ^{64}Cu- and ^{68}Ga-Labeled RGD Conjugates Show Improved PET Imaging of $\alpha_v\beta_3$ Integrin Expression and Facile Radiosynthesis. *J. Nucl. Med.* **2011**, *52*, 1276−1284.

(48) Rolleman, E. J.; Melis, M.; Valkema, R.; Boerman, O. C.; Krenning, E. P.; de Jong, M. Kidney protection during peptide receptor radionuclide therapy with somatostatin analogues. *Eur. J. Nucl. Med. Mol. Imaging* **2010**, *37*, 1018−1031.

Appendix B

Table of contents

Appendix B

1. Synthesis of NOPO via reactions e and f (Figure 3)

2-(carboxyethyl)phosphinic acid (**6**, 0.13 g, 0.9 mmol) was dissolved in hexamethyldisilazane (HMDS, 5 mL), the glassware was purged with argon, and the solution was heated to 130 °C for 24 h. Strictly inert atmosphere and moisture-free conditions are the crucial criterion for quantitative conversion of **6** to **7**. The reaction was monitored by ^{31}P NMR (a doublet at $\delta = 37$ ppm disappears, and a singlet belonging to **7** is observed around $\delta = 160$ ppm). **4** (0.10 g, 0.29 mmol) was dissolved by heating with HMDS at 130°C under argon atmosphere and the reaction mixture containing **7** was added in one portion with a syringe. Paraformaldehyde (30 mg, 1.0 mmol) was added in one portion, the reaction mixture was stirred for 24 h and then cooled to r.t.. Methanol (5 mL) was added dropwise. Then the reaction mixture was dissolved in water and loaded onto a column filled with cation exchanger (DOWEX 50, H^+-form). NOPO was eluted with water in neutral fraction, which was evaporated and freeze-dried. Yield 70 mg, 47%.

2. Potentiometry

Water ionic product pK_w (13.81) and values of stability constants for the metal-hydroxide complexes were taken from literature.[1] During potentiometric titrations, Ga^{3+} ion was complexed with NOPO immediately after mixing of the reactants and the complex was fully formed even in the beginning of titration in acidic solution (pH ~1.6) similarly to other TRAP ligands. Thus, the complex stability constant was determined by competition with tetrahydroxidogallate in alkaline region. The determined overall constants, β_{HhGaL}, are presented in Table S2 together with errors as given by the fitting. Stability constant values of the TACN-based ligands correlate well with basicity of the ring nitrogen atoms (given as $\log K_1 + \log K_2$), Figure S1. Protons in the protonated species should be attached to the pendant arm oxygen atoms similarly to other Ga^{III} complexes with TRAP ligands.

Table S1: Experimentally determined overall protonation constants ($\log \beta_{HhL}$) of NOPO (25 °C, $I = 0.1$ M $(Me_4N)Cl$).

Constant	NOPO
$\log \beta_{HL}$	11.967(7)
$\log \beta_{H2L}$	17.19(1)
$\log \beta_{H3L}$	20.96(1)
$\log \beta_{H4L}$	22.51(2)

Table S2: Experimentally determined overall stability constants, $\log\beta_{HhMmLl}$ ($\beta_{HhMmLl} = [H_hM_mL_l] / [H]^h \times [M]^m \times [L]^l$), for Ga^{III} complexes of NOPO (25 °C, $I = 0.1$ M $(Me_4N)Cl$).

Coefficients	Constant
011	25.0(1)
111	29.4(2)
211	30.6(2)
–111	17.58(8)
–211	7.8(2)

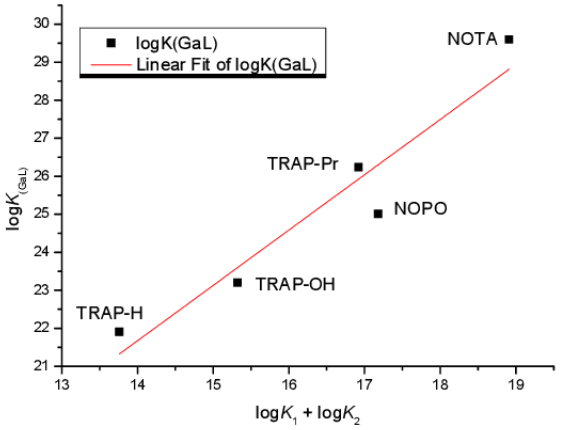

Figure S1: Correlation between ligand basicity and thermodynamic stability of Ga-complexes.

Appendix B

3. NMR studies of Ga-NOPO at different pH

The [Ga(NOPO)] complex was prepared by dissolving equimolar amounts of NOPO and $GaCl_3$ in water. For characterisation, the complex was purified on weak cation exchanger (Amberlite CG-50). The aqueous solution of the complex possessed pH 1.7.

A sample of complex, dissolved in 6 M $HClO_4$, showed no signs of decomposition over the period of three months, monitored by ^{31}P and ^{71}Ga NMR. Base-promoted hydrolysis was assessed from aq. solutions of the complex, adjusted to pH 7.5 and 10.0 by addition of 2 M aq. NaOAc and 2 M aq. NaOH, respectively. Complex concentration in NMR tubes was approximately 0.1 M. Interpretation of NMR data was done by qualitative comparison with the chemical model obtained from potentiometry. A rigorous quantitative comparison is not possible due to presence of buffers and different ionic strength. However, we found that presence of buffers is necessary, because protons are released during slow rearrangement processes of the complex (formation of "out-of-cage" structures, see main text), resulting in a decrease of the initial pH. These rearrangements were found to be fully reversible; acidification of the samples with HCl resulted in formation of the original "in-cage" [Ga(NOPO)] complex.

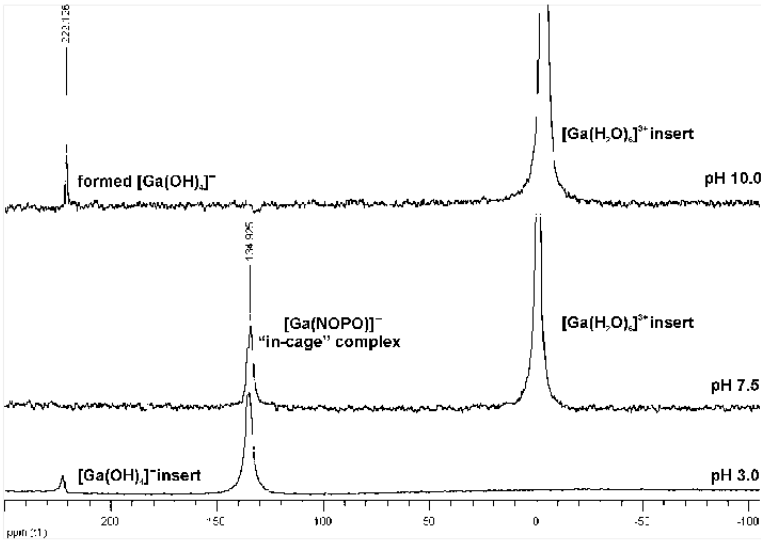

Figure S2: ^{71}Ga NMR spectra of [Ga(NOPO)] at pH 3, 7.5 and 10, referenced to 0.1 M $Ga(NO_3)_3$ ($[Ga(H_2O)_6]$ at $\delta = 0$ ppm) and 0.1 M $[Ga(OH)_4]^-$ in 1 M NaOH ($\delta = 222$ ppm).

4. Coupling chemistry and intramolecular ester formation

In order to explain the observed molecular masses after coupling reactions of NOPO with peptides, resulting in conjugates showing not only loss of m/z = 18 on ESI-MS (water molecule released from peptide bond formation) but another m/z = 18, we employed ^{31}P NMR spectroscopy. We found that treatment of such intermediate with trifluoroacetic acid (TFA) resulted in conjugates with the expected molecular weight.

The chemical shifts were measured relative to 85% aqueous H_3PO_4 (0 ppm) as an external standard. The following ^{31}P NMR experiments were conducted (see Figures S3–S6):

(1) Measuring the chemical shifts of NOPO only in DMSO.
(2) Measuring the same with addition of a non-coordinating base (DIPEA).
(3) Acquisition of ^{31}P NMR spectra after addition of HATU.
(4) The same experiments (1)-(3) with addition of methylamine or L-Phe(OtBu) together with DIPEA.

Furthermore, formation of phosphilactons was inhibited by addition of one equivalent of solid $ZnCl_2$ hexahydrate to NOPO in DMSO prior to the coupling reaction. Figure S7 shows ^{31}P NMR spectra for this reaction sequence on the example of $MeNH_2$. For demetallation, Zn^{II} can be released at pH 2, using excess NOTA as a scavenger, resulting in neat NOPO-conjugates.

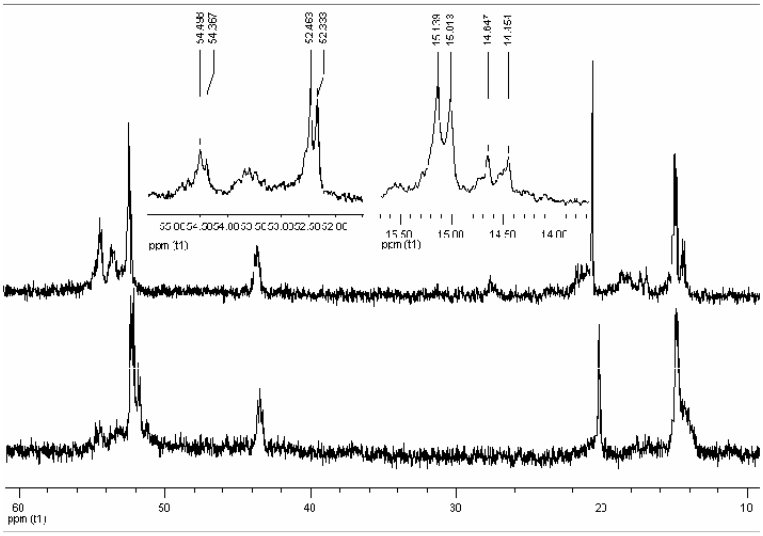

Figure S3: ^{31}P NMR spectra of NOPO, DIPEA and HATU in DMSO, 5 min after mixing (bottom); the same mixture at 5 minutes after addition of $MeHN_2$ (top) with detail on peak pattern.

Appendix B

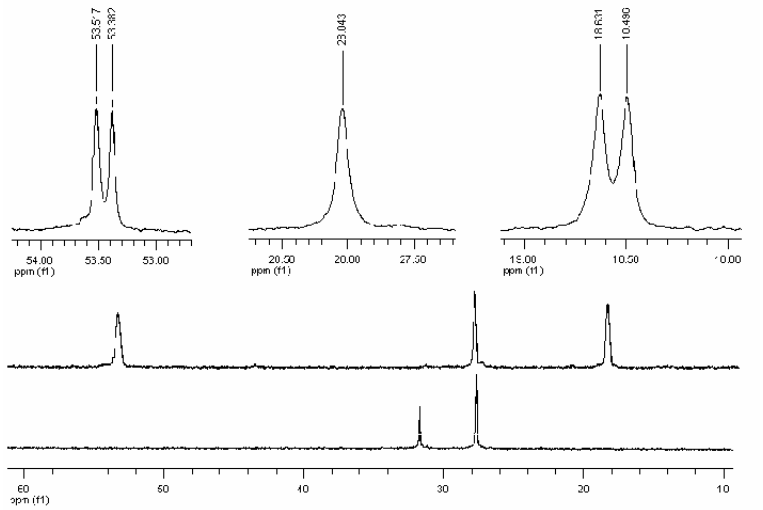

Figure S4: bottom: ^{31}P NMR spectra of NOPO and $MeNH_2$ in DMSO with addition of DIPEA; middle: the same mixture at 5 minutes after addition of HATU; top: peak details. The observed coupling constant of $^{3}J_{PP}$ = 16 Hz is characteristic for a P–CH_2–O–P interaction, e.g. in the intramolecular esters.

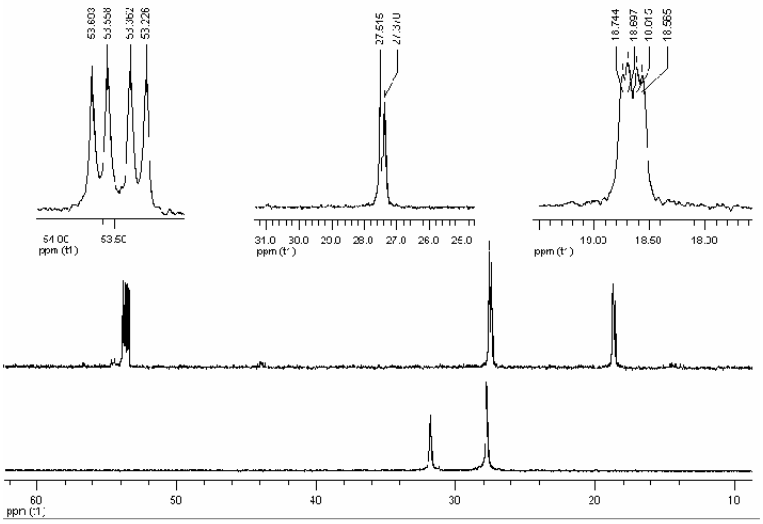

Figure S5: bottom: ^{31}P NMR spectra of NOPO and L-Phe(O*t*Bu) in DMSO with addition of DIPEA; middle: the same mixture at 15 minutes after addition of HATU; top: peak details, showing presence of two diasteromers.

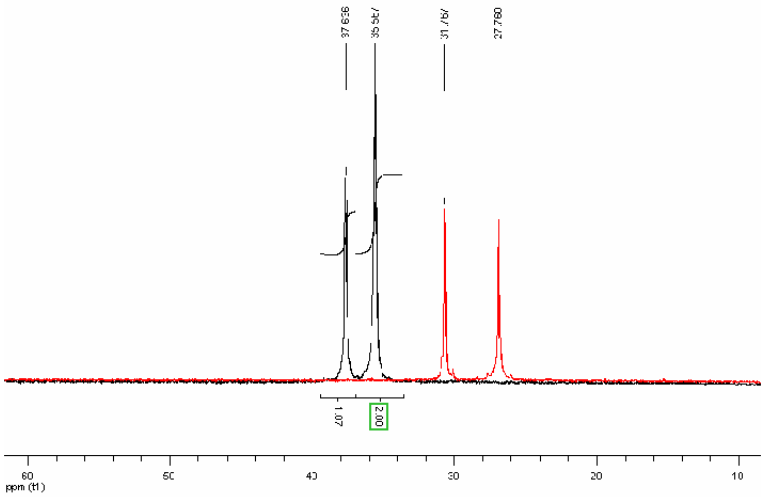

Figure S6: ^{31}P NMR spectra of NOPO in DMSO without (black) and with (red) addition of DIPEA.

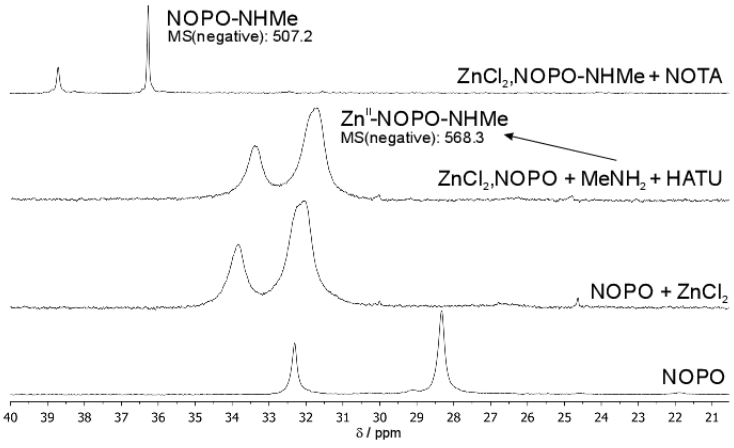

Figure S7: From bottom to top: ^{31}P NMR spectra of NOPO in DMSO with addition of DIPEA; the same mixture after addition of $ZnCl_2$; after addition of $MeNH_2$ and HATU; after demetallation from Zn^{II}, which was done by addition of 10 eq. NOTA at pH 2. The coupling product and its Zn^{II} complex were identified by ESI-MS.

Appendix B

5. Structures of NOPO-NOC and its phosphilactone form

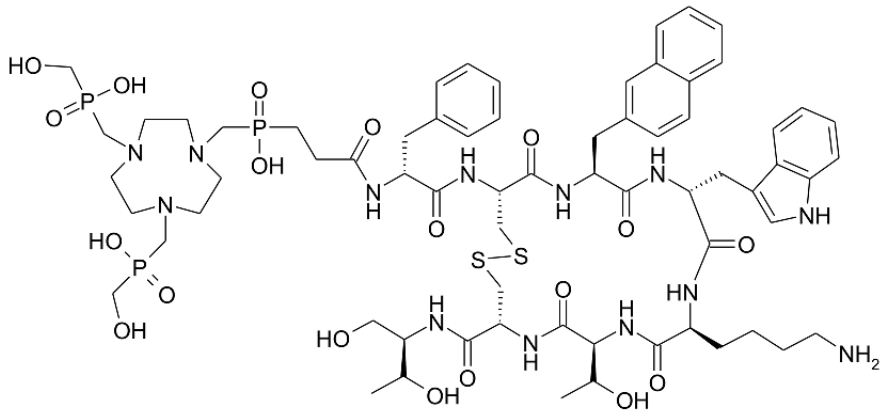

NOPO-NOC

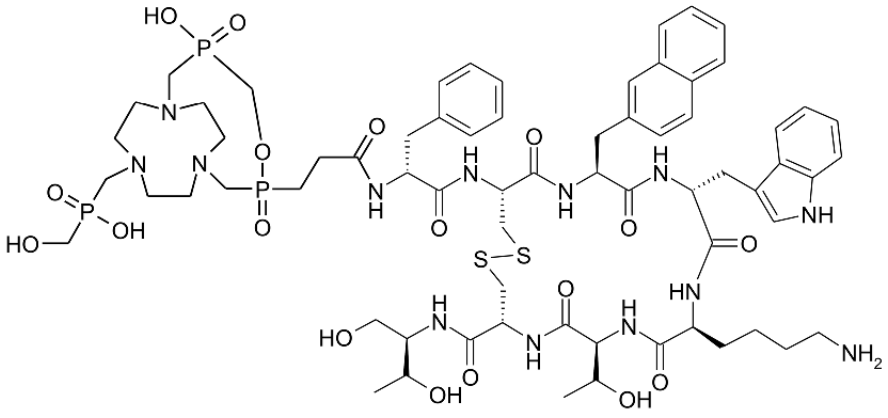

phosphilactone-NOPO-NOC

Scheme S1: Structures of NOPO-NOC and the corresponding phosphilactone, which is formed as the primary product in the course of the coupling reaction.

6. ^{68}Ga-NOPO-NOC analysis

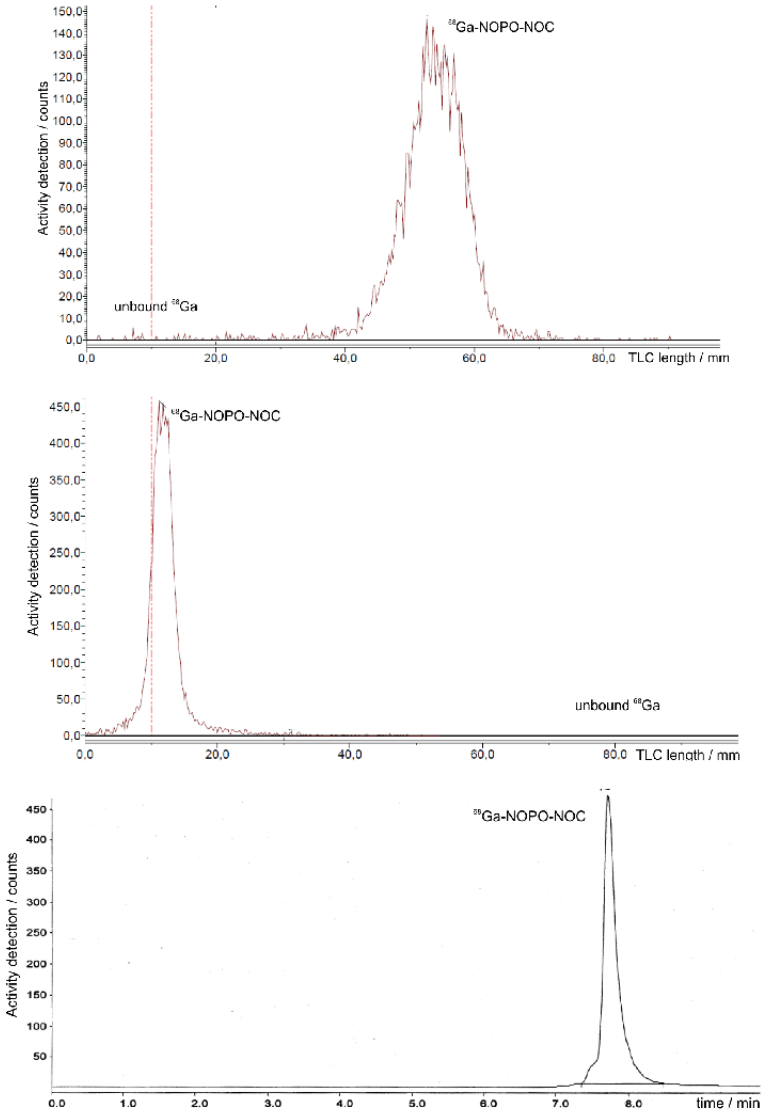

Figure S8: Quality control of ^{68}Ga-NOPO-NOC for injection. TLC on silica-coated paper developed with NH_4OAc/MeOH, 1:1 by volumes (top) and 1 M aq. sodium citrate (middle). Bottom: Radio-HPLC using a C18 column (Chromolith 100 × 4.6 mm); flow rate 2 mL/min; eluents were water and acetonitrile, both containing 0.1% TFA (isocratic elution with 3% MeCN for 2 min, followed by a gradient to 60% MeCN in 6 min and isocratic elution with 95% MeCN for 3 min).

Appendix B

7. Biodistribution

Table S3: Distribution of ^{68}Ga-NOPO-NOC in AR42J xenografted mice at 60 and 120 min p.i. and upon blockade (60 min p.i.) with ^{nat}Ga-NOPO-NOC - 5mg/kg body weight.

	60 min p.i., N = 7			120 min p.i., N = 5			blockade, N = 4		
Tissue	**ID·g^{-1} / %**		**SD**	**ID·g^{-1} / %**		**SD**	**ID·g^{-1} / %**		**SD**
tumour	11.56	±	4.92	13.87	±	4.93	0.87	±	0.38
blood	0.42	±	0.10	0.20	±	0.05	1.08	±	0.46
heart	0.23	±	0.06	0.15	±	0.04	0.58	±	0.27
lung	2.19	±	0.64	1.83	±	0.22	3.91	±	2.59
liver	1.13	±	0.47	0.86	±	0.18	1.62	±	0.69
spleen	0.75	±	0.23	0.51	±	0.07	0.63	±	0.16
pancreas	1.81	±	0.52	2.16	±	0.62	0.29	±	0.13
stomach	2.62	±	1.03	2.48	±	0.77	0.55	±	0.26
small intestine	0.61	±	0.12	0.58	±	0.13	0.84	±	0.52
large intestine	1.31	±	0.35	1.57	±	0.59	0.63	±	0.32
kidney	6.32	±	1.29	9.04	±	1.91	10.59	±	3.22
adrenal gland	0.97	±	0.30	2.18	±	1.79	0.90	±	0.39
muscle	0.18	±	0.12	0.11	±	0.06	0.28	±	0.05
carcass	0.23	±	0.06	0.20	±	0.05	0.44	±	0.16

Table S4: Tumour to background activity uptake ratio calculated from biodistribution of ^{68}Ga-NOPO-NOC in AR42J xenografted mice at 60 and 120 min p.i. and upon blockade.

	60 min p.i., N = 7		120 min p.i., N = 5		blockade, N = 4	
Tissue	**ratio**	**SD**	**ratio**	**SD**	**ratio**	**SD**
tumour	1.00	± 0.00	1.00	± 0.00	1.00	± 0.00
blood	27.36	± 8.47	79.93	± 54.68	0.81	± 0.10
heart	49.63	± 15.59	106.39	± 71.18	1.54	± 0.23
lung	5.55	± 2.43	7.50	± 2.18	0.29	± 0.16
liver	11.41	± 5.05	17.64	± 10.98	0.56	± 0.27
spleen	15.96	± 5.91	28.43	± 14.23	1.33	± 0.42
pancreas	6.65	± 2.50	7.45	± 5.40	2.98	± 0.44
stomach	4.72	± 1.82	6.64	± 4.92	1.65	± 0.35
small intestine	18.90	± 5.97	24.96	± 12.75	1.16	± 0.37
large intestine	8.79	± 2.29	9.79	± 4.90	1.44	± 0.32
kidney	1.81	± 0.59	1.70	± 1.09	0.08	± 0.02
adrenal gland	12.23	± 4.30	9.64	± 6.62	0.99	± 0.36
muscle	85.15	± 48.98	194.54	± 177.48	3.10	± 1.38
carcass	48.57	± 12.12	80.30	± 56.07	1.97	± 0.38

Appendix B

8. In vivo stability

Table S5: Activity extraction efficiencies from tissue homogenates

	Mouse 1	**Mouse 2**	**Mouse 3**	**Mouse 4**
	extracted activity / %			
blood	84	82	86	92
liver	36	21	41	68
kidney	43	64	51	73

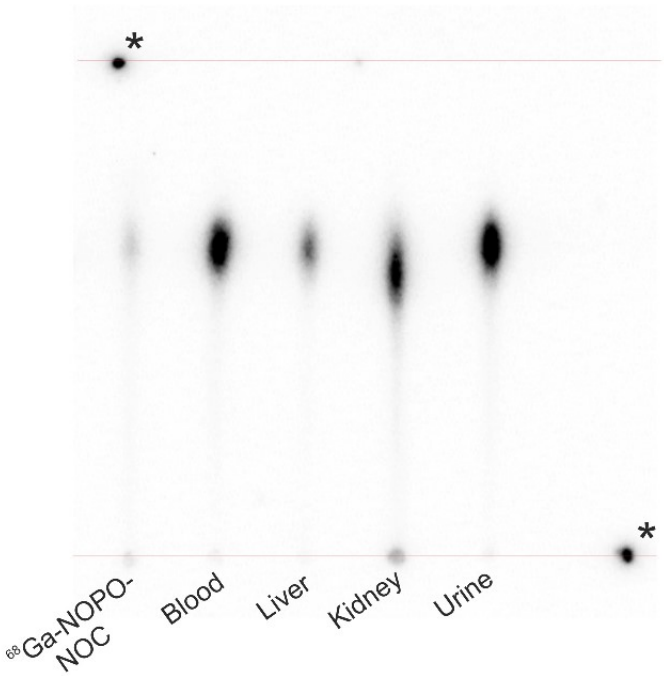

Figure S9: Example of metabolite analysis of ^{68}Ga-NOPO-NOC in mouse 4 (Table S5); 30 min p.i. in blood, liver, kidney and urine (TLC autoradiography). The asterisks marks activity spots placed for indicating start and front of the mobile phase (1M NH_4OAc/MeOH, 1:1 by volume).

9. References

1 a) A. E. Martell, R. M. Smith, Critical Stability Constants, Vols. 1–6, Plenum Press, New York, **1974**–**1989**; b) NIST Standard Reference Database 46 (Critically Selected Stability Constants of Metal Complexes), Version 7.0, **2003**; c) C. F. Baes, Jr., R. E. Mesmer, The Hydrolysis of Cations, Wiley, New York, **1976**.

Appendix C

Simecek, J.; Zemek, O.; Wester, H.; Notni, J. Ga-68-Labeling via Metal-Induced de-Esterification of NOPO-Peptides. *Journal of labelled compounds & radiopharmaceuticals* **2013**, *56*, S207–S207

Appendix C

P-120 ^{68}Ga-labeling via metal-induced de-esterification of NOPO-peptides

Šimeček, Jakub[1*]; Zemek, Ondřej[2]; Wester, Hans-Jürgen[1]; Notni, Johannes[1]

1 Pharmaceutical Radiochemistry,Technische Universität München, Garching, Germany; 2 Inorganic Chemistry, Charles University in Prague, The Czech Republic

Objectives: The recently introduced hydroxymethylphosphinic acid bifunctional chelator NOPO [1] shows unique ^{68}Ga labellabeling properties. Here we report on the consequences of the high selectivity of NOPO for ^{68}Ga even in high excess of Zn^{2+} and Fe^{3+} [2] and compare the labellabeling efficiency of peptide-conjugates of NOPO, their Zn(II) chelates and intramolecular phosphinic acid esters labeled via ^{68}Ga-induced deesterification.

Methods: NOPO-c(RGDfK) and NOPO(ester)-NOC were prepared via standard coupling methods using DIPEA, HATU and DMSO. Zn-NOPO-c(RGDfK) was prepared by mixing the conjugate with solution of $ZnCl_2$. **A**–**C** were labeled using fractionated eluates from ^{68}Ge/^{68}Ga generator with SnO_2 matrix (iThemba Labs, SA). Fully automated GMP-compliant preparation of ^{68}Ga-NOPO-peptides was done using a Gallelut^{+} module (SCINTOMICS, Germany). Chemical and radiochemical purity was assessed by HPLC and radio-TLC/HPLC, respectively.

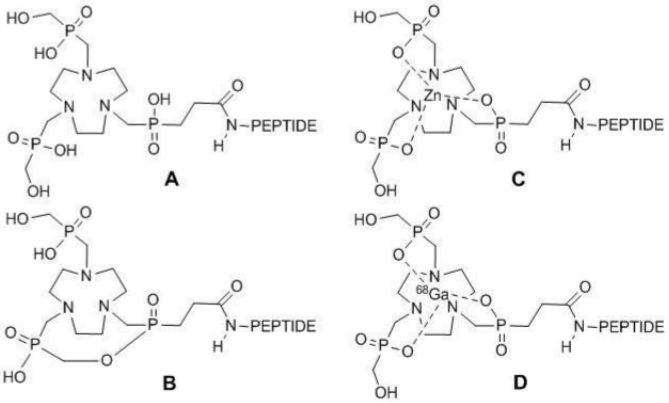

Figure 1. Generic structures of a NOPO-peptide conjugate (**A**), an intramolecular ester (**B**) thereof, a Zn(II) complex (**C**), and a ^{68}Ga-labeled NOPO-peptide (**D**).

Results: NOPO and NOPO-peptides (**A**) showed more than 50 times higher labeling efficiency for $^{68}Ga^{3+}$ compared to NODAGA-peptides. Quantitative ^{68}Ga incorporation was reached already at 30 nM concentrations (3 pmol) of NOPO-peptides. As a consequence of NOPO's high affinity to Ga^{3+}, complexes **C** underwent transmetallation with $^{68}Ga^{3+}$, resulting in **D**, even at r.t. No comparable ^{68}Ga-labellabeling was achieved with Zn(II)-NODAGA-peptides. During standard coupling reaction, intramolecular esters **B** were obtained whose structures were confirmed by multinuclear NMR and MS. Despite the primary complexation sites, i.e, the phosphinates, are partly blocked by this ester formation, presence of $^{68}Ga^{3+}$ induces de-esterification, quantitatively yielding **D** at 1 µM concentration of **B**. At the same time, presence of the ester structure in **B** protects the chelator's cavity from complexation of other cations. 1 nmol of both Zn(II)-NOPO-cyclo(RGDfK) and NOPO(ester)^{0}-NaI^{3}-octreotide could be labeled in our fully automated procedure with quantitative radiochemical yield. Interestingly, Zn(II) is not easily transchelated from NOPO-peptides in presence of other chelating agents, such as NOTA or EDTA. Although esters **B** were found to be stable under labeling conditions (pH≥ 3), they are easily cleaved at lower pH, e.g. upon addition of TFA or AcOH, yielding the corresponding NOPO-peptide **A**.

Conclusions: Efficient labeling of NOPO-esters and NOPO-Zn(II) complexes is combined with unprecedented selectivity of this chelator for $^{68}Ga^{3+}$. The reported techniques of transcomplexation and de-esterification broaden the current spectrum of labeling methods and open the field for new structures that can be considered as motifs in metal-chelate design.

Acknowledgements: Financial support by DFG (SFB 842, projects Z1/B5), is gratefully acknowledged.

References: [1] Šimeček J, et al. (2012) ChemMedChem, 7, 1375–8. [2] Šimeček J, et al. (2013) ChemMedChem, 8, 95–103.

Appendix D

Chilla, S. N. M.; Zemek, O.; Kotek, J.; Boutry, S.; Larbanoix, L.; Sclavons, C.; Elst, L. V.; Lukes, I.; Muller, R. N.; Laurent, S. Synthesis and Characterization of Monophosphinic Acid DOTA Derivative: A Smart Tool with Functionalities for Multimodal Imaging. *Bioorganic & Medicinal Chemistry* **2017**, *25* (16), 4297–4303. https://doi.org/10.1016/j.bmc.2017.06.008.

Appendix D

Bioorganic & Medicinal Chemistry 25 (2017) 4297–4303

Contents lists available at ScienceDirect

Bioorganic & Medicinal Chemistry

journal homepage: www.elsevier.com/locate/bmc

Synthesis and characterization of monophosphinic acid DOTA derivative: A smart tool with functionalities for multimodal imaging

Satya Narayana Murthy Chilla [a,*], Ondrej Zemek [b], Jan Kotek [b], Sébastien Boutry [a,c], Lionel Larbanoix [a,c], Coralie Sclavons [a,c], Luce Vander Elst [a,c], Ivan Lukes [b], Robert N. Muller [a,c], Sophie Laurent [a,c,*]

[a] Department of General, Organic and Biomedical Chemistry, NMR and Molecular Imaging Laboratory, University of Mons, Avenue Maistriau, 19, Mendeleïev Building, 7000 Mons, Belgium
[b] Department of Inorganic Chemistry, Universita Karlova, Hlavova 2030, 128 40 Prague 2, Czech Republic
[c] Centre for Microscopy and Molecular Imaging (CMMI), Rue Adrienne Bolland, 8, 6041 Charleroi-Gosselies, Belgium

ARTICLE INFO

Article history:
Received 6 February 2017
Revised 30 May 2017
Accepted 8 June 2017
Available online 15 June 2017

Keywords:
Contrast agents
Macrocyclic ligands
Peptide conjugation
Gadolinium complex
Relaxivity

ABSTRACT

A new facile synthetic strategy was developed to prepare bifunctional monophosphinic acid Ln-DOTA derivatives, Gd-DO2AGAP^{NBn} and Gd- DO2AGAP^{ABn}. The relaxivities of the Gd-complexes are enhanced compared to Gd-DOTA. Monophosphinic acid arm of these Gd-complexes affords enhancement of inner sphere water exchange rate due to its steric bulkiness. The different functionalities of DO2AGAP^{NBn} were appended in trans positions and are designed to conjugate identical or different vectors according to the potential applications. The conjugation of Gd-DO2AGAP^{ABn} with E3 peptide known to target apoptosis was successfully performed and in vivo MRI allowed cell death detection in a mouse model.

1. Introduction

Magnetic resonance imaging (MRI) is an effective tool in biomedical research for understanding biological processes in living organisms as well as in clinical diagnosis due to its excellent spatial resolution, its non-invasiveness and its limitless tissue penetration. The resolution and tissue specificity can be further enhanced by paramagnetic lanthanide complexes due to their exceptional magnetic properties.[1] Nowadays, MRI contrast agents (CA) can provide detailed information at sub-cellular level resolution.[2] In multimodal imaging a single multimodal probe could be sufficient to address the same pharmacokinetics and co-localization of the signal in each modality, allowing the correlation of the information obtained by the different methods and avoiding multiple dose injections of agents.[3] However, the sensitivity of each modality can be different by several orders of magnitude and obtaining a single molecule efficient in each imaging modality is not trivial.

Gadolinium(III) complexes of polyaminopolycarboxylates are widely used as CA in MRI.[4] The efficacy of a paramagnetic CA is assessed by its relaxivity (r_1). Relaxivity enhancement can be achieved by fast water exchange rate (usually expressed as water residence time, τ_M) and slow molecular tumbling rates characterized by the rotational correlation time τ_R.[4,5] Most of the commercially used MRI contrast agents are low-molecular-weight compounds and generally have too fast molecular tumbling, i.e. short τ_R. In general, they have also a relatively slow water exchange rate[4] (e.g. τ_M^{310} of Gd-DOTA = 122 ns, (DOTA = 1,4,7,10-tetraazacyclododecane-1,4,7,10-tetraacetic acid).[6,7] It has been reported that increasing the negative charge of the complex and bulkiness around central metal atom facilitates the fast exchange of the coordinated water molecule due to sterical reasons.[4] Extensive research about the relationship between water exchange rates and solution structures have been related to the structural isomers of lanthanide(III) DOTA complexes. It is well-known that DOTA-like ligands wrap around a lanthanide(III) ion yielding two coordination geometries, namely square antiprismatic (SA) and twisted square-antiprismatic (TSA).[4,5,8] It was observed that the TSA isomers had 10–100 times faster exchange rate of the coordinated water molecule.[9] In general, increased steric repulsion around the paramagnetic center favors the TSA isomers.[2]

In the present work, we designed a suitable ligand for different modalities, the complexes of which can exhibit favorable

* Corresponding authors at: Department of General, Organic and Biomedical Chemistry, NMR and Molecular Imaging Laboratory, University of Mons, Avenue Maistriau, 19, Mendeleïev Building, 7000 Mons, Belgium (S. Laurent).
E-mail addresses: satya.chilla@umons.ac.be (S.N.M. Chilla), modrej@natur.cuni.cz (O. Zemek), sophie.laurent@umons.ac.be (S. Laurent).

http://dx.doi.org/10.1016/j.bmc.2017.06.008
0968-0896/

characteristics for both optical imaging and MRI techniques. This system consists of a kinetically inert macrocyclic ligand covalently linked to an aromatic phosphinate moiety. Through this approach, complexes suited for magnetic and optical imaging and with identical bio distributions could be used in MRI and optical imaging techniques and should enable better interpretation of in vivo molecular imaging experiments.[10] We prepared DO2AGAP^{NBn} (Scheme 1), a DOTA derivative with two different arms: *p*-nitro benzyl phosphinic acid and pentanedioic acid arms in trans-position. Consequently, the nitro group will serve as good precursor of amine function for further conjugation of the probe. The hexapeptide E3 was previously selected as a phosphatidylserine (PS)-specific peptide using the phage-display method.[11] PS is a membrane phospholipid that is externalized by cells undergoing apoptosis, which is a natural genetically programmed cell death process occurring in several normal (e.g. embryonic development), pathologic (e.g. neurodegeneration) or therapeutic (e.g. anti-cancer treatment) conditions.[12] Apoptosis can be induced in thymus by intra-peritoneal injection of the synthetic glucocorticoid dexamethasone (DEX).[13] This cell death model was set up in mice for preliminary MRI testing of the here-presented compounds, conjugated or not to the E3 peptide.

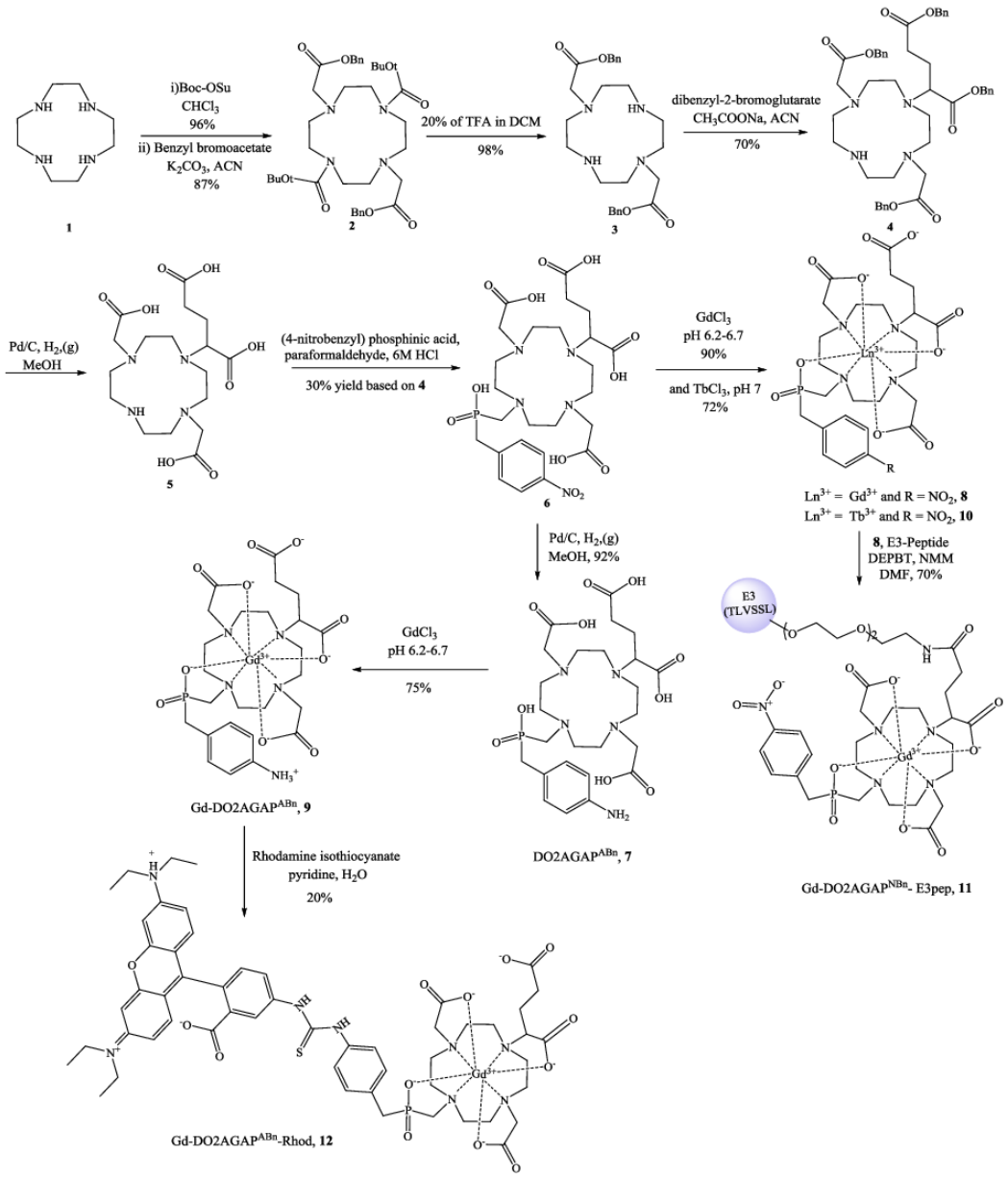

Scheme 1. Synthesis of monophosphinic acid derivatives and their conjugations with peptide and chromophore rhodamine isothiocyanate.

Appendix D

2. Results and discussion

2.1. Synthesis, complexation and conjugation of contrast agents

The controlled synthesis of ligand DO2AGAP^{NBn} **6** was obtained by a multi-step synthetic route starting from preparation of two pendant arms (Scheme 1). The key intermediates 4-nitrobenzylphosphinic acid[14] and dibenzyl 2-bromodipentanoate[15] were obtained according to literature procedures. The *trans*-DO2A **3** was synthesized by selective protection of nitrogen atoms *N-1* and *N-7* with Boc-O-succidimyl and further alkylation and deprotection as previously described.[16,17] Trialkylated product **4** was obtained by alkylating **3** with dibenzyl 2-bromopentanedioate in acetonitrile and sodium acetate used as a base. At this stage, we tried several bases for alkylation. Among them sodium acetate allowed to obtain a majority of trialkylated product even though we could not avoid the formation of minor tetraalkylated product. The second arm introduction was envisaged (after hydrogenolysis of compound **4** to intermediate **5**) by Mannich type reaction with formaldehyde and 4-nitrobenzylphosphinic acid in 6 N HCl, leading to the macrocyclic ligand **6** (DO2AGAP^{NBn}). As the secondary amine of **5** has low reactivity, a large excess of precursor and formaldehyde was used and in addition, a long reaction time was required. Ligand **6** DO2AGAP^{NBn} was isolated by ion exchange chromatography in good yields and the structure was confirmed by ^{1}H, ^{13}C, ^{31}P NMR and high-resolution mass spectrometry. Complexation of the ligand **6** DO2AGAP^{NBn} with Gd^{3+} or Tb^{3+} ions was performed under standard procedure. High-resolution mass spectrometry reveals peak corresponding to the molecular ion with the correct isotopic pattern for each complex. In order to prepare multimodal contrast agent, the conjugation efficiency of carboxylic acid of the Gd–DO2AGAP^{NBn} **8** complex was tested by using peptide-coupling reaction with a small hexapeptide under peptidic coupling methods at room temperature by using DEPBT and *N*-methyl morpholine (NMM) as a base. The compound **11** was obtained with good yield and purified by reverse phase chromatography. Our trials for conversion of nitro group of the compound **8** to amino group by catalytic hydrogenation were not successful. The ligand **6** was thus treated under hydrogenolysis to obtain **7** and Gd-DO2AGAP^{ABn} **9** was obtained after complexation in conditions similar to those used to complex **6**. Conjugation with rhodamine isothiocyanate depicted the availability of aniline group of complex **9** for further conjugations. The complex was purified by reverse phase chromatography and the corresponding mass confirms the formation of thiourea. (Scheme 1, see SI Fig. S1).

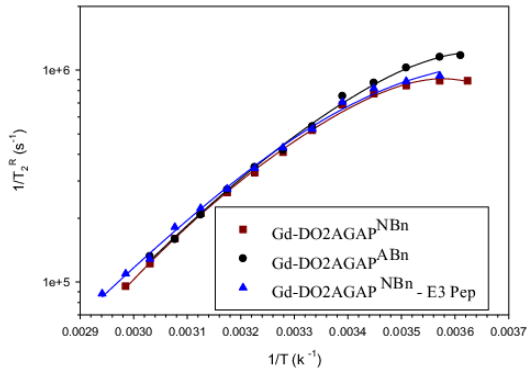

Fig. 1. Temperature dependence of the reduced transverse relaxation rate of ^{17}O at 11.75 T of Gd-DO2AGAP^{NBn} **8** (28.13 mM), Gd-DO2AGAP^{ABn} **9** (20.12 mM) and Gd-DO2AGAP^{NBn}-E3Pep **11** (26.032 mM).

2.2. Inner sphere hydration number (q) determination

A previous method for the determination of q by ^{17}O chemical shifts[18] used the dysprosium complexes, mainly because the contact contribution to its induced shift, is predominant as compared with its pseudo-contact shift and because Dy^{3+} causes a relatively small broadening of the ^{17}O signal. However, despite the quite large broadening of the ^{17}O signal induced by Gd^{3+}, this ion is better suited for such measurements since it induces only contact shift and no pseudo-contact shift. As previously reported,[19] we compared the ^{17}O chemical shift induced by the new Gd complex with well described Gd complexes, such as Gd–DOTA (Dotarem) and Gd–DTPA (Magnevist), for which $q = 1$ has been validated. The value obtained for Gd-DO2AGAP^{NBn} was estimated to be 0.74.

2.3. ^{17}O and ^{1}H NMRD measurements

The variable temperature dependence of the reduced ^{17}O transverse relaxation rates ($1/T_{2r}$) (Fig. 1) is typical of a water residence time lower than 100 ns at 310 K.[20] The observed τ_M values of Gd-DO2AGAP^{NBn} **8** and its derivatives (Table 1) show improvement compared to Gd-DOTA and to other phosphinate based DO3A complexes (Table 1).[14]

Proton relaxivity measurements in water revealed that the Gd-DO2AGAP^{NBn} **8** and its derivatives are stable in the pH range extending from 3 to 8. The magnetic field dependence of the proton longitudinal water proton relaxivities (r_1 NMRD profile) measured at 310 K shows higher relaxivities for our new complexes as compared to those of the parent compound Gd–DOTA.[20] At

Table 1
Parameters obtained from ^{17}O transverse relaxometry and ^{1}H NMRD of Gd-DO2AGAP^{NBn} **8**, Gd-DO2AGAP^{ABn} **9**, Gd-DO2AGAP^{NBn} – E3Pep **11** Gd-DO2AGAP^{ABn}-Rhod **12** and Gd-DOTA complexes in water at 37 °C.

Parameters	Gd–DO2AGAP^{NBn}[a] **8**	Gd–DO2AGAP^{ABn}[a] **9**	Gd–DO2AGAP^{NBn}–E3peptide[a] **11**	Gd-DO2AGAP^{ABn}-Rhod **12**	Gd–DOTA[a,b]
τ_M^{310} [ns]	20.3 ± 1.4	15.8 ± 0.1	10.8 ± 0.4	16[c]	122 ± 10
$\Delta H^{\neq}$ [kJ mol^{-1}]	62.6 ± 0.1	54.0 ± 0.1	44.9 ± 0.05	–	50.1 ± 0.2
$\Delta S^{\neq}$ [J mol^{-1} K^{-1}]	104.0 ± 0.3	78.5 ± 0.3	52.2 ± 0.2	–	48.7 ± 0.2
A/ħ [10^{6} rad s^{-1}]	−2.90 ± 0.02	−2.8 ± 0.1	−2.82 ± 0.02	–	−3.42 ± 0.03
B [10^{20} s^{-2}]	16.2 ± 0.4	16.5 ± 0.5	8.2 ± 0.3	–	1.94 ± 0.09
τ_v^{298} [ps]	12.1 ± 0.37	18.4 ± 0.5	13.5 ± 0.6	–	11.4 ± 0.5
E_V [kJ mol^{-1}]	20.0 ± 12.4	20.0 ± 16.0	0.1 ± 13.3	–	4.0 ± 0.4
τ_v^{310} [ps]	13.6 ± 3.0	24.2 ± 5	17.2 ± 2.7	25.2 ± 2.1	7 ± 1
τ_R^{310} [ps]	77.3 ± 3.0	90.3 ± 2.4	115.3 ± 4.0	180 ± 4	53 ± 1
τ_{so} [ps]	247 ± 22	206 ± 10	202 ± 9	162 ± 3	404 ± 24

[a] The following parameters were fixed: (D is the diffusion coefficient = 3 · 10^{-9} m^2 s^{-1}, d is the distance of closest approach = 0.36 nm, r is the distance between the proton of the inner-sphere water molecule and Gd ion = 0.31 nm, q is fixed to 1 and τ_M was fixed to the value determined by ^{17}O NMR).
[b] Ref. 21c τ_M was fixed at the value obtained for Gd-DO2AGAP^{ABn} (16 ns).

60 MHz and 310 K, the relaxivities of Gd–DO2AGAP^{NBn} **8**, Gd–DO2AGAP^{ABn} **9** and Gd–DO2AGAP^{NBn}–E3Pep **11** are enhanced respectively by 39% (r_1 = 4.93 mM^{-1} s^{-1}), 56% (r_1 = 5.45 mM^{-1} s^{-1}) and 29% (r_1 = 4.28 mM^{-1} s^{-1}) as compared to Gd–DOTA (r_1 = 3.06 mM^{-1} s^{-1}).

The NMRD profiles were fitted using the inner sphere and outer sphere theories (Fig. 2). As expected, considering the molecular weight of Gd-DO2AGAP^{NBn} **8** and its derivatives, the value of τ_R is increased as compared to that of Gd-DOTA (Table 1). In addition, the temperature dependence of the proton longitudinal relaxivity at 20 MHz of complexes **8**, **9**, **11** and **12** confirms the fast water exchange for all the complexes (see SI Fig. S1). The r_1 value of Gd-DO2AGAP^{ABn} **9** at 25 °C and 20 MHz (r_1 = 7.2 s^{-1} mM^{-1}) is larger than the value reported for Gd-DO3AP^{ABn} at 25 °C and 10 MHz (6.7 s^{-1} mM^{-1})[14] as could be expected from the larger molecular weight of **9**. In addition, the τ_M^{298} values are in the same range, 16.2 ns for Gd-DO3AP^{ABn}[14] and 38 ns for Gd-DO2AGAP^{ABn} **9**.

2.4. ^{31}P NMR measurement

The interaction of the phosphinate with the Tb^{3+} center could be confirmed by ^{31}P NMR spectroscopy (Fig. 3). For the complex Tb-DO2AGAP^{NBn} **10**, two broad shifted peaks could be observed at a range of frequencies from 400 to 500 ppm. The direction and magnitude of the shifts are in agreement with what is observed for lanthanide complexes where the phosphinate group is in close proximity to the paramagnetic center. The two peaks corresponding to two isomeric forms SAP and TSAP of **10** are observed at ~468 ppm and ~413 ppm respectively with a 4:6 ratio. The large proportion of TSAP isomer is in good agreement with the fast water exchange of the Gd complex.

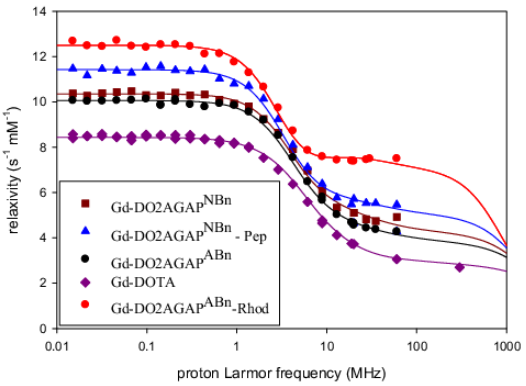

Fig. 2. ^{1}H NMRD relaxivity profiles of Gd–DO2AGAP^{NBn} **8**, Gd–DO2AGAP^{ABn} **9**, Gd–DO2AGAP^{NBn}–E3Pep **11** and Gd–DOTA in water at 37 °C.

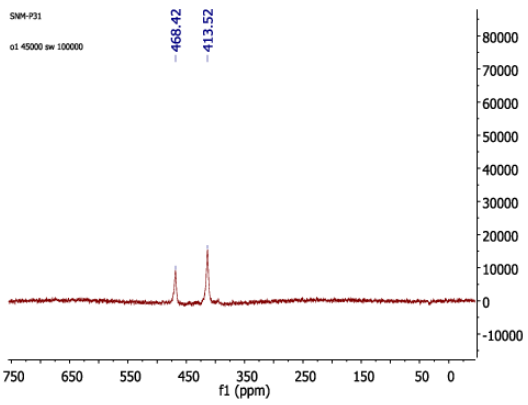

Fig. 3. ^{31}P spectrum of Tb–DO2AGAP^{NBn} **10** (D_2O).

2.5. Photophysical measurements

The emission experiments were performed in H_2O at 25 °C. After excitation of Tb-DO2AGAP^{NBn} **10** at 267 nm, no f-f transition of Tb^{3+} was observed showing no antenna effect probably because of the distance between the benzyl group and the central metal ion. In addition, the photo-physical properties of Gd-DO2AGAP^{ABn}-Rhodamine **12** was examined by recording the excitation and emission spectra of 1 mM solution in H_2O (see SI Fig. S2). For this complex a strong absorption could be observed at 556 nm and excitation at this wavelength resulted in broad emission band centered at 581 nm.

3. In vivo results

Thymus is a primary lymphoid organ in which T-lymphocytes (or T cells) develop for immune response capability. It is composed of an outer zone called cortex and an inner zone called medulla. T cell maturation (CD4+CD8+) from immature thymocytes occurs during their migration from cortex to medulla.[22] Dexamethasone (DEX) promotes thymocyte apoptosis and vessel permeability increase in the cortical region of thymus.[13,23] Immunohistochemistry of activated caspase-3 demonstrated ongoing apoptotic phenomenon in thymic cortex of mice 18 h after injection of DEX at a dose of 30 mg/kg (see SI Fig. S3). MRI showed signal intensity enhancement in thymic region corresponding to cortex in DEX-treated mice after injection of Gd-DO2AGAP^{NBn}-E3pep, suggesting specific targeting of PS on apoptotic thymocytes (see SI Fig. S3). Cortex/medulla signal intensity enhancement ratio was shown to be significantly increased ($p < 0.01$) in DEX-treated mice after injection of Gd-DO2AGAP^{NBn}-E3pep, regarding control groups (no DEX treatment + injection of Gd-DO2AGAP^{NBn}-E3pep or injection of Gd-DO2AGAP^{NBn} and DEX-treated + injection of Gd-DO2AGAP^{NBn}) (see Fig. 4 and SI Fig. S3).

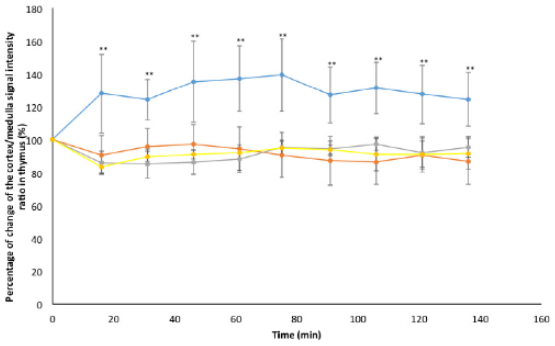

Fig. 4. Percentage of change of the cortex/medulla signal intensity ratio as a function of time after injection of Gd-DO2AGAP^{NBn}-E3pep in DEX-treated mice (n = 3, blue line), Gd-DO2AGAP^{NBn} in DEX-treated mice (n = 2, gray line), Gd-DO2AGAP^{NBn}-E3pep in untreated mice (n = 2, orange line), Gd-DO2AGAP^{NBn} in untreated mice (n = 2, yellow line). $^{**}p < 0.01$ for DEX-treated mice + Gd-DO2AGAP^{NBn}-E3pep regarding control groups.

Appendix D

4. Conclusion

In summary, a facile synthetic route was developed to prepare monophosphinic acid DOTA derivatives with two different functional groups such as carboxylic acid and nitro or amine. These new ligands DO2AGAP^{NBn} **6** and DO2AGAP^{ABn} **7** were easily complexed with lanthanides. Their relaxivities are enhanced due to the presence of phosphinic moiety that induces a τ_R increase and a significant molecular crowding which results in fast water exchange rates. The complexes were conjugated with small peptide on carboxylic acid arm or with a chromophore on amine of the phosphinate arm. Both functionalities were proved to be enough reactive to obtain multimodal contrast agent. The ^{31}P NMR of Tb–DO2AGAP^{NBn} **10** complex showed that the phosphinic acid moiety is coordinated to metal center but photophysical studies have not shown luminescence properties. In vivo experiments showed promising results in molecular MRI of cell death by conjugating PS-specific E3 hexapeptide to Gd-DO2AGAP^{NBn} **8** and targeting PS exposed by thymocytes in a mouse model of thymus cortex apoptosis induced by dexamethasone.

5. Experimental

5.1. General procedures

The chemicals were purchased from different companies: Acros, Aldrich, Fluka, Merck, Strem, Chematech, Polypeptide, TCI and VWR. All reagents were used without further purification. All solvents were distilled and/or dried prior to use by standard methodology except for those, which were reagent grades. Unless and otherwise mentioned, all the reactions were carried out under a nitrogen atmosphere and the reaction flasks were pre-dried by heat gun under vacuum. Pure water (18 MΩ cm^{-1}) was used throughout.[1,2] ^{1}H, ^{13}C and ^{31}P NMR spectra were recorded on Bruker 300 or 500 spectrometers. Chemical shift scale was referenced by following ways: ^{1}H – internal reference $CDCl_3$ at 7.27 ppm, MeOH at 3.33 ppm or D_2O at 4.75 ppm or TMS at 0.0 ppm; ^{13}C – internal reference $CDCl_3$ at 77.0 ppm, MeOH at 50 ppm or TMS at 0.0 ppm; ^{31}P – external reference 85% H_3PO_4 0.0 ppm and experiments were performed at 25 °C. ESI low-resolution mass spectra (ESI-MS) were recorded on Waters micromass ZQ system (Waters, Belgium) with full spectral detection mode in positive and negative ion modes. For HR-MS all experiments were performed on a Waters QToF 2 mass spectrometer. The analyte solutions (10^{-5} M methanol/water, 80:20) were delivered to the ESI source. Analytical thin layer chromatography (TLC) was performed on silica gel 60 F_{254} plates (E. Merck, Germany) using different mobile phases. The compounds were visualized by UV_{254} light and TLC plates were developed in Iodine chamber. The purification of the compounds was performed on KP-silica, KP-C_{18} cartridges from Biotage over Biotage flash chromatography instrument (Uppsala, Sweden) and by using silica gel 60 (70–230 mesh) from Merck. Reversed-phase analytical HPLC was performed in a stainless steel Xbridge (length 250 mm, internal diameter 4.6 mm, outside diameter 9.5 mm and particle size 5 μm) C18 column. Preparative HPLC was performed in a stainless steel Xbridge (length 250 mm, internal diameter 41.4 mm, outside diameter 50.8 mm and particle size 5 μm) C18 column (Varian). The compounds were purified using a gradient with the mobile phase starting from 95% solvent A (water) and 5% of solvent B (ACN) to 70% B in 10 min, 100% B in 18 min, 100% B isocratic till 24 min and decreased to 5% B in 28 min. The flow rate generally used for analytical HPLC was 1 mL/min and for preparative HPLC was 12 mL/min. All the solvents for HPLC were filtered through a Nylon-66 Millipore filter (0.45 μm) prior to use. Hexapeptide-E3 was synthesized on Liberty1 automated microwave peptide synthesizer with synthesis scale of 0.02–5 mmol by Fmoc chemistry. The microwave operating power was 120 V/60 Hz.

5.2. Synthetic procedures of the compounds

5.2.1. Di-tert-butyl 4-[2-(benzyloxy)-2-oxoethyl]-10-[(3-phenyl propanoyl)oxy]-1,4,7,10-tetraazacyclododecane-1,7-dicarbo-xylate (**2**)

To a solution of 1,4,7,10-tetraazacyclododecane free base **1** (714 mg, 4.067 mmol) in chloroform (35 mL), *N*-(*tert*-Butoxycarbonyloxy) succinimide (8.134 mmol) was added. The reaction mixture was stirred at room temperature for 28 h. Solvent was removed by rotary evaporation and 30 mL of NaOH 3 M was added to the remaining residue. The aqueous phase was extracted with chloroform (3.3 mL). The extracts were combined and dried (over K_2CO_3). The solvent was removed by rotary evaporation and the residue was dried in vacuum for several hours. 513 mg of the unpurified compound from the preceding reaction (1.3761 mmol) was solubilized in acetonitrile. 0.67 mL (2.87 mmol) of benzyl bromoacetate and 0.474 g (3.412 mmol) K_2CO_3 were added to this solution at room temperature, after which the mixture was heated under reflux for 8 h. The solids were discarded by filtration over Celite and the solvent was removed under *vacuum*. Chromatographic purification (alumina, 98/2 DCM/MeOH) yielded **2** as a slowly solidifying colourless oil (736 mg, 87% over all for two steps). ^{1}H NMR (500 MHz, $CDCl_3$) δ (ppm): 7.31 (m, 10H), 5.11 (s, 4H), 3.54 (s, 4H), 3.49 (m, 8H), 2.86 (m, 8H), 1.41 (s, br 18H). ^{13}C (500 MHz, $CDCl_3$) δ (ppm): 171.48, 157.11, 136.02, 79.33, 66.04, 55.04, 54.51, 46.68, 28.46. ESI-MS ($C_{36}H_{52}N_4O_8$); m/z = 668 $[M+H]^+$.

5.2.2. 2-(4,10-Bis-benzyloxycarbonylmethyl-1,4,7,10 tetraaza-cyclododec-1-yl)-pentanedioic acid dibenzyl ester (**4**)

Trifluroacetic acid (14 mL) was added to the solution of **2** (10.21 g, 0.015 mol) in dichloromethane (100 mL) and the mixture was stirred at room temperature for 16 h. The reaction mixture was evaporated under reduced pressure. Diethyl ether was used to precipitate the crude oil. The precipitate was washed with excess of ether followed by filtration and dried to obtain **3**. This product was directly used in the next step without further purification. 7.0 g (0.0149 mmol) of deprotected product and 2.64 g (0.03 mmol) of CH_3COONa were added to a solution of 5.8 g (0.015 mol) of dibenzyl 2-bromopentadioate in 100 mL of ACN and stirred for 48 h. The solid was discarded by filtration over a pad of Celite and the solvent was removed under reduced pressure to recover brownish oily crude mixture. Chromatographic purification (silica gel, 98/1.5/0.5 EtOAc/MeOH/TEA) of this mixture yielded **4** as slight yellow viscous oil. (8.1 g, 70%) ^{1}H NMR (300 MHz, $CDCl_3$) δ (ppm): 7.38–7.28 (m, 20H), 5.28–5.04 (m, 8H) 3.6–3.55 (m, 1H), 3.43 (s, br 4H), 3.1–3.0 (m, 6H), 2.6 (m, 4H), 2.52–2.5 (m, 6H), 2.22–1.97 (m, 4H). ^{13}C NMR (300 MHz, $CDCl_3$) δ (ppm): 177.75, 174.55, 172.8, 170.8, 135.73, 135.4, 128.72, 128.67, 128.59, 128.50, 128.45, 128.25, 128.17, 71.16, 67.16, 67.00, 66.54, 66.5, 59.89, 55.84, 55.21, 50.91, 49.60, 46.37, 30.59, 29.72, 26.18, 22.75, 20.52. ESI-MS ($C_{45}H_{54}N_4O_8$); m/z = 779 $[M+H]^+$.

5.2.3. 2-{4,10-Bis-carboxymethyl-7-[hydroxy-(4-nitrobenzyl) phosphinoy-lmethyl]1,4,7,10 tetraazacyclododec-1-yl}-pentanedioic acid (**6**)

10% Pd/C (1.0 g) was added to a solution of **4** (8.0 g, 0.01 mol) in MeOH (100 mL) and the resulting suspension was shaken for 4 h under H_2 atmosphere. After filtration of the suspension over a Celite pad and after evaporation of the solvent under reduced pressure, 3.2 g of **5** were obtained. The crude product (3.2 g, 8.13 mmol) was dissolved in 6 N HCl (20 mL). 1.95 g (0.065 mol) of paraformaldehyde and 6.5 g of 4-nitrobenzylphosphinic acid

Appendix D

(0.03 mol) were added to the latter solution and stirred at 50 °C for 2 days. Reaction mixture was cooled to 0 °C and all solvents were evaporated under vacuum. The product was purified using strong cation exchanger chromatography (Dowex 50, H^+-form, 6 × 25 cm, elution with water followed by 5% aq. ammonia). After evaporation of the solvents, the product was collected as a yellow oily NH_4^+-salt. The mixture was again subjected to anion exchanger (Dowex 5, Cl^- form, 15 × 3.8 cm elution with water 5% HCl). Evaporation of the solvents provided HCl salt of ligand. The chloride salt was dissolved in water, poured onto a column of a strong cation exchanger (Dowex 50, H^+-form, 4 × 25 cm) and the column was eluted with 10% aq. pyridine. After evaporation of the excess of pyridine from the eluate, the Hpy^+-salt was dissolved in a minimum amount of water and subjected to reverse phase flash chromatography, eluted with water/acetonitrile and yielded **6** (0.82 g, 30% based on **4**). ^{1}H NMR (500 MHz, D_2O) δ (ppm): 8.12–8.1 (d, J = 10 Hz, 2H), 7.43–7.41 (d, J = 10 Hz, 2H), 3.75–3.64 (m, 5H), 3.48–2.85 (m, 20H), 2.63–2.61 (m, 2H), 1.96 (s br, 2H). ^{13}C NMR (500 MHz, D_2O) δ (ppm): 177.3, 174.9, 173.5, 173.2, 146.5, 138.9, 131.1, 130.0, 122.1, 122.0, 66.5, 58.9, 58.2, 54.6, 54.1, 52.7, 52.4, 52.3, 51.1, 50.5, 41.2, 31.3, 30.2, 25.2. ^{31}P (500 MHz, D_2O) δ (ppm): 38.22 (S). HRMS (ESI): calcd for $C_{25}H_{38}N_5O_{12}P$; $[M+H]^+$ 632.2333; found 632.2334.

5.2.4. 2-{7-[(4-Aminobenzyl)hydroxyphosphinoylmethyl]-4,10-bis-carboxymethyl-1,4,7,10 tetraaza-cyclododec-1-yl}-pentanedioic acid (*7*)

10% Pd/C (0.1 g) was added to a solution of **6** (0.15 g, 0.23 mmol) in EtOH (10 mL) and the resulting suspension was shaken for 4 h under H_2 atmosphere. The suspension was filtered over a celite pad, and after evaporation of the solvent under reduced pressure **7** was obtained (0.13 g, 92%). ^{1}H NMR (500 MHz, D_2O) δ (ppm): 6.82–6.8 (d, J = 10 Hz, 2H), 6.33–6.3 (d, J = 10 Hz, 2H), 3.75–3.64 (m, 5H), 3.4–2.80 (m, 20H), 2.65–2.61 (m, 2H), 1.96 (s br, 2H). ^{13}C NMR (500 MHz, D_2O) δ (ppm): 177.3, 174.9, 173.5, 173.2, 145.5, 138.9, 138.3, 129.1, 116.1, 122.0, 66.5, 58.9, 58.2, 54.6, 54.1, 52.7, 52.4, 52.3, 51.1, 50.5, 41.2, 31.3, 30.2, 25.2. ^{31}P (500 MHz, D_2O) δ (ppm): 37.22 (s). ESI-MS ($C_{25}H_{40}N_5O_{10}P$); m/z = 602.6 $[M+H]^+$

5.3. Preparation of Gd^{3+} complex of DO2AGAP^{NBn} (*8*)

The complex was obtained by adding portion wise $GdCl_3{\cdot}6H_2O$ to a solution of **6** (0.26 g, 0.69 mmol) in H_2O (5 mL), maintaining the pH between 6.2 and 6.7 by addition of 1 N Pyridine. The final pH of the solution after stirring 24 h was 6.3. The excess of the free lanthanide was removed as $Gd(OH)_3$ precipitate, which appeared at pH 9. The resulting solution was treated with chelex-100 to remove free Gd^{3+} ions. The absence of free Gd^{3+} ions was confirmed by an Arsenazo III test[24] (in 0.1 M NaAc/HAc buffer solution, pH 5.2). The pH of the supernatant was decreased to 7 and the solution was freeze-dried. The complex was dissolved in water, purified by reverse phase flash chromatography and freeze-dried, yielding Gd–DO2AGAP^{NBn} (**8**) as a white powder (450 mg, 90%). The compound was purified by preparative HPLC as mentioned above. HPLC: R_t = 9.5 min, purity (215 nm): 96% HRMS (ESI): calcd for $C_{25}H_{34}GdN_5O_{12}P$; $[M+Na]^+$ 805.1126; found 805.1090.

5.4. Preparation of Gd^{3+} complex of DO2AGAP^{ABn} (*9*)

Gadolinium(III) complex of DO2AGAP^{ABn} was prepared by mixing a 1:1.1 M ratio of $GdCl_3{\cdot}6H_2O$ (0.054 g, 0.14 mmol) and ligand **7** (0.08 g 0.13 mmol) in water followed by addition of 1 N pyridine to adjust the pH to 7. The reaction mixture was briefly heated to 50 °C and then stirred at room temperature overnight. The complex was purified on Amberlite CG-50 with water elution. The solution was tested negatively for the presence of free lanthanide(III) ions by using arsenazo III test as an indicator (in 0.1 M NaAc/HAc buffer solution, pH 5.2). The complex was dissolved in water, purified by reverse phase flash chromatography and freeze-dried, yielding **Gd–DO2AGAP^{ABn}** as a pale off white powder (80 mg, 75%). The concentration of gadolinium(III) ions in solution was determined by relaxometric measurement. HRMS (ESI): calcd for $C_{25}H_{37}GdN_5O_{10}P$; $[M+Na]^+$ 775.1530; found 775.1534.

5.5. Preparation of Tb^{3+} complex of DO2AGAP^{NBn} (*10*)

Terbium(III) complex of DO2AGAP^{NBn} was prepared by mixing a 1:1.1 M ratio of $TbCl_3{\cdot}6H_2O$ (14.2 mg, 0.004 mmol) and ligand **6** (0.022 g, 0.004 mmol) in water followed by addition of 1 N pyridine to adjust the pH to 7. The reaction mixture was briefly heated to 50 °C and then stirred at room temperature overnight. The complex was purified on Amberlite CG-50 with water elution. The solution was tested for the absence of free lanthanide(III) ions by using arsenazo III test as an indicator (in 0.1 M NaAc/HAc buffer solution, pH 5.2). The complex was dissolved in water, purified by reverse phase flash chromatography and freeze-dried, yielding **Tb–DO2AGAP^{NBn}** as an off-white powder (20 mg, 72%). ESI-MS ($C_{25}H_{33}TbN_5O_{12}P2Na$); m/z = 832.2

5.6. Conjugation of peptide (E3) with Gd–DO2AGAP^{NBn} (*11*)

0.2 g (0.25 mmol) of **8** was dissolved in 5 mL of DMF to which 0.21 g (0.28 mmol) of peptide-E3, 89 mg (0.32 mmol) of DEPBT and 0.1 mL (0.752 mmol) of DIPEA were added. The reaction mixture was stirred for 4 h and diluted with 20 mL of water; a white precipitate was isolated by filtration and washed with ethyl acetate (50 mL). The solid was dried under reduced pressure and purified by semi-preparative HPLC using method A and obtained after 16 min of retention time. The compound was freeze-dried, and **11** was obtained as a white solid (0.27 g, 70%). HRMS (ESI): calcd for $C_{58}H_{93}GdN_{12}O_{24}P$; $[M+H]^+$ 1528.5398; found 1528.5422.

5.7. Conjugation of rhodamine with Gd-DO2AGAP^{ABn} (*12*)

32 mg of rhodamine isothiocyanate (0.072 mmol) and 6 μl of pyridine (0.07 mmol) were added to the aqueous solution of complex **9** (45 mg, 0.06 mmol) at room temperature. The mixture was stirred in the dark for 48 h. The mixture was freeze-dried and subjected to purification by reverse phase flash-chromatography over C18 silica gel using conditions as mentioned previously and **12** was obtained after 10 min of elution. (17 mg, 20%). ESI-MS ($C_{54}H_{65}GdN_8O_{13}PS$); m/z = 1274 $[M+Na]^+$.

5.8. ^{17}O NMR measurements and proton NMRD profiles

^{17}O NMR measurements were performed at 11.75 T on 350 μL samples contained in 5 mm o.d. tubes on a Bruker Avance 500 spectrometer (Karlsruhe, Germany). Temperature was regulated by air or nitrogen flow controlled by a Bruker BVT 3200 unit. ^{17}O transverse relaxation times of distilled water (pH 6.5–7) were measured using a CPMG sequence and a subsequent two-parameter fit of the data points. The 90° and 180° pulse lengths were 27.5 and 55 μs, respectively. The ^{17}O T_2 of water in complex solution was obtained from the line width measurements or CPMG sequence when linewidth was <80 Hz. All spectra were proton decoupled. The data are presented as the reduced transverse relaxation rate $\{1/T_2^r = 55.55/([\text{Gd-complex}]\times q \times T_2^p)$, where: [Gd complex] is the molar concentration of the complex, q is the number of coordinated water molecules and T_2^p is the paramagnetic transverse relaxation rate}. The fitting of the experimental data was performed as described in literature.[20,21] The gadolinium

Appendix D

concentration was determined by ICP-AES on a JobinYvon JY 70 instrument (Longjumeau, France) and was further confirmed by ^{1}H relaxometry of a decomplexed sample. Proton nuclear magnetic relaxation dispersion (NMRD) profiles were measured on a Stelar Spinmaster FFC (Mede, Italy) fast field cycling NMR relaxometer over a magnetic field range from 0.24 mT to 1.0 T. Measurements were performed on 0.6 mL samples contained in 10 mm o.d. Pyrex tubes. Additional relaxation rates at 20 and 60 MHz were obtained on a Minispec mq20 and a Minispec mq60, respectively.

5.9. In vivo MRI and image analysis

Animal experiments were performed under approval of the ethics committee of the Center for Microscopy and Molecular Imaging (CMMI protocol number 2012-06; LA1500589). Apoptosis was induced in thymus of 4–6 weeks old CD-1 female mice (Charles River (L'Arbresle, France)) by intraperitoneal injection of 30 mg/kg freshly prepared water-soluble dexamethasone (DEX, Sigma-Aldrich, Belgium, 25 mg/ml in PBS [Phosphate buffered saline] solution). For MRI observations, mice were anesthetized with isoflurane vaporized at 2–2.5% in O_2 à 2 L/min and placed in a warmed bed into the MRI scanner. Mice respiration was monitored during all experiment and anesthesia was adapted to 1.5–2% of isoflurane with O_2 flow of 0.4 L/min to maintain 20 respirations per minute. MRI was performed 16–18 h after dexamethasone injection, on a Bruker Biospec 9.4 T (Bruker, Karlsruhe, Germany). MR signal was detected using a volume coil (40 mm diameter) adapted for mouse body and connected to the animal bed. Images were acquired and visualized with the Paravision software (Bruker). The sequence used for this study was a T_1 spin-echo sequence (RARE): TR : 389.1 ms; TE: 8.9 ms; NEX (number of averages): 16; acquisition time: 14 min 56 s; matrix: 344 × 192; slice thickness: 1 mm; FOV: 3.2 × 1.8 cm; spatial resolution: 93 × 94 μm; fat saturation. Images were acquired on mice, treated with dexamethasone (developing apoptosis in the cortical region of thymus) and on control mice, up to 2 h (9 time points) after receiving an intravenous injection of Gd-DO2AGAP^{NBn}-E3pep or Gd-DO2AGAP^{NBn} (200 Â μmol Gd/kg). Image analysis was performed with the ImageJ software by measurement of a signal intensity enhancement ratio in thymus (cortex versus medulla), expressed as a percentage of change relative to the pre-contrast situation (considered as 100%). Statistical significance of differences between percentages of change were tested in Microsoft Excel using Student's *t*-test.

5.10. Immunohistochemistry

Mice were sacrificed in accordance with the ethics committee of CMMI (protocol 2012-06), 18 h after intraperitoneal injection of DEX (30 mg/kg). Thymus was collected and fixed in 4% formalin during 24 h. After PBS washing, tissue was dehydrated and embedded in paraffin using a Tissue-Tek VIP machine (Sakura Finetek, Japan). Thymus sections of 5-μm thickness were cut using a microtome and were automatically processed by a Discovery XT machine (Ventana/Roche, Belgium) for immunohistochemistry of activated (cleaved) caspase-3 enzyme. Sections were incubated at 37 °C for 1 h with anti-cleaved caspase-3 (Asp175) primary antibody (#9661, Cell Signaling, Netherlands), at dilution 1:100 in Ventana/Roche buffer, and for 24 min with secondary antibody (1:200; biotinylated anti-rabbit IgG made in goat (#BA-1000, Vector laboratories, LabConsult, Belgium)). Areas of caspase-3 activation were revealed by a streptavidin-biotin peroxidase detection system (Discovery DAB Map (#760-124, Ventana/Roche, Belgique)) allowing for diaminobenzidine precipitation at locations of antibody binding (brownish coloration) on thymic tissue. After nuclei coloration with hematoxylin, sections were dehydrated and mounted for light microscope observation.

Acknowledgements

The authors thank to the ARC Programs of the French Community of Belgium, UIAP VII program of Belspo, the Région Wallone (Gadolymph project n° 1317980 through the EuroNanoMed 2013 framework), Holocancer and Interreg programs. The support and sponsorship concerted by COST Actions TD1004 and EMIL program are acknowledged. The support from the Grant Agency of the Czech Republic (Project No. 16-03156S) is acknowledged. The authors thank the Center for Microscopy and Molecular Imaging (CMMI, supported by the Wallonia Region). The DIAPATH (Digital Image Analysis in Pathology) research unit of CMMI is thanked for immunohistochemical tissue processing.

A. Supplementary data

Supplementary data associated with this article can be found, in the online version, at http://dx.doi.org/10.1016/j.bmc.2017.06.008.

References

1. Merbach A, Helm L, Toth E. *The Chemistry of Contrast Agents in Medical Resonance Imaging*. 2nd ed. John Wiley & Sons Ltd; 2013.
2. (a) Webb AG. *J Magn Reson*. 2013;226:55–66;
(b) Di Corato R, Gazeau F, Le Visage C, et al. *ACS Nano*. 2013;9:7500–7512.
3. Frullano L, Meade T. *J Biol Inorg Chem*. 2007;12:939–949.
4. (a) Que EL, Chang CJ. *Chem Soc Rev*. 2010;39:51–60;
(b) Caravan P. *Chem Soc Rev*. 2006;35:512–523;
(c) Hermann P, Kotek J, Kubicek V, Lukes I. *Dalton Trans*. 2008;3027–3047.
5. (a) Tóth É, Pubanz D, Vauthey S, Helm L, Merbach AE. *Chem Eur J*. 1996;2:1607–1615;
(b) Caravan P, Ellison JJ, McMurry TJ, Lauffer RB. *Chem Rev*. 1999;99:2293–2352.
6. Powell DH, Dhubhghaill OMN, Pubanz D, et al. *J Am Chem Soc*. 1996;39:9333–9346.
7. Chilla SNM, Laurent S, Vander Elst L, Muller RN. *Tetrahedron*. 2014;70:5450–5454.
8. Aime S, Botta M, Fasano M, et al. *Inorg Chem*. 1997;36:2059–2068.
9. (a) Dunand FA, Aime S, Merbach AE. *J Am Chem Soc*. 2000;122:1506–1512;
(b) Woods M, Aime S, Botta M, et al. *J Am Chem Soc*. 2000;122:9781–9792;
(c) Woods M, Kovacs Z, Zhang S, Sherry AD. *Angew Chem Int Ed*. 2003;42:5889–5892.
10. Bonnet CS, Toth E. *C R Chim*. 2010;13:700–714.
11. Laumonier C, Segers J, Laurent S, et al. *J Biomol Screen*. 2006;11:537–545.
12. Elmore S. *Toxicol Pathol*. 2007;35:495–516.
13. (a) Brooks KJ, Bunce KT, Haase MV, et al. *Steroids*. 2005;70:267–272;
(b) Herold MJ, McPherson KG, Reichardt HM. *Cell Mol Life Sci*. 2006;63:60–72.
14. (a) Rudovsky J, Cigler P, Kotek J, et al. *Chem Eur J*. 2005;11:2373–2384;
(b) Rudovsky J, Kotek J, Hermann P, Lukes I, Mainero V, Aime S. *Org Biomol Chem*. 2005;3:112–117.
15. (a) Wardleworth PS, Baylis EK. EP 307362; 1989.;
(b) Dingwall JG, Ehrenfreund J, Hall RG. *Tetrahedron*. 1989;45:3787–3808.
16. Izatt RM, Pawlak K, Bradshaw JS, Bruening RL. *Chem Rev*. 1991;91:1721–2085;
(b) Burai L, Ren J, Kovacs Z, Brucher E, Sherry AD. *Inorg Chem*. 1998;37:69–75.
17. (a) Lowe MP, Parker D, Reany O, et al. *J Am Chem Soc*. 2001;123:7601–7609;
(b) Eisenwiener K-P, Powell P, Macke HR. *Bioorg Med Chem Lett*. 2000;10:2133–2135;
(c) Huskens J, Sherry AD, Torres DA, Kovacs Z, Andre JP, Geraldes CFGC. *Inorg Chem*. 1997;36:1495–1503.
18. Alpoim CM, Urbano AM, Geraldes CFGC, Peters JA. *J Chem Soc Dalton Trans*. 1992;463–467.
19. (a) Laurent S, Vander Elst L, Wautier M, Galaup C, Muller RN, Picard C. *Bioorg Med Chem Lett*. 2007;14:6230–6233;
(b) Granato L, Laurent S, Vander Elst L, Djanashvili K, Peters JA, Muller RN. *Contrast Media Mol Imaging*. 2011;6:482–491.
20. Vander Elst L, Maton F, Laurent S, Seghi F, Chapelle F, Muller RN. *Magn Reson Med*. 1997;38:604–614.
21. Laurent S, Vander Elst L, Muller RN. *Contrast Med Mol Imaging*. 2006;3:128–137.
22. Li L, Hsu HC, Grizzle WE, et al. *Immunology*. 2003;57:410–422.
23. Bubanovic IV. *Med Hypotheses*. 2003;60:315–320.
24. Rohwer H, Hoston E. *Anal Chim Acta*. 1997;3:271–277.

Electronic supplementary data for

Synthesis and characterization of mono phosphinic acid DOTA derivatives: A smart tool with functionalities for multimodal imaging

Satya Narayana Murthy chilla[a,] ∗ Ondrej Zemek,[b] Jan Kotek,[b] Sébastien Boutry[a,c], Lionel Larbanoix[a,c], Coralie Sclavons[a,c] Luce Vander Elst,[a,c] Ivan Lukes,[b] Robert N. Muller, [a,c] and Sophie Laurent [a,c] ∗

a) *Department of General, Organic and Biomedical Chemistry, NMR and Molecular Imaging Laboratory, University of Mons, Avenue Maistriau, 19, Mendeleïev Building, 7000 Mons, Belgium.*
b) *Department of Inorganic Chemistry, Charles University, Hlavova 2030, 12840, Prague 2, Czech Republic.*
c) *Centre for Microscopy and Molecular Imaging (CMMI), Rue Adrienne Bolland, 8, 6041, Charleroi-Gosselies.*

Table of contents

∗ Corresponding author. Tel.: +32-65373516; fax: +32-65373484; e-mail: satya.chilla@umons.ac.be

∗ Corresponding author. Tel.: +32-65373525; fax: +32-65373484; e-mail: sophie.laurent@ umons.ac.be

Appendix D

Relaxivity vs Temperature for Gd–DO2AGAP^{NBn} 8, Gd–DO2AGAP^{ABn} 9, Gd–DO2AGAP^{NBn}–E3Pep 11 and Gd–DO2AGAP^{ABn}-Rhod 12 complexes:

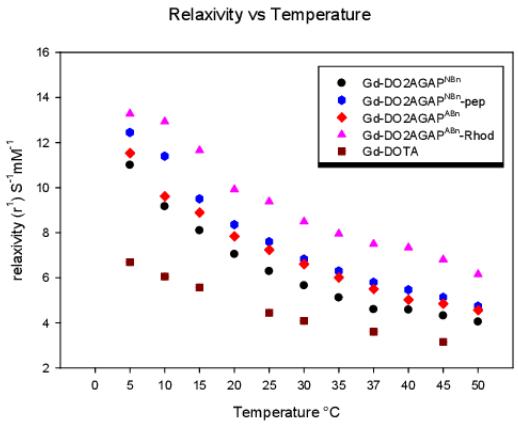

Figure S1: Relaxivity vs Temperature for Gd–DO2AGAP^{NBn} 8, Gd–DO2AGAP^{ABn} 9, Gd DO2AGAP^{NBn}–E3Pep 11 and Gd–DO2AGAP^{ABn}-Rhod 12 complexes and Gd-DOTA

Emission spectrum:

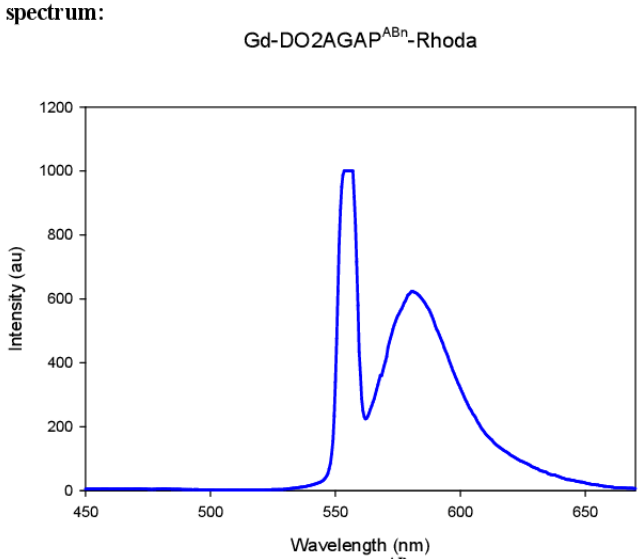

Figure S2: Emission spectrum of Gd-DO2AGAP^{ABn}-Rhodamine 12 (H_2O, pH 7.1) (λ_{exc} = 556nm and λ_{em} = 580nm)

Immunohistochemistry:

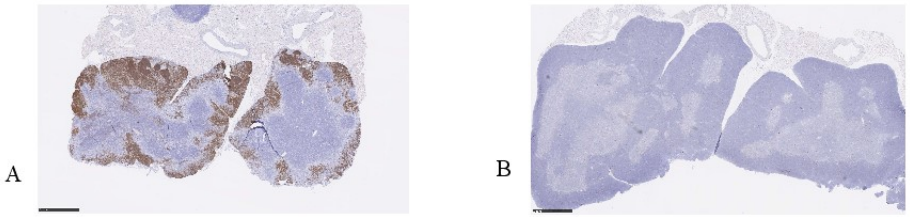

Immunohistochemistry of cleaved caspase-3 in thymus 18h post-DEX treatment (30 mg/kg)

Immunohistochemistry of cleaved caspase-3 in control thymus

MRI:

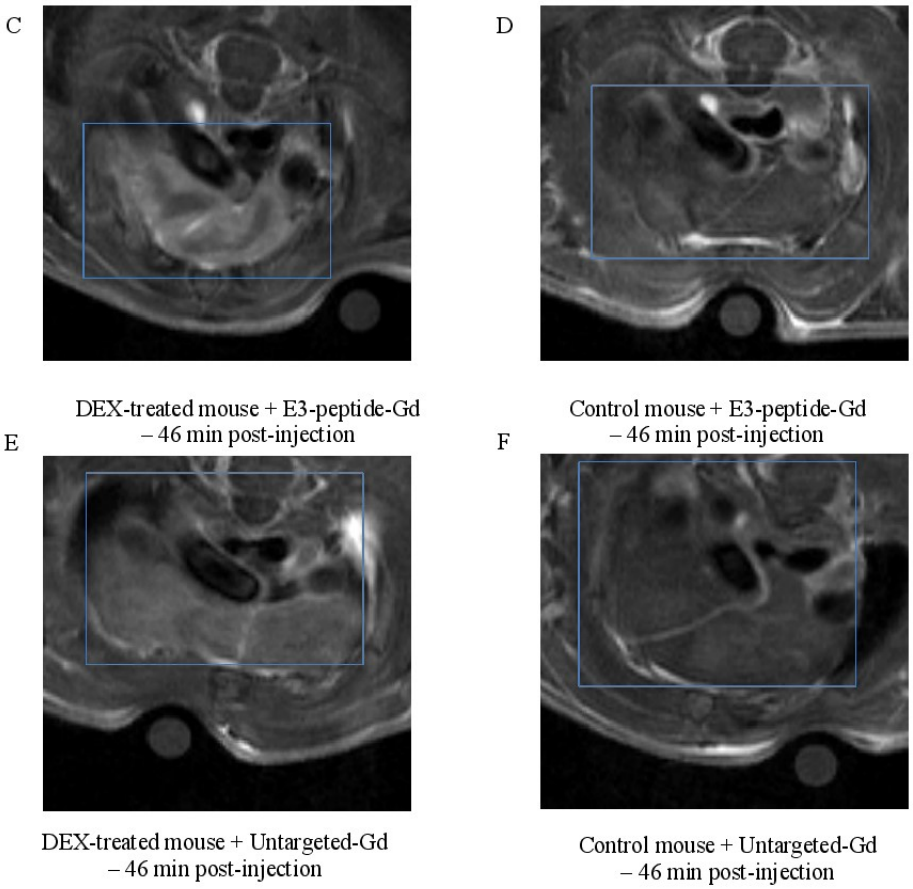

Figure S3: Immunohistochemistry of caspase-3 activation in thymus (cortex) of 18h DEX-treated (A) and untreated (B) mouse (Bar=1 mm). MR images showing surrounded thymus (blue square) 46 minutes after injection (200 micromoles Gd/kg) of: Gd-DO2AGAP^{NBn}-E3pep in DEX-treated mouse (C); Gd-DO2AGAP^{NBn}-E3pep in untreated mouse (D); Gd-DO2AGAP^{NBn} in DEX-treated mouse (E); Gd-DO2AGAP^{NBn} in untreated mouse (F). Similarity between locations of apoptosis detection in immunohistochemistry of cleaved caspase-3 (A) and in MRI with PS-targeted Gd-based compound (C) can be noted.

Appendix D

a) NMR spectrum of ligand 6 (DO2AGAP^{NBn})

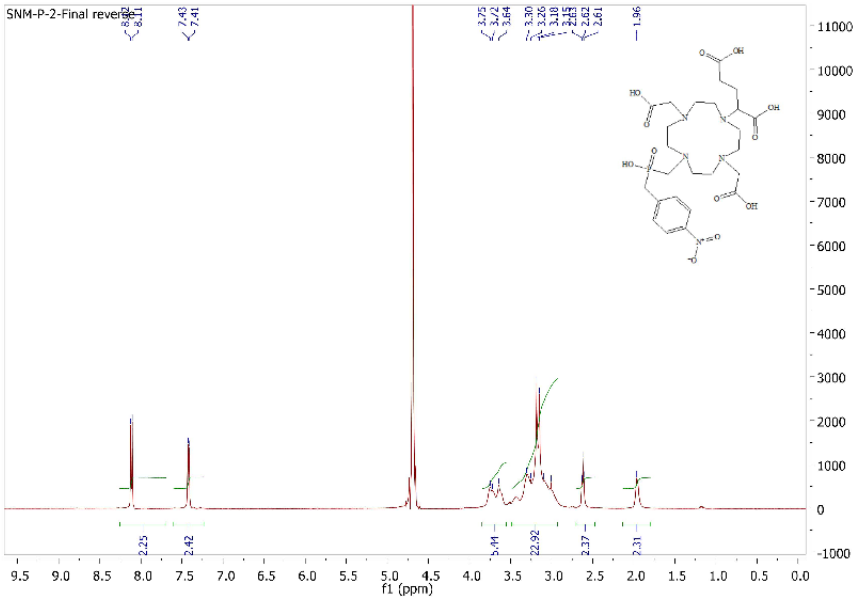

b) HRMS spectrum of the compound 6 (DO2AGAP^{NBn})

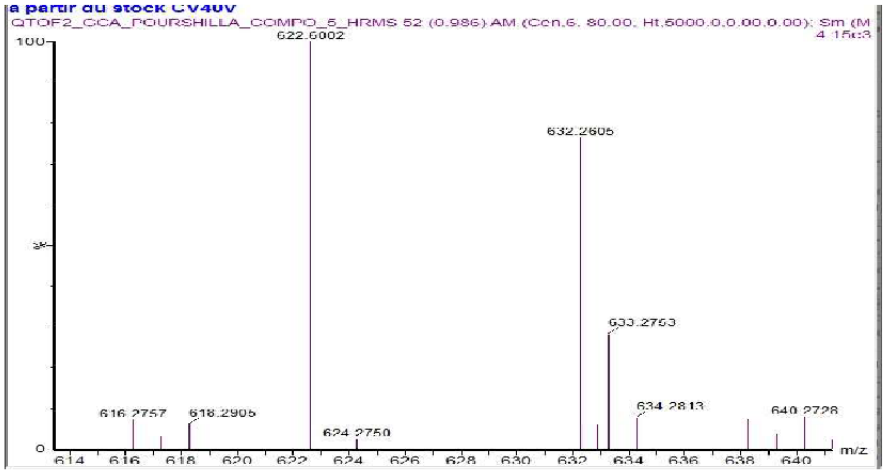

Figure S4: ^{1}H NMR (a) and HR-MS (b) spectra of the compound 6 (DO2AGAP^{NBn})

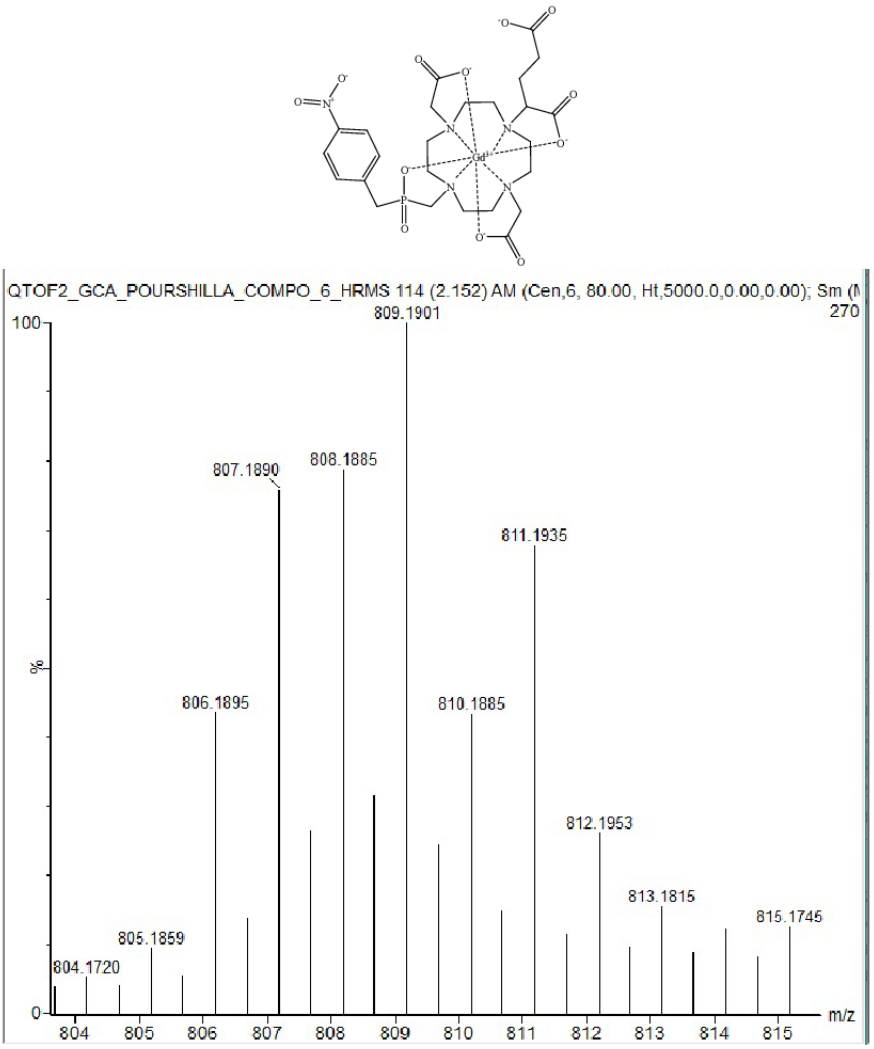

Figure S5: HR-MS spectrum of Gd–DO2AGAP^{NBn} 9

Appendix D

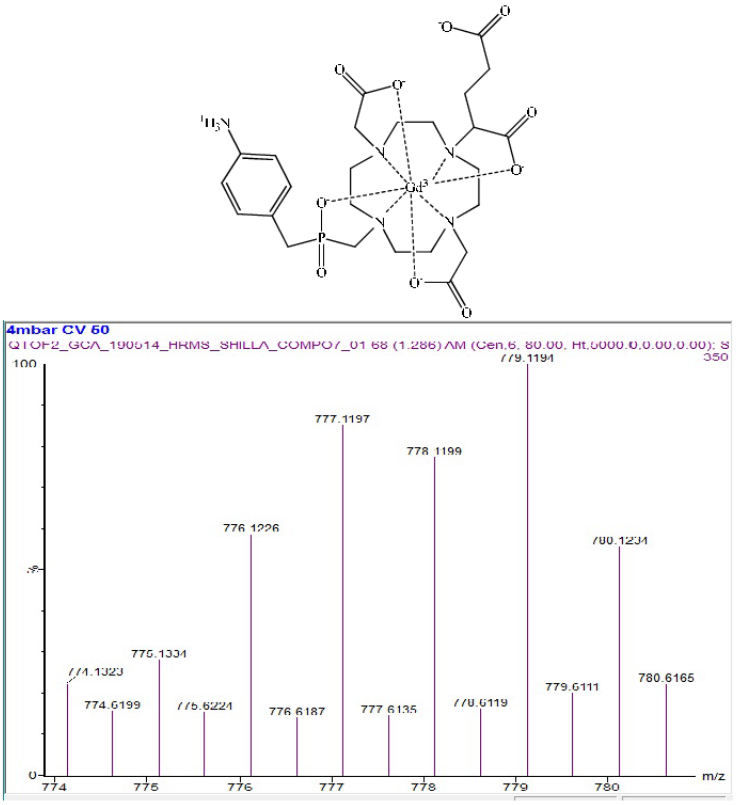

Figure S6: HR-MS spectrum Gd–DO2AGAP^{ABn} 9

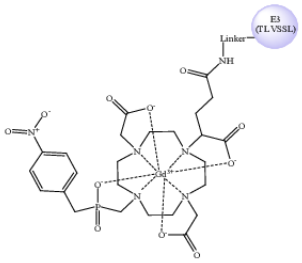

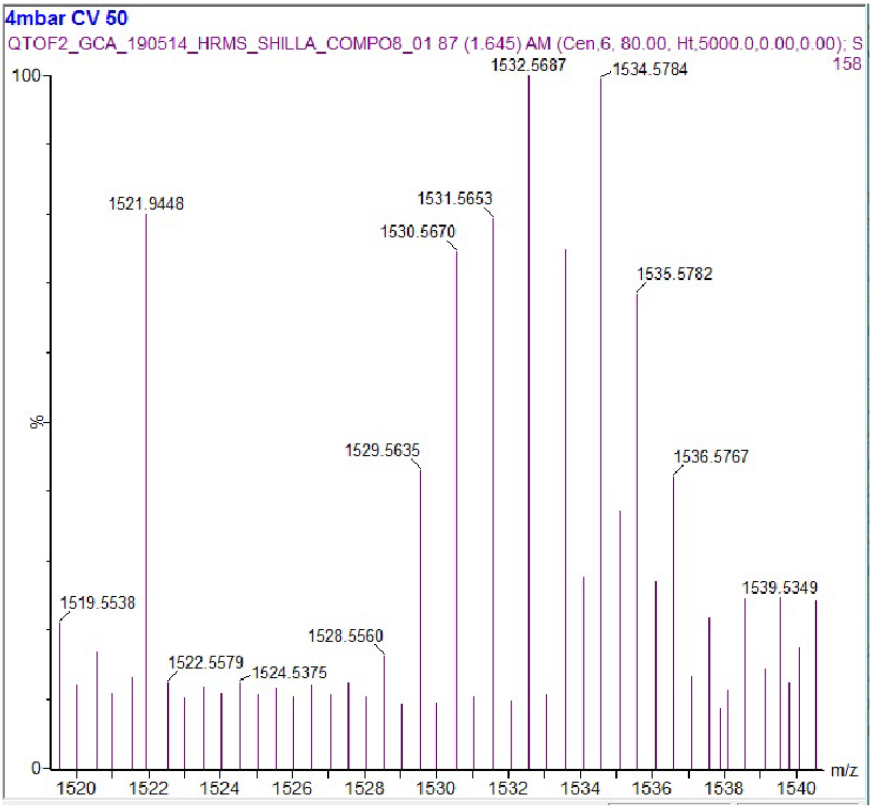

Figure S7:HR-MS spectrum Gd–DO2AGAP^{NBn} -E3 11

Appendix E

Rendler, T.; Neburkova, J.; Zemek, O.; Kotek, J.; Zappe, A.; Chu, Z.; Cigler, P.; Wrachtrup, J. Optical Imaging of Localized Chemical Events Using Programmable Diamond Quantum Nanosensors. *Nat Commun* **2017**, *8* (1), 14701. https://doi.org/10.1038/ncomms14701.

Appendix E

nature COMMUNICATIONS

ARTICLE

Received 19 Jul 2016 | Accepted 23 Jan 2017 | Published 20 Mar 2017

DOI: 10.1038/ncomms14701 OPEN

Optical imaging of localized chemical events using programmable diamond quantum nanosensors

Torsten Rendler[1,*], Jitka Neburkova[2,3,*], Ondrej Zemek[4], Jan Kotek[4], Andrea Zappe[1], Zhiqin Chu[1], Petr Cigler[2] & Jörg Wrachtrup[1]

Development of multifunctional nanoscale sensors working under physiological conditions enables monitoring of intracellular processes that are important for various biological and medical applications. By attaching paramagnetic gadolinium complexes to nanodiamonds (NDs) with nitrogen-vacancy (NV) centres through surface engineering, we developed a hybrid nanoscale sensor that can be adjusted to directly monitor physiological species through a proposed sensing scheme based on NV spin relaxometry. We adopt a single-step method to measure spin relaxation rates enabling time-dependent measurements on changes in pH or redox potential at a submicrometre-length scale in a microfluidic channel that mimics cellular environments. Our experimental data are reproduced by numerical simulations of the NV spin interaction with gadolinium complexes covering the NDs. Considering the versatile engineering options provided by polymer chemistry, the underlying mechanism can be expanded to detect a variety of physiologically relevant species and variables.

[1] 3. Physikalisches Institut, Universität Stuttgart, Pfaffenwaldring 57, 70569 Stuttgart, Germany. [2] Institute of Organic Chemistry and Biochemistry of the CAS, Flemingovo nam. 2, 166 10 Prague 6, Czech Republic. [3] First Faculty of Medicine, Charles University, Katerinska 32, 121 08 Prague 2, Czech Republic. [4] Faculty of Science, Department of Inorganic Chemistry, Charles University, Hlavova 2030, 128 43, Prague 2, Czech Republic. * These authors contributed equally to this work. Correspondence and requests for materials should be addressed to Z.Q.C. (email: z.chu@physik.uni-stuttgart.de) or to P.C. (email: cigler@uochb.cas.cz).

Physiological processes inside a living cell are accompanied by transient changes in variables including concentrations of ions[1], reactive oxygen species[2], enzymes[3], nucleic acids[4], pH[5] and redox potential[6]. Although a vast range of sensing principles for these variables based on selective molecular and nanoparticle probes have been developed[7–9], the field is still limited by the chemical and optical stabilities of probes, probe toxicity and perturbation of the biological environment, and, above all, probe sensitivity and spatiotemporal resolution. Therefore, reliable intracellular sensors designed for non-invasive quantitative monitoring of physiologically relevant species with near-atomic resolution are urgently needed to elucidate critical underlying mechanisms in cell biology and physiology, which in turn may lead to new possibilities for diagnostics and therapeutics at the subcellular level.

Nanodiamonds (NDs; nanometre-sized diamond particles) with nitrogen-vacancy (NV) defect centres exhibit excellent biocompatibility[10–12], long-term stability[13,14] and unique quantum sensing capability by optical means[15–17]. These NDs hold great promise for a range of biomedical applications, including serving as nanomedicine platforms for delivery of drugs[18], genes and proteins[19,20], use as fluorescent/photoacoustic imaging agents[13,21,22] and applications in multifunctional intracellular sensing[23–25]. The fluorescence of these atomic-scale NV centres in NDs depends on their electronic spin states, which show a long coherence time even under ambient conditions, enabling direct nanoscale sensing for magnetic/electric field[15,26], temperature[24,27,28] and mechanical force/pressure[29,30]. In fact, the facile optical readout of NV centres in NDs facilitates quantum sensing in living cells[23,24]. However, direct measurement of chemical reactions and processes through quantum detection of NDs remains challenging, especially under physiological conditions. The main challenges lie in developing selective detection principles enabling direct quantum sensing of chemical transformations via spin-dependent fluorescence of NV centres, the related chemical architectures on the ND surface that host the primary sensing system and robust quantum-sensing schemes applied to NV centres in NDs, especially when they are introduced to complicated environments such as the interior of living cells.

A critical step towards developing NDs with biomedical applications is customizing the diamond surface chemistry for required functionalization, while maintaining excellent colloidal stability under physiological conditions[31]. NDs engineered with our recently developed polymer-coating approach[32,33] exhibit long-term colloidal stability, reduced nonspecific binding and the capability for convenient chemical modification. In the current study, we connected macrocyclic complexes of Gd^{3+} ions with a biocompatible copolymer shell on NDs via selectively cleavable linkers. In this sense, the attachment of Gd^{3+} complexes to the polymer is strictly programmed, paving the way for their subsequent detachment in response to changes in a sole parameter. By quantifying the change in NV spin relaxation time due to the Gd^{3+} complexes (spin noise), we show that this platform can be chemically programmed to sense fundamental physiological quantities. We designed and demonstrated time dependent pH and redox potential detection in a microfluidic device with sub-micrometre spatial resolution and minute temporal resolution. In particular, the excellent agreement between our experimental data and theoretical modelling suggests that this scheme can serve as a multifunctional platform for sensing of various chemical and biochemical transformations under physiological conditions with high selectivity (enabled by available libraries of selective cleavage reactions) and unprecedented sensitivity and resolution (yielded by the quantum detection approach).

Results

Design of ND-polymer-Gd multifunctional nanosensors. To enable direct selective quantum detection of chemical processes by means of NV centres, we designed a general nanosensing platform that combines NV centres in NDs and surface polymer coating bearing spin labels. Specifically, complexes of Gd^{3+} ions with electronic spin $S = 7/2$ were chemically attached via selectively cleavable linkers to poly[(2-hydroxypropyl)methacrylamide]-based (HPMA) co-polymer chains. Coating of NDs with an HPMA co-polymer shell improves the colloidal stability of the particles, reduces nonspecific interactions with proteins under physiological conditions, maintains the optical properties of NDs and enables further chemical modification[32,33]. The vicinity of Gd^{3+} complexes (spin labels) acting as stochastically fluctuating magnetic fields can be sensed by NV relaxometry[34–37], providing us a novel route to monitor local

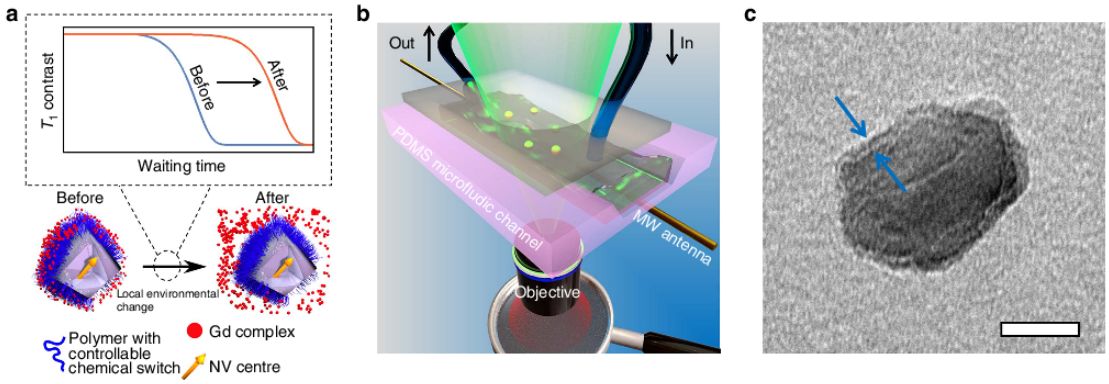

Figure 1 | Basic principle of a ND-based multifunctional sensor. (**a**) Cartoon showing the sensing mechanism of a ND-polymer-Gd hybrid nanosensor in response to a local environmental change. The Gd^{3+} complexes (spin labels attached to the polymer shell on the ND surface) are released after activation of a chemical switch due to a local change, which can be monitored by the change in T_1 relaxation time of NV centres. (**b**) Cartoon showing the experimental setup: polydimethylsiloxane (PDMS) microfluidic channel (pink), pipe system enabling real-time measurement (blue), microwave antenna (gold), optical excitation for NV (green) and fluorescence detection (red). (**c**) Representative TEM image of a polymer-coated ND (ND-HPMA); arrows indicate the polymer shell. Scale bar, 20 nm.

Appendix E

changes. As illustrated in Fig. 1a, the T_1 relaxation time of NV centres in NDs can be quantitatively modulated by the surrounding Gd^{3+} complexes: the more Gd^{3+} complexes loading inside the surface polymer shell, the shorter the T_1 relaxation time. Detachment of Gd^{3+} complexes from the ND particle strongly influences T_1 and can proceed only upon selective cleavage of the linker connecting the complex with the polymer. Importantly, we utilized complexes of Gd^{3+} ions with macrocyclic ligands bearing one phosphonate/phosphinate and three acetate groups, which were originally designed as magnetic resonance imaging (MRI) contrast agents[38]. Thanks to their kinetic inertness and thermodynamic stability, these complexes do not release toxic Gd^{3+} ions under physiological conditions and therefore exhibit excellent biocompatibility and negligible toxicity[39,40]. We developed a convenient synthetic pathway to their modification with cleavable linkers terminated with azido group for attachment to polymers via click chemistry (see Supplementary Methods). To demonstrate the potential applications of the developed nanosensor in cell biology and analytical chemistry, we performed experiments in a home-built microfluidic device made of polydimethylsiloxane (Fig. 1b). The NDs used are in average ~33 nm in diameter with a fairly narrow size distribution[41] (Supplementary Fig. 1) and coated with a HPMA shell a few nanometre thick, as indicated by transmission electron microscopy (TEM) image (Fig. 1c). These NDs contain few NV centres (<10 per particle on average, Supplementary Fig. 2).

Chemical engineering and characterization of the ND surface. To test the utility of our ND-polymer-Gd hybrid nanosensors, we developed two kinds of chemical linkers to sense pH and redox potential, and corresponding nanosensors are denoted as ND@pH and ND@redox particles, respectively (Fig. 2a). ND@pH particles contain an aliphatic hydrazone linker, for which the rate of hydrolytic cleavage is greatly accelerated at lower pHs in the physiologically relevant range[42] (pH 4–8; Fig. 2b). ND@redox particles contain a disulfide linker that can be cleaved into two thiol fragments in reducing environments (in this case, by the presence of glutathione, GSH) (Fig. 2c). As a control, we also synthesized a system with non-cleavable bonds (denoted ND-HPMA-Gd; Fig. 2a). The HPMA polymer is electroneutral but the macrocyclic Gd^{3+} complexes are negatively charged, introducing an overall negative charge to the polymer shell. The electrostatic repulsion between complexes facilitates the departure of the cleaved complexes from the shell.

Based on the NV relaxometry-sensing scheme, the T_1 relaxation time of an NV centre is determined by the number of spins within the effective NV-sensing radius[35]. Therefore, the critical parameter is the actual concentration of Gd^{3+} in the ND nanoenvironment as the relaxation time scales with the Gd^{3+} concentration in the shell (see Supplementary Equations (2, 7, 12)). Either swelling or collapse of the polymer shell would affect this quantity and therefore influence the measured T_1 relaxation time, even if the Gd^{3+} complexes are not released. As polymers can reversibly respond to pH and ionic strength by changes in their hydrodynamic diameters and also by nonspecific adsorption of ions resulting in changes in zeta potential, we studied the influence of these parameters on the behaviour of our nanosensors. First, we measured the size distribution of ND-HPMA-Gd particles (with non-cleavable bonds) in various pH buffers by dynamic light scattering. As shown in Fig. 2d, the hydrodynamic radii of ND-HPMA-Gd in the whole range of buffers were fairly uniform, indicating that the shell thickness of our nanosensor does not change in response to various buffer conditions. In two selected buffers (pH 2.0 and 7.4), we measured

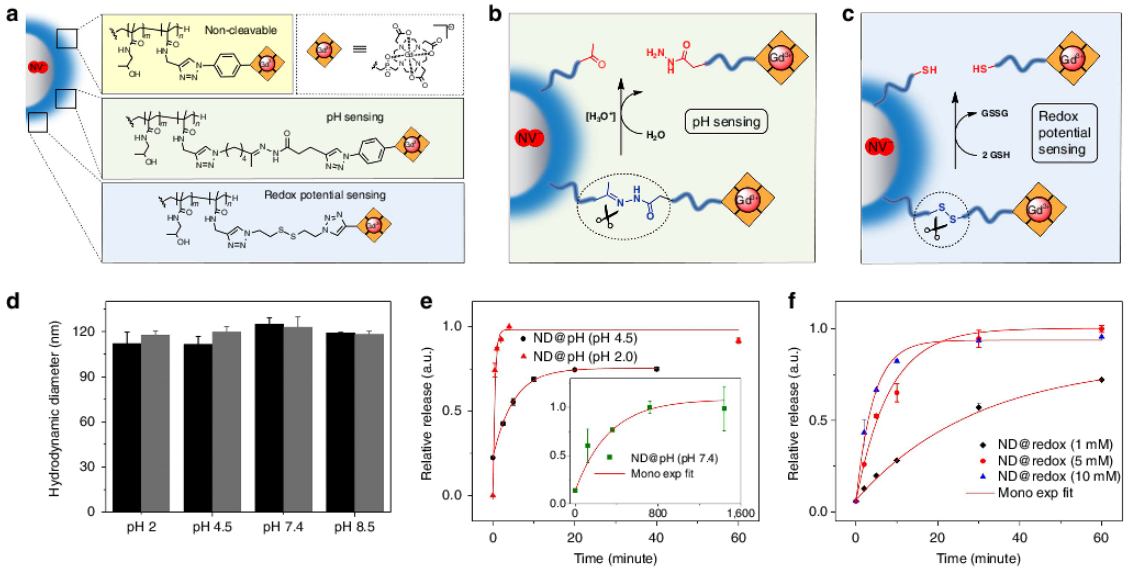

Figure 2 | Design and characterization of ND-polymer-Gd hybrid nanoscale sensors. (**a**) Chemical structure of the polymer interface with Gd^{3+} complexes attached via a non-cleavable and two types of cleavable linkers. The specific release mechanisms for (**b**) pH-dependent hydrolytically cleavable and (**c**) reductively cleavable linkers are shown in detail. (**d**) Hydrodynamic diameters of poly(HPMA)-coated NDs (ND-HPMA, black) and poly(HPMA)-coated NDs modified with non-cleavable Gd^{3+} complexes (ND-HPMA-Gd, grey) determined by dynamic light scattering in different buffers used for Gd-release measurements. (**e**) Release kinetics of Gd^{3+} complexes in ND@pH particles in pH 2.0, 4.5 and 7.4 buffers analysed by ICP MS. The red line is the corresponding mono-exponential fitting. (**f**) Release kinetics of Gd^{3+} complexes in ND@redox particles in the presence of 1, 5 and 10 mM GSH in pH 8.5 buffer analysed by ICP MS. The red line is the corresponding mono-exponential fitting. The error bars in **d–f** represent s.d. from at least three independent measurements.

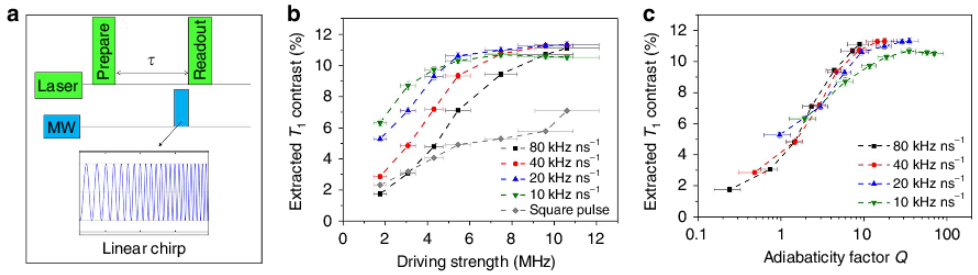

Figure 3 | Robust relaxation measurement with linear chirp pulse. (**a**) Schematic cartoon showing the used optical and microwave pulse sequence for T_1 relaxation measurement. (**b**) Comparison of experimentally extracted contrast of T_1 relaxation measurement with chirp pulse and square pulse for control sample ND-HPMA. The contrast is defined as the normalized initial difference between the sensing sequence with and without the inversion pulse. (**c**) Dependence of extracted T_1 contrast on the extracted minimum adiabaticity factor Q, where Q is defined as the effective driving amplitude over its angular velocity in the rotating frame. The vertical error bars in **b**,**c** represent the s.d. from 20 independent measurements with $\tau \ll T_1$, whereas the horizontal error bars represent the s.e. (95% confidence intervals) from Lorentzian fits (for Fourier transformed Rabi oscillation).

hydrodynamic radii, zeta potentials and T_1 for ND-HPMA-Gd at increasing ionic strengths (up to ~0.25 M, achieved by addition of NaCl and precisely quantified according to the conductivity of the solution). We observed that both pH and ionic strength exert only a marginal influence on hydrodynamic radii (Supplementary Fig. 3a). Although the zeta potentials increased with increasing ionic strength, most likely because of preferential adsorption of sodium ions (Supplementary Fig. 3b), this effect had no influence on T_1 (Supplementary Fig. 3c). This observation confirms the insensitivity of the polymer surface architecture to various environments, which is essential for the construction of stable and robust nanosensors for bio-applications.

To verify whether our nanosensors could release Gd^{3+} complexes on demand, we incubated them in different environments, removed them from solution by centrifugation and analysed the amount of Gd^{3+} complexes in the supernatant with inductively coupled plasma mass spectrometry (ICP MS) as a function of incubation time. This method allowed us to study the temporal evolution of Gd^{3+} complexes release from our nanosensors. As shown in Fig. 2e, the ND@pH particles showed pH-dependent release, whereas the ND-HPMA-Gd (with non-cleavable bonds) particles (Supplementary Fig. 4) were stable under all conditions examined within the current chosen measurement time window (~ 1 h). Furthermore, the slope of the release profile measured at pH 2.0 was two orders of magnitude higher than that for pH 7.4, indicating a much faster cleaving rate of Gd^{3+} complexes from the polymer at low pH values. The very slow change (as shown in insert of Fig. 2e) at pH 7.4 indicates that the sensor can continuously operate for several hours before measurements at lower pH values.

Similarly, the ND@redox particles showed an obvious GSH concentration-dependent release: the higher the applied concentration of GSH, the steeper the release slope (Fig. 2f), whereas the ND-HPMA-Gd control sample (with non-cleavable bonds) were stable in the presence of GSH (Supplementary Fig. 5). All the measured release kinetics for ND@pH and ND@redox particles fit well with standard first-order reaction kinetics

$$C = C_0 e^{-kt} \quad (1)$$

where C_0 is the initial concentration of the reactant and k is the first order rate constant, indicating that the release rate is solely dependent on one specific reactant in solution.

Robust NV spin relaxometry utilizing a linear chirp pulse. Our experiments are based on probing the spin relaxation time T_1 of the NV centre. T_1 is measured by first initializing the NV spin into $m_s = 0$ by an optical pulse. After a waiting time τ, the spin state is readout by an optical excitation pulse generating fluorescence, which is proportional to the population probability of $m_s = 0$. Measuring this fluorescence as a function of the waiting time τ thus determines T_1. However, special care needs to be taken when performing relaxometric measurements on NV centres, as, for example, charge-state fluctuations can mask the T_1 decay in this approach[43]. To derive pristine T_1 curves, one needs to apply an additional microwave pulse in resonance with for example the $m_S = 0$ to $m_S = +1$ spin transition in a second measurement to invert the population of spin state sublevels and subtract the result of both (see Supplementary Discussion). As the spin state has to be manipulated, knowledge about the spin resonance frequency is required. In addition, the excitation power and pulse duration of the used microwave pulse has to be set correctly for a precise state adjustment. Later parameters for their part differ when the orientation of the NV axis to the local microwave field is changed. Therefore, it is highly desirable to use pulse schemas that intrinsically compensate for such variations. In the current study, we optimized the T_1 readout by introducing an adiabatic passage (see Supplementary Discussion) in form of a linear chirp pulse (Fig. 3a), which is robust against detuning and microwave driving power[44]. To compare the performance of different schemes used in T_1 measurement, we extracted the spin contrast from experimental measurement as a function of driving strength (estimated by Rabi oscillations driven on the optically detected magnetic resonance (ODMR) transitions, see Supplementary Fig. 10a) for the control sample ND-HPMA (without Gd^{3+} complexes) (Fig. 3b). The obtained spin contrast decreased as the driving strength reduced for both measurement schemes, but the chirp pulse always resulted in a higher contrast than that obtained with square pulse. We also plotted the extracted spin contrast as a function of expectable minimal adiabaticity factor Q (a measure of the adiabaticity of the used pulse scheme[45]) when using linear chirp pulse at different chirp rate (Fig. 3c). For the data shown in this work using linear chirp pulse, we experimentally obtained a contrast ranging from 4 to 10%, corresponding to a factor Q in the range of around 1.5 up to 10. Indeed, in terms of sensitivity, the chirp pulse resulted in a twofold sensitivity enhancement with different chirp rate when the microwave power is large enough (Supplementary Fig. 6).

Microfluidic measurement of nanosensors. Because of the excellent colloidal stability of our nanosensor under physiological conditions, we performed our T_1 measurements on diffusing NDs (Fig. 4a). We first investigated two kinds of control sample,

Appendix E

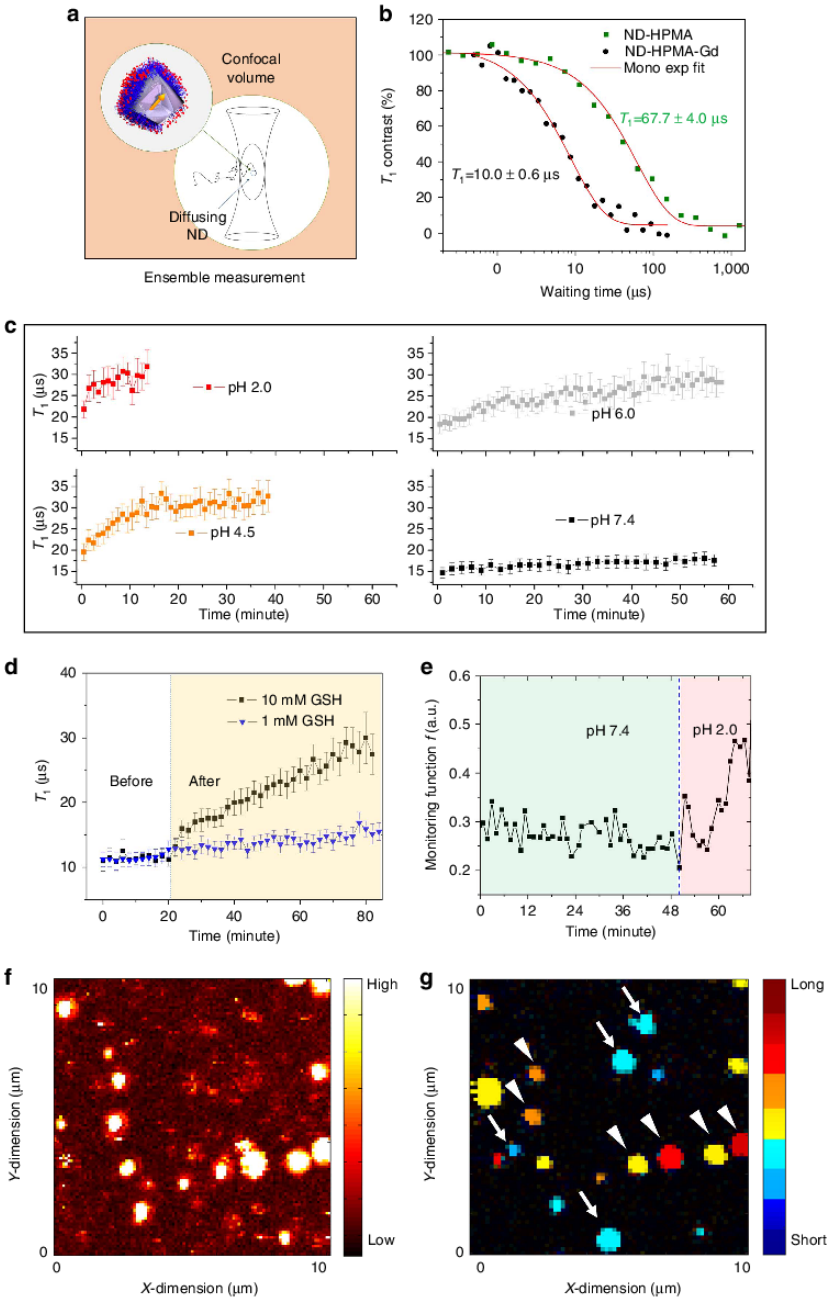

Figure 4 | *In situ* measurements in a microfluidic channel. (**a**) Schematic cartoon showing the ensemble measurements on the averaged T_1 of ND particles diffusing through the confocal volume. (**b**) Typical T_1 ensemble measurement of ND-HPMA and ND-HPMA-Gd (with non-cleavable bond) particles in pH 7.4 buffer. (**c**) Time-dependent ensemble measurement for T_1 of the ND@pH particles when incubated with pH 2.0, 4.5, 6.0 and 7.4 buffers. (**d**) Time-dependent ensemble measurement for T_1 of the ND@redox particles in buffer solution before and after addition of 1 mM (blue) and 10 mM (black) GSH. (**e**) Time-dependent fixed-τ measurement for chosen ND@pH particles when incubated at pH 7.4 followed by a change to pH 2.0 buffer (details are given in Methods). (**f**) Confocal image for the chosen view of ND@pH particles on cover glass in pH 2.0 buffer; the bar indicates the measured fluorescence intensity. (**g**) Reconstructed T_1 contrast image of the same view as in **f** after rinsing with pH 7.4 buffer and adding again freshly prepared ND@pH particles (loaded with Gd^{3+} complexes) in pH 7.4 buffer. White triangles point to old ND@pH particles (Gd^{3+} complexes released), while white arrows point to those newly emerging ones (loaded with Gd^{3+} complexes), the colour bar indicates the extracted T_1 value ranging from short (blue) to long (red). The error bars in **c** and **d** represent the s.e. (95% confidence intervals) from mono exponential decay fits.

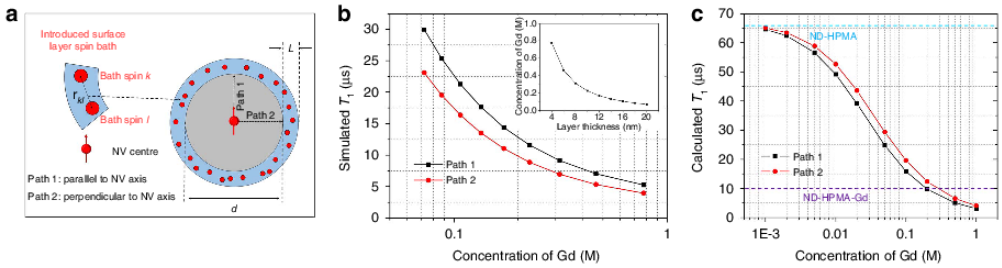

Figure 5 | Simulation for the influence of Gd^{3+} complexes on relaxometry. (**a**) The ND is modeled as a sphere with diameter *d* coated with polymer with thickness *L*. The Gd^{3+} complexes embedded in the polymer layer acts as a randomly fluctuating spin bath. The NV centre is positioned along two orientations (Path 1 and 2). (**b**) The influence of varying HPMA layer thickness (varying concentration of Gd^{3+} complexes) on simulated T_1 value when the number of Gd^{3+} complexes is fixed. The inset shows the concentration of Gd^{3+} complexes versus the layer thickness of the shell (here, $d = 33$ nm and the number of Gd^{3+} complexes was fixed at ~8,000). (**c**) The influence of varying concentrations of Gd^{3+} complexes on calculated T_1 value when the thickness of the polymer layer is fixed ($d = 33$ nm and $L = 10$ nm). The purple dashed line (ND-HPMA-Gd) and blue dashed line (ND-HPMA) denote the lower and upper limit for the measured T_1 value in current study, respectively.

namely ND-HPMA (without Gd^{3+} complexes) and ND-HPMA-Gd (non-cleavable). As shown in Fig. 4b, the ND-HPMA particles had an average measured T_1 value of 67.7 ± 4.0 μs, whereas the ND-HPMA-Gd particle showed a significantly lower value of 10.0 ± 0.6 μs in pH 7.4 buffer. In fact, we also checked the stability of these control samples in all the buffer conditions used in current study (see Supplementary Figs 4 and 5).

We then used the ND@pH particles (pH cleavable) to perform time-dependent T_1 measurement in various conditions including pH 2.0, 4.5, 6.0 and 7.4 (Fig. 4c). At physiological pH environment (pH 7.4), we observed only a slight change for the measured T_1 over a period of 1 h, whereas the T_1 changed dramatically at acidic condition. The measured T_1 curve as a function of the incubation period showed the following behaviour (Fig. 4c): the lower the pH value the steeper the changes in T_1, being consistent with our previous ICP MS measurements (Fig. 2e). Taking a moderate pH (pH 4.5) as an example, the release kinetics of Gd^{3+} complexes (after converting T_1 to a Gd^{3+} concentrations using Supplementary Equations, also see Fig. 5) from ND@pH particles ($\tau_{rel} = 315.7 \pm 42.8$ s) agree excellently with ICP MS measurements ($\tau_{rel} = 306.4 \pm 9.9$ s) (Supplementary Fig. 7). Using set of Britton–Robinson buffers (with equal composition and ionic strength), we also investigated the sensitivity of our sensor in the physiologically relevant pH range (3.7–6.9) for a short measurement time frame (12 min). We estimated the T_1 change rate for each measured pH and found a monotonous dependence on pH (Supplementary Fig. 8) allowing for accuracy of a pH difference at least ~0.7.

Furthermore, we also investigated the change in T_1 of ND@redox nanosensor (cleavable at reduction conditions) in the presence of GSH, an important antioxidant found in most of the animal cells[46]. As shown in Fig. 4d, we observed a mild increase in the T_1 change rate after adding 1 mM GSH and a significant change for 10 mM GSH, while the measured T_1 value was constant before GSH addition.

We can reduce the used measurement schema into fast fixed-τ measurement by directly counting the ratio (monitoring function *f*) of fluorescence signal at two fixed time points[43]. A large monitoring function *f* value indicates a longer relaxation time. As shown in Fig. 4e, the monitoring function *f* kept almost the same in pH 7.4 buffer, but starts to increase once the pH 2.0 buffer is introduced, indicating the increase of T_1 time due to Gd^{3+} complexes release (being consistent with data in Figs 2e and 4c). With the fast measurement scheme, we can perform T_1 contrast imaging on several different NDs in a confocal scanning approach. To demonstrate this, we first incubated ND@pH particles in pH 2.0 buffer as shown in Fig. 4f, followed by rinsing with pH 7.4 buffer and adding again freshly prepared ND@pH particles in pH 7.4 buffer. Next, we performed fixed-τ measurement for each pixel within the chosen field of view and reconstructed a T_1 contrast image shown in Fig. 4g. ND@pH particles that were not subject to low pH (white arrows in Fig. 4g) showed short T_1 times, whereas particles that were subject to pH 2.0 (white triangles in Fig. 4g) showed long T_1 times, as most of their loaded Gd^{3+} complexes had been released during pH 2.0 treatment. This is consistent with the statistical view of T_1 observations for the sample ND@pH, indicating significant different T_1 in two different pH buffers (pH 2.0 and pH 7.4; Supplementary Fig. 9).

Modelling the NV relaxometry modulated by Gd^{3+} complexes. To fully understand the observed effects, we started with the model description[47] and revised it to describe the function of our nanosensors (see Supplementary Methods). As shown in Fig. 5a, we modelled a single ND particle as a sphere and considered the introduced Gd^{3+} complexes as randomly fluctuating spin bath inside the polymer shell at the beginning. As the actual position of our NV centre in the crystal is not known, we considered various positions of the NV centre between the centre and the edge of the sphere. By this we derive an average value of the simulated T_1. From measurements using ICP atomic emission spectroscopy (AES), we obtained the average content of Gd^{3+} complexes in ND particles ~3.2%. Therefore, we can estimate the approximate number of Gd^{3+} complexes is around 8,000 per particle if we assume an average diameter of NDs as 33 nm, equivalent to the average value obtained from our TEM measurements (Supplementary Fig. 1). To estimate the shell thickness of the HPMA for the given sample in the used buffer solutions, we fixed the number of Gd^{3+} complexes inside the polymer shell and varied its thickness to investigate the corresponding T_1 change. In this way, we derive the T_1 value as a function of shell thickness as shown in Fig. 5b. The measured T_1 of ND-HPMA-Gd is ~10 μs (Fig. 4b) pointing to ~0.2 M Gd^{3+} concentration in our simulation (Fig. 5b) with a ~10 nm shell (insert in Fig. 5b). This shell thickness is similar with our TEM observation in Fig. 1c and Supplementary Fig. 1, and we used it in all further analysis steps. One could also account for paramagnetic centres lying on the surface of NDs[47], but as we know the relaxation rate for the situation when the Gd^{3+} is absent, we can use the already gained T_1 time from the control sample ND-HPMA as a basis

Appendix E

offset. The measured T_1 value was 67.7 μs (Fig. 4b) for the control sample ND-HPMA in buffer solutions. We interpreted this as the intrinsic relaxation rate

$$R^{\mathrm{int}} = \frac{1}{T_1^{\mathrm{int}}} \quad (2)$$

where $T_1^{\mathrm{int}} = 67.7\mu s$ of the nanosensors in solution and calculated the expected relaxation T_1 time (Fig. 5c) using

$$T_1^{\mathrm{Calculated}} = \left(R^{\mathrm{int}} + R^{\mathrm{Gd}}\right)^{-1} \quad (3)$$

where R^{int} is the intrinsic relaxation rate and R^{Gd} is the simulated relaxation rate induced by Gd^{3+} complexes. From this, we can deduct that we are able to detect Gd^{3+} complexes with concentration ranging from 0.2 M (~8,000 Gd^{3+} complexes per particle) down to 0.001 M (~40 Gd^{3+} complexes per particle), corresponding to the measured highest (purple dashed line in Fig. 5c) and lowest (blue dashed line in Fig. 5c) Gd content, respectively.

Discussion

Our hybrid nanosensor achieves signal transduction, recording and amplification simultaneously. Subtle changes in physiological systems (weak signals) can be recorded by counting the variance of Gd^{3+} complexes (strong interaction with NV centres) inside the polymer shell due to a programmed chemical reaction. The well-fitted first-order reaction equation for measured release kinetics (Fig. 2e,f and Supplementary Fig. 7) indicates that our nanosensor responds to changes in a single, pre-defined chemical parameter. Importantly, the thickness of the polymer shell was insensitive to pH and ionic strength (Fig. 2d and Supplementary Fig. 3a). We observed neither swelling nor collapse of the polymer shell in any of the conditions used. Consistently, we observed no influence of these factors on T_1 (Supplementary Fig. 3c), which is critical for reliable and robust function of the nanosensors in biological environments.

The excellent agreement between the experimental results (Fig. 4b) and theoretical modelling (Fig. 5c) indicates the underlying mechanism: the change in T_1 relaxation time is caused by release of Gd^{3+} complexes from the polymer shell. Precise agreement of ICP MS with T_1 kinetic measurements (Supplementary Fig. 7) suggests the high accuracy and sensitivity of the current detection method. In principle, we can monitor gradual release down to several tens of molecules of Gd^{3+} complexes (Fig. 5c) at a single-particle level (Fig. 4e–g), which allows us to monitor a localized chemical process occurring on an extremely small scale (~10^{-22}–10^{-20} mol). Although the achieved accuracy (~0.7 pH unit) is lower compared with the current, most sensitive measurement techniques[48] (~0.1 pH unit for intracellular measurement), our system operates in quite a broad pH range. In contrast, for some optical pH sensors, which exhibit a sigmoidal response towards changes in pH, their narrow dynamic range represent often a limitation[49]. Considering practical measurements in cells, the accuracy of our sensor is sufficient, as pH differences between extracellular space, cytosol and some organelles are much higher than 0.7. For example, the cytosol pH is ~7.4, whereas endo/lysosomal compartments show pH ~4.5 (ref. 50). Similarly, the intracellular GSH concentrations usually range from 0.5 to 10 mM, whereas extracellular values are almost three orders of magnitude lower[51]. These differences are in a range well measurable by our nanosensor.

Many of the currently used nanosensors are based on mechanisms, which are either irreversible (based on formation or cleavage of covalent bonds) or practically irreversible, because the formed non-covalent sensing assembly is extremely stable (for instance, nucleic acid hybridization, antibody and aptamer affinity probes, fluorescence resonance energy transfer sensors utilizing cleavage reactions[52]). Irreversibility is typical also for current approaches to detect GSH[53,54]. The chemical nature of our sensing mechanism also renders our scheme irreversible, which limits the possible durations of measurements, especially for higher cleavage rates. To enlarge the measurement window to basically unlimited time, we are currently developing a reversibly responding polymer coating on NDs, which operates without a need of irreversible cleavage events.

For a typical T_1 measurement with an additional control sequence using a square pulse, one needs to find the resonance frequency and the length of used pulse to effectively invert the spin population. This is especially important for NDs, because their NV centres are typically arbitrary oriented and with a strain-induced variation in resonance frequency[23]. In comparison, the used linear chirp pulse scheme simplifies T_1 measurements into a single step: direct T_1 measurement by applying chirp pulse acting as 'inversion pulse' without any preliminary measurements for identifying the resonance frequency and pulse length. In addition, the chirp pulse scheme results in enhanced sensitivity compared to that with a square pulse (Fig. 3 and Supplementary Fig. 6). This is also consistent with our simulation of NV spin state evolution excited by different pulse scheme: the square pulse is sensitive to the changes in microwave excitation while the linear chirp pulse is much more robust, especially in the presence of inhomogeneous ODMR line broadening (see Supplementary discussion and Supplementary Fig. 10). Thus, the chirp pulse scheme enables robust T_1 measurement on different NDs simultaneously (ensemble measurement).

In conclusion, our hybrid nanosensor, owing to its versatility, can serve as a general platform with potential applications ranging from catalytic chemistry to cell biology and physiology, especially for label-free three-dimensional imaging of physiological variables by optical means. Development of molecular-sized NDs with NV centres[55,56] can further increase the sensitivity of the current method due to improved spin sensitivity of NV centres.

Methods

Experimental setup. In the current study, we adapted a confocal microscopy apparatus. The laser (CNI, CW DPSS Laser 532 nm) was directed through acousto-optic modulator (AOM) and focused onto the focal plane of a ×60 water-immersion objective (Olympus) for the ensemble measurements and a ×60 oil objective (Olympus) when measuring individual NDs. The fluorescence of NV centre was filtered (long pass, cutoff at 647 nm) and collected by two avalanche photo diode (Perkin-Elmer) in Hanbury-Brown and Twist configuration. Resonant microwave manipulation of the NV centre was achieved using a spanned copper wire inside a home-built microfluidic channel made of transparent poly-dimethylsiloxane (Sylgard 184 silicone elastomer kit, Dow Corning) in the vicinity of the optical focus. Two small plastic tubes are used to exchange the solution in the microfluidic channel.

Preparation of ND-polymer-Gd nanosensors. Detailed descriptions for preparation of fluorescent NDs with NV centres[57], their coating with HPMA polymer and synthesis of Gd^{3+} complexes can be found in the Supplementary Information. Briefly, alkyne-modified HPMA-coated NDs were decorated with azide-modified Gd^{3+} complexes using Cu(I)-catalysed azide-alkyne cycloaddition (CuACC). HPMA-coated NDs (10 mg in a final reaction volume of 12.8 ml of 50 mM HEPES buffer, pH 7.4) were mixed with either non-cleavable Gd^{3+} complexes or Gd^{3+} complexes with hydrazone or disulfide linker (in final concentrations of 0.96, 1.92 and 2.4 mM, respectively), pre-mixed 0.32 mM $CuSO_4$ and 0.64 mM tris(3-hydroxypropyltriazolylmethyl)amine ligand, and a freshly prepared solution of sodium ascorbate (5 mM). The reaction mixture was well sealed, left for 1 h with no stirring and washed by centrifugation with water (Gd^{3+} conjugates with non-cleavable linker, ND-HPMA-Gd and disulfide linker, ND@redox) or methanol (Gd^{3+} conjugate with hydrazone linker, ND@pH). The resulting nanosensors were stored in water (ND-HPMA-Gd and ND@redox) or in dry methanol (ND@pH) at 4 °C.

Characterization of ND-polymer-Gd nanosensors. The morphology and size of the particles were characterized with TEM (JEOL JEM-1011)[58]. The stability and

surface charge of HPMA-coated NDs with Gd^{3+} complexes were tested by dispersing them in buffer solutions (50 mM citric acid buffer pH 2.0, 50 mM acetate buffer pH 4.5, 50 mM HEPES buffer pH 7.4, 50 mM TRIS buffer pH 8.5 and 1.5 M PBS buffer pH 7.4) for further experiments. Dynamic light scattering and zeta potential were recorded with a Zetasizer Nano ZS system (Malvern Instruments) at 37 °C at a concentration of 0.1 mg ml^{-1}.

To quantitatively measure the amount of Gd^{3+} complexes released from the nanosensors, the particles were mixed with buffer and incubated for a certain time. Then, cleavage conditions were stopped, the particles were centrifuged and the released Gd^{3+} complexes in supernatant were measured with an ICP MS 7700 (Agilent Technologies) instrument in duplicates. The non-cleavable ND-HPMA-Gd^{3+} conjugate was used as a control and processed under the same conditions. The relative release at a given time was calculated as a ratio of the amount released to the maximum release amount. A detailed description of these release experiments can be found in the Supplementary Information. The total amount of Gd^{3+} conjugated to HPMA-coated NDs was measured as ~3.2% (weight percentage to NDs) using ICP AES (Spectro Arcos SOP).

Relaxation measurement with linear chirp pulse. For full T_1 relaxometry measurement, laser light modulation was achieved by passing continuous wave laser through an acousto-optical modulator for polarization and readout of NV centres. We first applied a laser pulse for polarizing NV centres into $m_s=0$ (initialization) and then wait for the time τ, followed by another laser pulse to detect NV fluorescence revealing the spin state (readout). Afterwards, we applied a similar sequence that differs from the first one, by adding a microwave pulse before the readout. The microwave pulse (linear chirp) is generated by mixing the output of one microwave source (SMIQ 03B, Rhode & Schwarz) with an arbitrary waveform generator (AWG2041, Tectronixs) and amplified by a microwave amplifier (ZHL-16W-43+, mini circuits). The linear chirp microwave pulse starts from 2.845 GHz and is swept over 100 MHz (covering most of the detuning range in NDs) at certain speed. The chirp speed was kept as 10–100 kHz ns^{-1}. The obtained difference in fluorescence $\Delta F(\tau)$ is proportional to the residual spin polarization after time τ of only those NV centres excited by microwave pulse. We thus further normalized the obtained $\Delta F(\tau)$ (named T_1 contrast)[43], fitted it with a single exponential function:

$$\Delta F(\tau) = A e^{-\tau/T_1} \quad (4)$$

to get an average decay constant T_1 value. For comparison of a chirp pulse with a square pulse for effective spin state inversion during T_1 measurement, 10 µl poly(HPMA)-coated NDs (4 mg ml^{-1} in water) were dropped in the vicinity of the copper wire on top of cover glass and air dried. The analysed detection volume contains more than several hundreds of NV centres, estimated on the detected photon flux in this experiment in comparison with that detected from a single NV centre measured with the same setup. The focal point of the laser was tuned to any position of the dense packed NDs nearby the copper wire for ensemble measurements (all the NDs inside the focus volume). At different microwave power, we performed T_1 measurement through both square pulse and chirp pulse with different sweeping speed. The adiabaticity factor Q is defined as the effective Larmor precession around the effective magnetic field in the rotating frame over the angular change of the field[45]. The driving strength is defined as the effective Rabi frequency of an ensemble of NV centres driven by an external microwave. To quantify the performance of individual scheme in an experiment, the sensitivity enhancement factor is calculated as ratio of power noise equivalents δT_1 of the different pulse scheme:

$$\mathrm{EF} = \frac{\delta T_1^{\mathrm{chirp}}}{\delta T_1^{\mathrm{square}}} = \frac{c_{\mathrm{chirp}}}{c_{\mathrm{square}}} \cdot \sqrt{\frac{t_{\mathrm{square}}}{t_{\mathrm{chirp}}}} \quad (5)$$

where c is the contrast and t is the cycle time of the measurement.

NV relaxometry measurements in a microfluidic channel. For all time-dependent T_1 measurements (Fig. 4 and Supplementary Fig. 9), the freshly prepared nanosensor particles were dispersed in the respective buffer at a concentration of approximately 100 µg ml^{-1} and were injected into a microfluidic channel through the conjugated tube. In case of the ensemble measurement we used a PDMS chamber that can be opened and covered from top. The focal point of the laser was placed to any position inside the channel for ensemble measurements (all the free diffusing particles). For fixed τ measurement, we only collected the fluorescence signal (F) at two fixed time points ($\tau_1=0.001$ µs and $\tau_2=20$ µs) on the obtained full T_1 curve of chosen ND spot and compare the change of T_1 by monitoring function:

$$f = F(\tau_2)/F(\tau_1) \quad (6)$$

Data availability. Data supporting the findings of this study are available within the article and its Supplementary Information files and from the corresponding authors upon reasonable request.

References

1. Orrenius, S., Zhivotovsky, B. & Nicotera, P. Regulation of cell death: the calcium-apoptosis link. *Nat. Rev. Mol. Cell Biol.* **4,** 552–565 (2003).
2. Winterbourn, C. C. Reconciling the chemistry and biology of reactive oxygen species. *Nat. Chem. Biol.* **4,** 278–286 (2008).
3. Wu, J. & Kaufman, R. J. From acute ER stress to physiological roles of the unfolded protein response. *Cell Death Differ.* **13,** 374–384 (2006).
4. He, L. & Hannon, G. J. MicroRNAs: small RNAs with a big role in gene regulation. *Nat. Rev. Genet.* **5,** 522–531 (2004).
5. Casey, J. R., Grinstein, S. & Orlowski, J. Sensors and regulators of intracellular pH. *Nat. Rev. Mol. Cell Biol.* **11,** 50–61 (2010).
6. Schafer, F. Q. & Buettner, G. R. Redox environment of the cell as viewed through the redox state of the glutathione disulfide/glutathione couple. *Free Radic. Biol. Med.* **30,** 1191–1212 (2001).
7. Domaille, D. W., Que, E. L. & Chang, C. J. Synthetic fluorescent sensors for studying the cell biology of metals. *Nat. Chem. Biol.* **4,** 168–175 (2008).
8. Howes, P. D., Chandrawati, R. & Stevens, M. M. Bionanotechnology. Colloidal nanoparticles as advanced biological sensors. *Science* **346,** 1247390 (2014).
9. Zhang, J., Campbell, R. E., Ting, A. Y. & Tsien, R. Y. Creating new fluorescent probes for cell biology. *Nat. Rev. Mol. Cell Biol.* **3,** 906–918 (2002).
10. Schrand, A. M. *et al.* Are diamond nanoparticles cytotoxic? *J. Phys. Chem. B* **111,** 2–7 (2007).
11. Mochalin, V. N., Shenderova, O., Ho, D. & Gogotsi, Y. The properties and applications of nanodiamonds. *Nat. Nanotechnol.* **7,** 11–23 (2012).
12. Zhu, Y. *et al.* The biocompatibility of nanodiamonds and their application in drug delivery systems. *Theranostics* **2,** 302–312 (2012).
13. Fang, C. Y. *et al.* The exocytosis of fluorescent nanodiamond and its use as a long-term cell tracker. *Small* **7,** 3363–3370 (2011).
14. Mohan, N., Chen, C. S., Hsieh, H. H., Wu, Y. C. & Chang, H. C. *In vivo* imaging and toxicity assessments of fluorescent nanodiamonds in *Caenorhabditis elegans*. *Nano Lett.* **10,** 3692–3699 (2010).
15. Balasubramanian, G. *et al.* Nanoscale imaging magnetometry with diamond spins under ambient conditions. *Nature* **455,** 648–651 (2008).
16. Maze, J. R. *et al.* Nanoscale magnetic sensing with an individual electronic spin in diamond. *Nature* **455,** 644–647 (2008).
17. Gruber, A. *et al.* Scanning confocal optical microscopy and magnetic resonance on single defect centers. *Science* **276,** 2012–2014 (1997).
18. Chow, E. K. *et al.* Nanodiamond therapeutic delivery agents mediate enhanced chemoresistant tumor treatment. *Sci. Transl. Med.* **3,** 73ra21 (2011).
19. Kuo, Y., Hsu, T. Y., Wu, Y. C. & Chang, H. C. Fluorescent nanodiamond as a probe for the intercellular transport of proteins *in vivo*. *Biomaterials* **34,** 8352–8360 (2013).
20. Chu, Z. *et al.* Rapid endosomal escape of prickly nanodiamonds: implications for gene delivery. *Sci. Rep.* **5,** 11661 (2015).
21. Zhang, T. *et al.* Photoacoustic contrast imaging of biological tissues with nanodiamonds fabricated for high near-infrared absorbance. *J. Biomed. Opt.* **18,** 26018 (2013).
22. Chu, Z. *et al.* Unambiguous observation of shape effects on cellular fate of nanoparticles. *Sci. Rep.* **4,** 4495 (2014).
23. McGuinness, L. P. *et al.* Quantum measurement and orientation tracking of fluorescent nanodiamonds inside living cells. *Nat. Nanotechnol.* **6,** 358–363 (2011).
24. Kucsko, G. *et al.* Nanometre-scale thermometry in a living cell. *Nature* **500,** 54–58 (2013).
25. Petrakova, V. *et al.* Imaging of transfection and intracellular release of intact, non-labeled DNA using fluorescent nanodiamonds. *Nanoscale* **8,** 12002–12012 (2016).
26. Dolde, F. *et al.* Electric-field sensing using single diamond spins. *Nat. Phys.* **7,** 459–463 (2011).
27. Neumann, P. *et al.* High-precision nanoscale temperature sensing using single defects in diamond. *Nano Lett.* **13,** 2738–2742 (2013).
28. Toyli, D. M., Charles, F., Christle, D. J., Dobrovitski, V. V. & Awschalom, D. D. Fluorescence thermometry enhanced by the quantum coherence of single spins in diamond. *Proc. Natl Acad. Sci. USA* **110,** 8417–8421 (2013).
29. Doherty, M. W. *et al.* Electronic properties and metrology applications of the diamond NV− center under pressure. *Phys. Rev. Lett.* **112,** 047601 (2014).
30. Momenzadeh, S. A. *et al.* Thin circular diamond membrane with embedded nitrogen-vacancy centers for hybrid spin-mechanical quantum systems. *Phys. Rev. Applied* **6,** 024026 (2016).
31. Neburkova, J., Vavra, J. & Cigler, P. Coating nanodiamonds with biocompatible shells for applications in biology and medicine. *Curr. Opin. Solid State Mater. Sci.* **21,** 43–53 (2017).
32. Slegerova, J. *et al.* Designing the nanobiointerface of fluorescent nanodiamonds: highly selective targeting of glioma cancer cells. *Nanoscale* **7,** 415–420 (2015).
33. Rehor, I. *et al.* Fluorescent nanodiamonds with bioorthogonally reactive protein-resistant polymeric coatings. *ChemPlusChem* **79,** 21–24 (2014).
34. Ermakova, A. *et al.* Detection of a few metallo-protein molecules using color centers in nanodiamonds. *Nano Lett.* **13,** 3305–3309 (2013).

Appendix E

35. Steinert, S. *et al.* Magnetic spin imaging under ambient conditions with sub-cellular resolution. *Nat. Commun.* **4,** 1607 (2013).
36. Kaufmann, S. *et al.* Detection of atomic spin labels in a lipid bilayer using a single-spin nanodiamond probe. *Proc. Natl Acad. Sci. USA* **110,** 10894–10898 (2013).
37. Sushkov, A. O. *et al.* All-optical sensing of a single-molecule electron spin. *Nano Lett.* **14,** 6443–6448 (2014).
38. Rudovský, J. *et al.* Lanthanide(III) complexes of a mono(methylphosphonate) analogue of H_4dota: the influence of protonation of the phosphonate moiety on the TSAP/SAP isomer ratio and the water exchange rate. *Chemistry* **11,** 2373–2384 (2005).
39. Försterová, M. *et al.* Thermodynamic study of lanthanide(III) complexes with bifunctional monophosphinic acid analogues of H_4dota and comparative kinetic study of yttrium (III) complexes. *Dalton Trans.* 535–549 (2007).
40. Kotková, Z. *et al.* Cyclodextrin-based bimodal fluorescence/MRI contrast agents: an efficient approach to cellular imaging. *Chemistry* **16,** 10094–10102 (2010).
41. Havlik, J. *et al.* Benchtop fluorination of fluorescent nanodiamonds on a preparative scale: toward unusually hydrophilic bright particles. *Adv. Funct. Mater.* **26,** 4134–4142 (2016).
42. Hrubý, M., Koňák, Č. & Ulbrich, K. Polymeric micellar pH-sensitive drug delivery system for doxorubicin. *J. Control Release* **103,** 137–148 (2005).
43. Häberle, T., Schmid-Lorch, D., Reinhard, F. & Wrachtrup, J. Nanoscale nuclear magnetic imaging with chemical contrast. *Nat. Nanotechnol.* **10,** 125–128 (2015).
44. Niemeyer, I. *et al.* Broadband excitation by chirped pulses: application to single electron spins in diamond. *New J. Phys.* **15,** 033027 (2013).
45. Garwood, M. & DelaBarre, L. The return of the frequency sweep: designing adiabatic pulses for contemporary NMR. *J. Magn. Reson.* **153,** 155–177 (2001).
46. Wu, G., Fang, Y.-Z., Yang, S., Lupton, J. R. & Turner, N. D. Glutathione metabolism and its implications for health. *J. Nutr.* **134,** 489–492 (2004).
47. Tetienne, J.-P. *et al.* Spin relaxometry of single nitrogen-vacancy defects in diamond nanocrystals for magnetic noise sensing. *Phys. Rev. B* **87,** 235436 (2013).
48. Ray, A., Yoon, H. K., Lee, Y. E. K., Kopelman, R. & Wang, X. Sonophoric nanoprobe aided pH measurement *in vivo* using photoacoustic spectroscopy. *Analyst* **138,** 3126–3130 (2013).
49. Wencel, D., Abel, T. & McDonagh, C. Optical chemical pH sensors. *Anal. Chem.* **86,** 15–29 (2013).
50. Grant, B. D. & Donaldson, J. G. Pathways and mechanisms of endocytic recycling. *Nat. Rev. Mol. Cell Biol.* **10,** 597–608 (2009).
51. Lushchak, V. I. Glutathione homeostasis and functions: potential targets for medical interventions. *J. Amino Acids* **2012,** 736837 (2012).
52. Howes, P. D., Chandrawati, R. & Stevens, M. M. Colloidal nanoparticles as advanced biological sensors. *Science* **346,** 1247390 (2014).
53. Jung, H. S., Chen, X., Kim, J. S. & Yoon, J. Recent progress in luminescent and colorimetric chemosensors for detection of thiols. *Chem. Soc. Rev.* **42,** 6019–6031 (2013).
54. Wang, K., Peng, H. & Wang, B. Recent advances in thiol and sulfide reactive probes. *J. Cell Biochem.* **115,** 1007–1022 (2014).
55. Vlasov, I. I. *et al.* Molecular-sized fluorescent nanodiamonds. *Nat. Nanotechnol.* **9,** 54–58 (2014).
56. Boudou, J.-P. *et al.* Fluorescent nanodiamonds derived from HPHT with a size of less than 10nm. *Diam. Relat. Mater.* **37,** 80–86 (2013).
57. Stursa, J. *et al.* Mass production of fluorescent nanodiamonds with a narrow emission intensity distribution. *Carbon* **96,** 812–818 (2016).
58. Rehor, I. & Cigler, P. Precise estimation of HPHT nanodiamond size distribution based on transmission electron microscopy image analysis. *Diam. Relat. Mater.* **46,** 21–24 (2014).

Acknowledgements

The authors thank Philipp Neumann, Thomas Häberle and Florestan Ziem for fruitful discussions, Matthias Widmann for his assistance with drawing illustration cartoons in Fig. 1, Tomas Matousek for ICP MS measurements, and David Chvatil and Jan Stursa (Nuclear Physics Institute AS CR, Czech Republic) for irradiation of nanodiamonds, which was supported by grant project RVO61389005. P.C. and J.N. acknowledges the support from the Grant Agency of the Czech Republic (Project Number 16-16336S). J.K. and O.Z. acknowledge the support from the Grant Agency of the Czech Republic (Project Number 16-03156S). J.W. acknowledges funding by the DFG via SPP 1601 and FOR 1493, the Volkswagenstiftung and the EU via the IP DIADEMS.

Author contributions

Z.Q.C., P.C. and J.W. conceived the idea. T.R. designed and carried out all the optical measurements. J.N., O.Z. and J.K. performed all materials synthesis and characterization. A.Z. prepared all the buffer solution involved in optical measurements and participated in the optimization for optical measurements. T.R. carried out the theoretical calculations. T.R., Z.Q.C. and P.C. analysed the data. J.W. supervised the project. Z.Q.C., P.C. and J.W. wrote the manuscript with the comments from all co-authors. All authors discussed the results and commented on the manuscript.

Additional information

Supplementary Information accompanies this paper at http://www.nature.com/naturecommunications

Competing financial interests: The authors declare no competing financial interests.

Reprints and permission information is available online at http://npg.nature.com/reprintsandpermissions/

How to cite this article: Rendler, T. *et al.* Optical imaging of localized chemical events using programmable diamond quantum nanosensors. *Nat. Commun.* **8,** 14701 doi: 10.1038/ncomms14701 (2017).

Publisher's note: Springer Nature remains neutral with regard to jurisdictional claims in published maps and institutional affiliations.

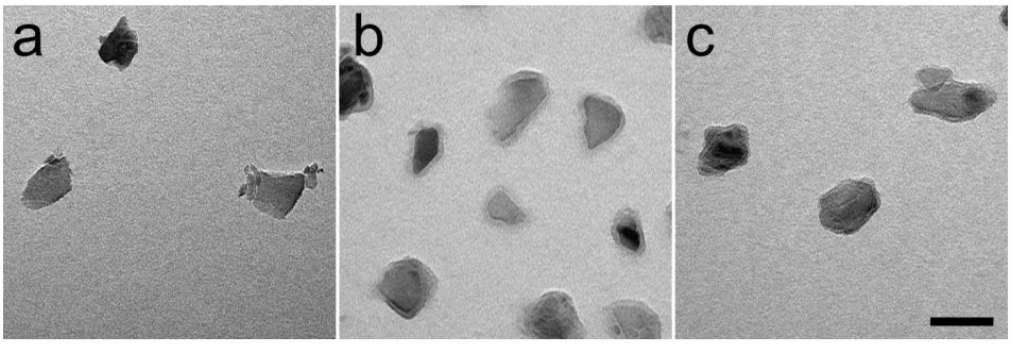

Supplementary Figure 1. Typical TEM image of various ND particles. (**a**) non-coated oxidized NDs. (**b**) Polymer coated ND-HPMA. (**c**) ND@redox. The scale bar represents 50 nm.

Appendix E

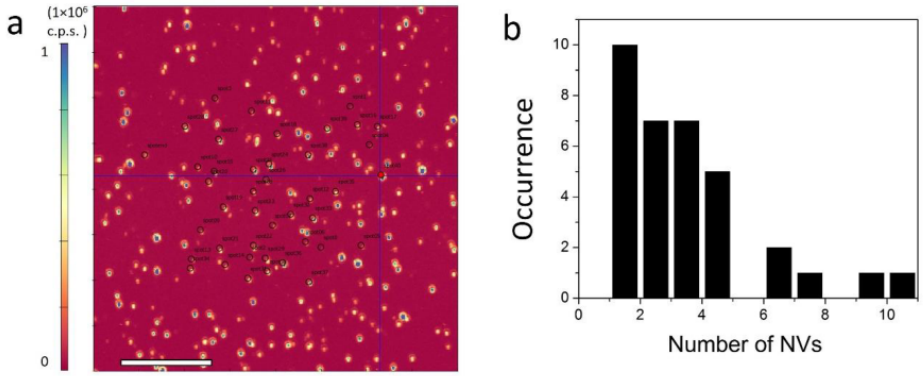

Supplementary Figure 2. Number of NV centers per particle. The number was calculated through analysis of 40 randomly chosen ND particles. (**a**) Typical confocal image of ND-HPMA particles dispersed on top of coverglass. The scale bar represents 10 μm. (**b**) The distribution of the number of NV centers in selected (marked with black circle) spots in (**a**); the number of NV centers in an individual particle was determined from the autocorrelation function $g^{(2)}(\tau)$.

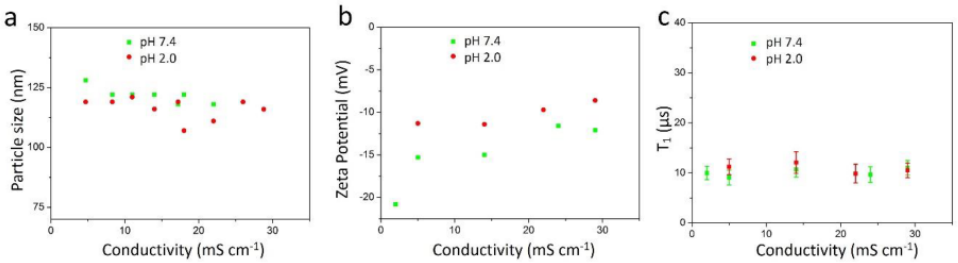

Supplementary Figure 3. The influence of ionic strength on the behavior of ND-HPMA-Gd. (**a**) Hydrodynamic radii, (**b**) zeta potentials, and (**c**) T_1 ensemble measurement of ND-HPMA-Gd in pH 7.4 and pH 2.0 buffers. The ionic strength is expressed as conductivity.

Appendix E

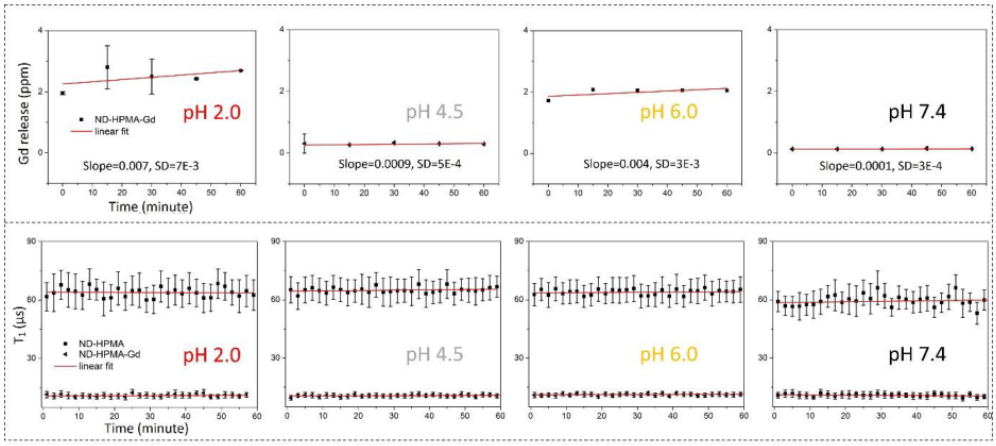

Supplementary Figure 4. Behavior of the control sample in different pH buffers. Release kinetics of Gd^{3+}-complex from ND-HPMA-Gd (non-cleavable) checked by ICP MS (upper panel) in different buffers (pH 2.0, 4.5, 6.0, and 7.4). Time-dependent ensemble measurement for T_1 (lower panel) of ND-HPMA and ND-HPMA-Gd (non-cleavable) in different buffers (pH 2.0, 4.5, 6.0, and 7.4). The slope of all linear fit is approaching zero, indicating negligible change of Gd^{3+} -complex within the measurement time period.

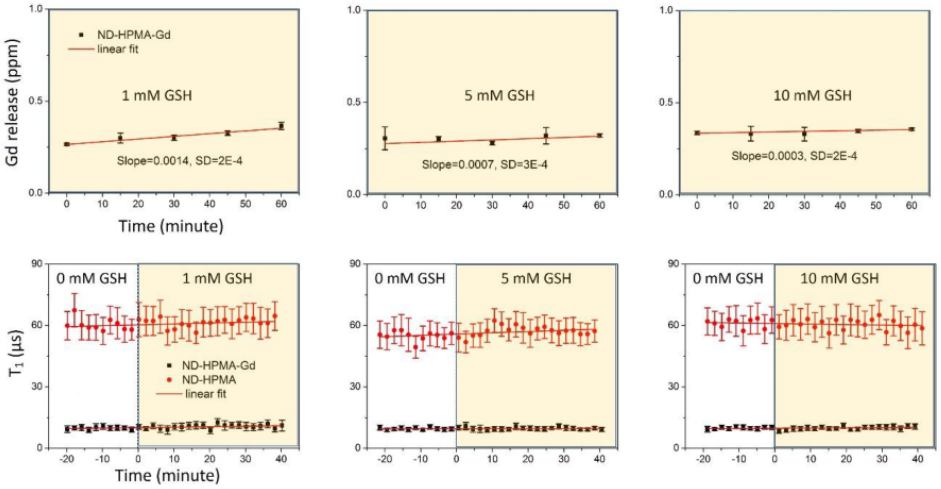

Supplementary Figure 5. The behavior of the control sample in buffers containing GSH. Release kinetics of Gd^{3+}-complex from ND-HPMA-Gd (non-cleavable) checked by ICP MS (upper panel) in different GSH buffers (1 mM, 5 mM and 10 mM GSH). Time-dependent ensemble measurement for T_1 (lower panel) of ND-HPMA and ND-HPMA-Gd (non-cleavable) in different GSH buffers (1 mM, 5 mM and 10 mM). The slope of all linear fit is approaching zero, indicating negligible change of Gd^{3+} complex within the measurement time period.

Appendix E

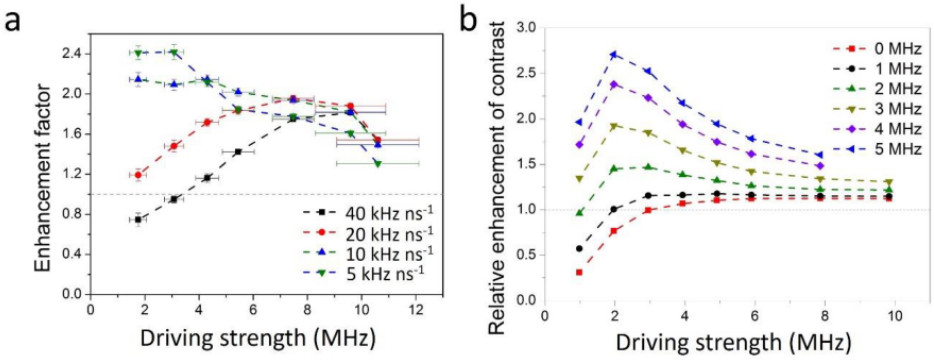

Supplementary Figure 6. Relative enhancement for chirp pulse versus a square pulse. (**a**) Comparison of experimentally obtained enhancement in sensitivity between T_1 relaxation measurement with linear chirp pulse over square pulse; the enhancement factor is calculated as the ratio of sensitivity obtained with linear chirp pulse to that with square pulse. The vertical error bars represent the standard deviations from 20 independent measurements with $\tau \ll T_1$, while the horizontal error bars represent the standard errors (95% confidence intervals) from Lorentzian fits (for Fourier transformed Rabi oscillation). (**b**) Simulation of relative enhancement of the probability to depopulate the NV $m_s = 0$ sublevel after applying linear chirp pulse over square pulse with different microwave driving strength.

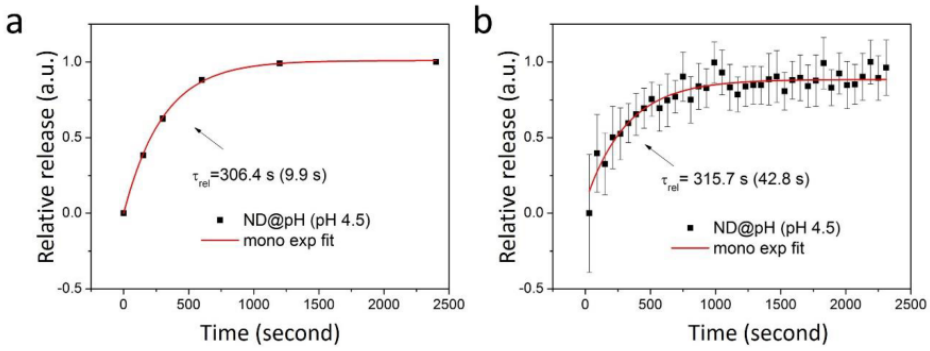

Supplementary Figure 7. Release kinetics of Gd^{3+} complexes. The results were obtained by (**a**) ICP MS and (**b**) ensemble T_1 measurement (ND@pH particles in pH 4.5 buffer). The standard deviations are stated in parentheses.

Appendix E

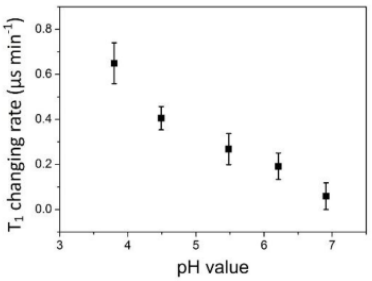

Supplementary Figure 8. Dependence of the fitted T_1 changing rate of ND@pH nanosensor on pH. Six T_1 measurement points (120 seconds per point) were linearly fitted to extract the actual T_1 change rate corresponding to a particular pH. Britton-Robinson buffers with same composition were used. Their conductivity was normalized using KCl to ensure environment with equal ionic strength for all measurements.

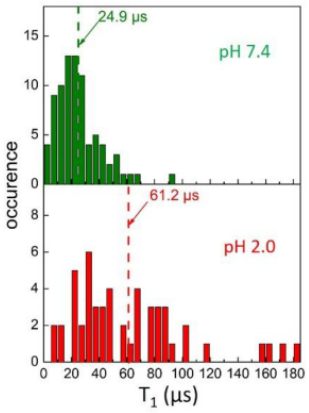

Supplementary Figure 9. Statistical view of ND@pH nanosensors in pH 7.4 and pH 2.0 buffers. After injecting the sample into a microfluidic chamber, the individual relaxation times for different adsorbed ND@pH nanosensors had been measured at pH 7.4 (green) and after changing to pH 2.0 (red).

Appendix E

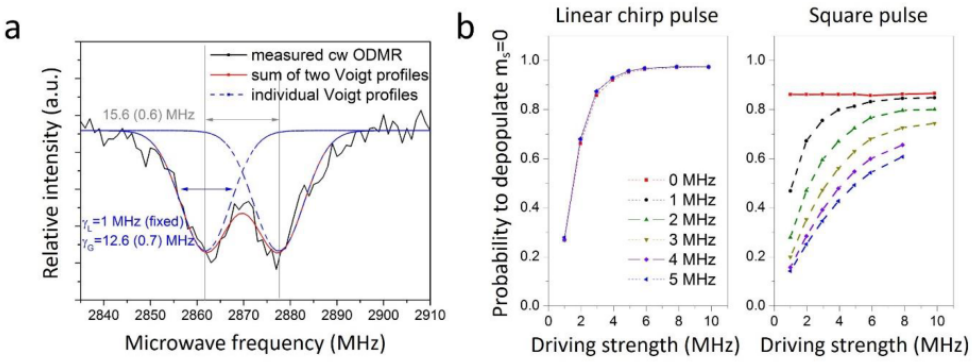

Supplementary Figure 10. Simulated NV spin flip probability induced by different pulse scheme. (**a**) A typical measured ODMR line for a randomly picked cluster of the ND-HPMA particles (black) excited with 45μW laser and weak microwave. The ODMR spectrum had been fitted by two Voigt profiles with a fixed Lorenzian linewidth of 1 MHz and a variable Gaussian linewidth (see below for used parameters). Both transitions in the measured ODMR line are quite broad and separated by around 16 MHz. (**b**) Simulated NV spin flip probability excited with a linear chirp pulse and square pulse plotted as a function of microwave driving strengths. The probability was calculated for an ensemble by averaging over all polar angle and assuming an inhomogeneous broadening of both ESR transitions with a variable value (color coded from 0 MHz (red) to 5MHz (blue)). Both transitions of ODMR line are set to split in average ~16 MHz to mimic the experimental situation in (**a**). The parameters of the chirp pulse had been set to typical values used under real experimental conditions (50 MHz sweep bandwidth with a 20 kHz ns^{-1} sweep speed).

Supplementary Methods

Chemical synthesis of Gd^{3+} complexes and diamond nanosensors

Chemicals and methods

3-Bromo-1-(trimethylsilyl)-1-propyne (**1**)[1], *t*Bu_3DO3A·HBr (**4**·HBr)[2], 1,6-bis(azido)-3,4-dithiahexane (**6**)[3], 10-({hydroxy[4-aminobenzyl]phosphoryl}methyl)-1,4,7,10-tetraazacyclododecane-1,4,7-triacetic acid (**7**)[4] and pent-4-ynehydrazide (**8**) (*via* methyl pent-4-ynoate[5]) were prepared according to published procedures. 6-Azido-hexan-2-one (**9**) was prepared analogously as published for related compounds[6]. Paraformaldehyde was filtered from aged aqueous formaldehyde solutions (Lachema) and dried in a desiccator over concentrated H_2SO_4. Other chemicals from commercial sources were used as received. Acetonitrile and dichloromethane were dried by distilling over P_4O_{10}.

NMR spectra were recorded on VNMRS300, Varian^{UNITY} INOVA 400 or Bruker Avance III 600 spectrometers. NMR chemical shifts are given in ppm, and coupling constants are reported in Hz. For ^1H and ^{13}C NMR measurements in D_2O, *t*BuOH was used as internal standard ($\delta_H = 1.25$, $\delta_C = 30.29$). For measurements in $CDCl_3$, TMS was used as internal standard ($\delta_H = 0.00$, $\delta_C = 0.00$). For ^{31}P NMR measurements, 85% aqueous H_3PO_4 was used as external reference ($\delta_P = 0.00$). The abbreviations s (singlet), d (dublet), t (triplet), m (multiplet) and br (broad) are used to express signal multiplicities.

Mass spectra were measured on a Bruker Esquire 3000 mass spectrometer with electrospray ionization with ion-trap detection in both positive and negative modes. Mass signals are provided with their relative abundance to the strongest one. For Gd^{3+} complexes, only the one containing the most abundant isotope is stated. HR MS spectra were recorded on an LTQ Velos Pro or Orbitrap ELITE mass spectrometer by Thermo.

HPLC measurements were performed on a ReproSil Gold C8 5 μm 150×4.6 mm column with a flow rate of 1 ml·min^{-1} using UV-absorption detection at 210 nm and 256 nm. The following methods with linear v/v gradients of water/acetonitrile were used: method **A**: 5% ACN to 90% ACN with 10 ppm v/v trifluoroacetic acid (TFA) in 5 min, then 90% ACN with 10 ppm v/v TFA for 5 min; method **B**: 0% ACN to 10% ACN with 5 ppm v/v TFA in 10 min, then 10% ACN to 25% ACN with 5 ppm v/v

Appendix E

TFA in 10 min, then 25% ACN to 95% ACN with 5 ppm v/v TFA in 10 min, then 95% ACN to 99% ACN with 1 ppm v/v TFA in 5 min; method **C**: 0% ACN to 10% in 10 min, then 10% ACN to 25% ACN in 10 min, then 25% ACN to 95% in 10 min, then 95% ACN to 99% ACN in 5 min.

Thin-layer chromatography (TLC) was performed on TLC aluminium sheets silica gel 60 F254 (Merck). UV light or dipping in 2% $KMnO_4$/10% Na_2CO_3 or 5% aqueous $CuSO_4$ were used for detection.

Elemental analyses were performed at the Institute of Macromolecular Chemistry (Academy of Sciences of the Czech Republic, Prague).

Synthesis of redox sensitive complex $[Gd(L^1)]^-$–SS–N_3

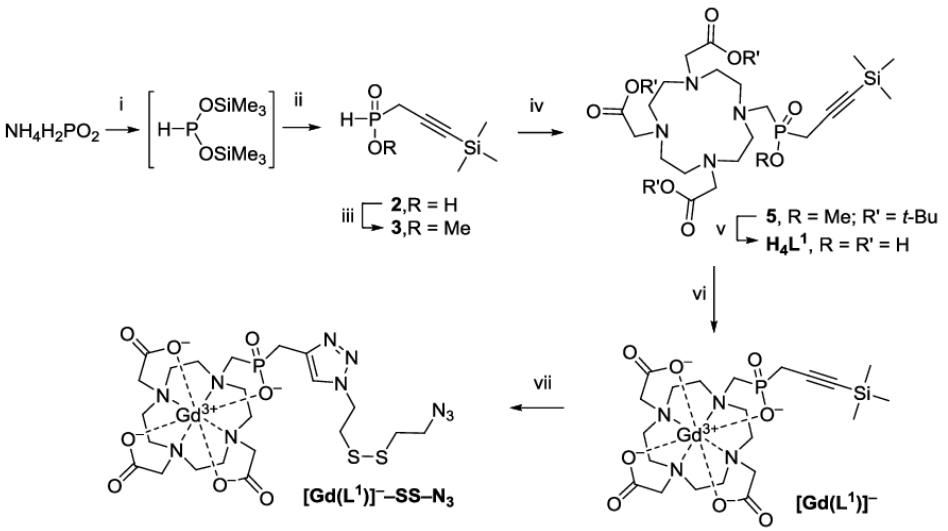

Reaction conditions and yields: i) Hexamethyldisilazane, under Ar, 105 °C, 12 h ii) 3-Bromo-1-(trimethylsilyl)-1-propyne (**1**)/CH_2Cl_2, under Ar, -10 °C to rt, 24 h, 54 % iii) methyl chloroformate, pyridine/CH_2Cl_2, reflux, 15 min, 97 % iv) *t*Bu_3DO3A·HBr (**4**·HBr), $(CH_2O)_n$/MeCN (dry), 65 °C, 3 days, ~90 % v) 1. 85% aq. HCOOH, 65 °C, 4 days, 2. 1,5% aq. HCl, rt, overnight, 78% vi) $GdCl_3 \cdot 5H_2O$/aq. NH_4OH, pH 4,8, rt, overnight, ~60 % vii) 1,6-bis(azido)-3,4-dithiahexane (**6**), $CuSO_4$, NaF, Sodium Ascorbate/ THF:*i*PrOH:H_2O (1:1:2), rt, 12 h, ~50%

3-(Trimethylsilyl)prop-2-ynylphosphinic acid (2)

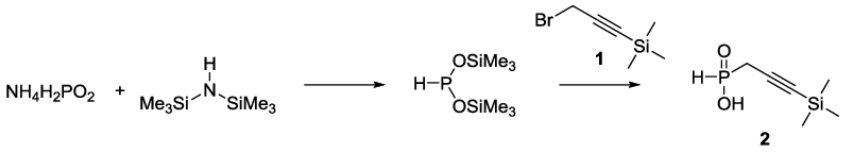

$NH_4H_2PO_2$ (5.0 g; 60 mmol) was securated in a 50 ml three-neck flask equipped with an argon inlet, a reflux condenser with vacuum trap and a septum. Hexamethyldisilazane (15 ml; 72 mmol) was added and the reaction mixture was stirred at 105 °C for 12 h under gentle flow of argon. In the course of the reaction, $NH_4H_2PO_2$ dissolved and ammonia evolved. The reaction mixture was then cooled to –10 °C and diluted with anhydrous dichloromethane (30 ml). Under an argon atmosphere, alkylation agent **1** (3.1 g; 16.2 mmol) was slowly added *via* syringe and the mixture was left to warm to RT under stirring. After 24 h, the reaction was terminated by addition of anhydrous EtOH (10 ml) and the reaction mixture was evaporated to dryness. The reaction mixture was co-evaporated two times with anhydrous EtOH (15 ml) and the remaining matter was dissolved in $CHCl_3$ (20 ml) and quickly washed with 3% HCl (2×20 ml). The combined aqueous phases were extracted with $CHCl_3$ (20 ml). The organic phases were combined, dried with Na_2SO_4 and volatiles were removed with rotary evaporator at 50 °C to yield (**2**) (1.54 g; 54 %) as a colorless oil.

The product contained ca 3% (by ^{31}P NMR) of bis(3-(trimethylsilyl)prop-2-ynyl)phosphinic acid, which does not react in the next step, and therefore, the crude **2** can be used without further purification. For analytic purposes, the compound **2** was purified by flash column chromatography on silica (EtOAc:MeOH = 5:4 v/v).

TLC: (EtOAc:MeOH = 5:4 v/v), R_f = 0.50, $KMnO_4$; ^1H NMR (299.94 MHz, $CDCl_3$): δ 0.17 (s, 9H, C*H*$_3$); 2.83 (dd, $^2J_{HP}$ = 20.1, $^3J_{HH}$ = 1.8, 2H, C*H*$_2$); 7.11 (d, $^1J_{HP}$ = 584, 1H, P–*H*); 10.9 (bs, O*H*); ^{13}C NMR (75.43 MHz, $CDCl_3$): δ –0,1 (s, *C*H$_3$); 24.6 (d, $^1J_{CP}$ = 84.5, *C*H$_2$); 86.8 (d, $^3J_{CP}$ = 7.5, C–*C*–Si); 99.4 (d, $^2J_{CP}$ = 8.7, P–C–*C*); ^{31}P NMR (121.42 MHz, $CDCl_3$): δ 27.8 (dt, $^1J_{HP}$ = 584, $^2J_{HP}$ = 20.0).

Appendix E

Methyl 3-(trimethylsilyl)prop-2-ynylphosphinate (3)

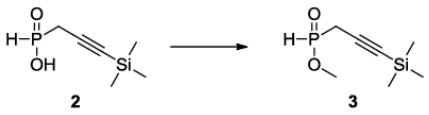

2 **3**

Phosphinic acid **2** (1.64 g; 9.31 mmol) was dried in a 100 ml flask by triple co-evaporation with anhydrous EtOH (5 ml). After evaporation, phosphinic acid was dissolved in anhydrous CH_2Cl_2 (19 ml), and methyl chloroformate (0.88 g; 9.31 mmol) was added. Anhydrous pyridine (0.74 g; 9.31 mmol) was added dropwise with stirring. After evolution of CO_2, the flask was equipped with a reflux condenser and the mixture was heated to reflux for 15 min. The reaction mixture was then cooled to RT and washed with 3% aqueous HCl (3×20 ml) and brine (20 ml). Combined aqueous phases were extracted with CH_2Cl_2 (2×20 ml) and organic phases were dried with Na_2SO_4, and solvent was removed with a rotary evaporator at 50 °C to yield methylester **3** (1.72 g; 97%) as a colorless liquid.

^{1}H NMR (299.94 MHz, $CDCl_3$): δ 0.12 (s, 9H, SiCH_3); 2.81 (d, $^2J_{HP}$ = 18.9, 2H, CH_2); 3.81 (d, $^3J_{HP}$ = 12.0, 3H, OCH_3); 7.16 (d, $^1J_{HP}$ = 585, 1H, P–*H*); ^{13}C NMR (75.43 MHz, $CDCl_3$): δ 0.3 (s, Si*C*H$_3$), 21.9 (d, $^1J_{CP}$ = 91.3, *C*H$_2$); 53.1 (d, $^2J_{CP}$ = 7.2, P–C–*C*); 89.9 (d, $^3J_{CP}$ = 8.5, C–*C*–Si); 93.4 (d, $^2J_{CP}$ = 10.9, O*C*H$_3$); ^{31}P NMR (121.42 MHz, $CDCl_3$): δ 31.5 (bd, $^1J_{HP}$ = 571.3).

Methyl ({4,7,10-tris[(*tert*-butyloxykarbonyl)methyl]-1,4,7,10-tetraazacyclododecane-1-yl}methyl)-3-(trimethylsilyl)prop-2-ynylphosphinate (5)

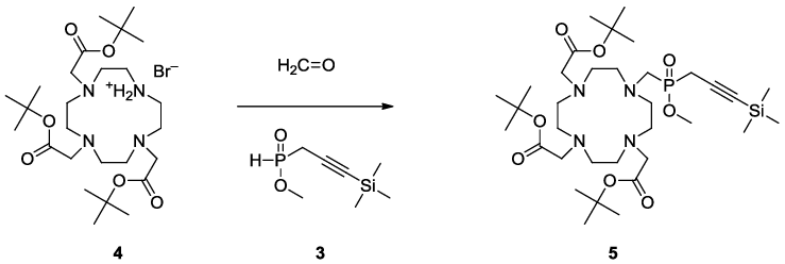

4 **3** **5**

*t*Bu$_3$DO3A·HBr (**4**·HBr, 1.000 g; 1.679 mmol) was placed into a 25 ml flask, and methyl ester **3** (336 mg; 1.763 mmol) and paraformaldehyde (53 mg; 1.763 mmol) were added under stirring. Anhydrous acetonitrile (10 ml) was then added, the flask was tightly closed, and the mixture was heated in an oil bath at 65 °C. The progress of the reaction was monitored with ^{31}P NMR spectra in 12-h intervals. A decrease in signal intensity of the starting compound **3** at 30 ppm (bd, $^{1}J_{HP}$ = 571 Hz) and increase in the product **5** signal at 43 ppm (s) was observed. In addition, approximately 3% of acid **2** was detected. Over time, the reaction mixture turned from a white suspension into pale brown clear solution. After 3 days, more than 95% of ester **3** had reacted, and solvent was removed with a rotary evaporator. The obtained oil was dissolved in minimal amount of hot MeOH, the solution was cooled, and the product was precipitated by addition of diethylether. The product **5** was collected by filtration (S3 frit), washed with diethylether (5 ml) and air-dried, affording 1.095 g (~90%) of off-white powder.

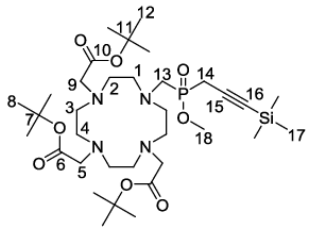

TLC: (EtOAc:EtOH:25% aq. NH_4OH = 60:33:7 v/v/v), R_f = 0.70, $KMnO_4$; ^{1}H NMR (299.94 MHz, $CDCl_3$): δ 0.07 (s, 9H, H-17); 1.40 (bs, 27H, H-8, H-12); 2.62 (d, $^{2}J_{HP}$ = 18.3, 2H, H-13); 2.60–3.60 (m, 24H, H-1-5, H-9, H-14); 3.75 (d, $^{3}J_{PH}$ = 10.8, 3H, H-18); ^{13}C NMR (75.43 MHz, $CDCl_3$): δ 0.1 (s, C-17); 23.2 (d, $^{1}J_{CP}$ = 84.8, C-14); 29.4 (s ,C-12); 30.6 (s, C-8); 51.2 (s, C-2); 51.8 (s, C-1,3); 52.2 (d, $^{2}J_{CP}$ = 97.8, C-13); 53.8 (s, C-4); 54.9 (s, C-9); 56.3 (s, C-5); 58.3 (d, $^{2}J_{CP}$ = 7.2, C-18); 84.6 (s, C-7); 86.1 (s, C-11); 92.1 (d, $^{3}J_{CP}$ = 8.9, C-16); 98.3 (d, $^{2}J_{CP}$ = 12.1, C-15); 170.2 (s, C-6); 174.2 (s, C-10); ^{31}P NMR (121.42 MHz, CD_3OD): δ 44.3 (bs); MS(+): 717.7 ($[M+H]^+$).

Appendix E

10-({Hydroxy[3-(trimethylsilyl)prop-2-ynyl]phosphoryl}methyl)-1,4,7,10-tetraazacyclododecane-1,4,7-triacetic acid (H_4L^1)

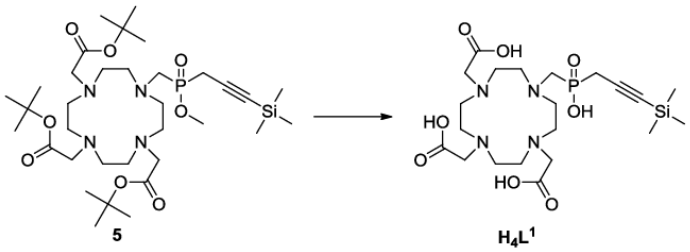

Compound **5** (1.000 g; 1.395 mmol) was dissolved in 85% formic acid (10 ml) in a 25-ml flask equipped with a magnetic stirring bar. The flask was closed, and the reaction mixture was heated in an oil bath at 65 °C for 4 days. Solvent was removed *in vacuo*, and the resulting oil was co-evaporated with water (3×5 ml) to remove the remaining formic acid. The obtained pale brown oil was dissolved in 1.5% aqueous HCl (10 ml) and stirred at RT overnight. Solvent was removed with a rotary evaporator. The resulting oil was dissolved in minimal amount of hot MeOH, the solution was cooled, and the product was precipitated by addition of diethylether. The product was collected by filtration on S3 frit, washed with diethylether (5 ml), dried in a vacuum and left to equilibrate at ambient conditions for three weeks. Product **H_4L^1** (0.694 g; 78%) was obtained as dihydrochloride sesquihydrate in form of an off-white powder.

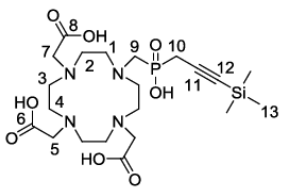

TLC: (EtOH:10% aq. AcOH = 8:2 v/v), R_f = 0.40; (EtOAc:EtOH:25% aq. NH_4OH = 60:33:7 v/v), R_f = 0.10, $CuSO_4$ or $KMnO_4$; ^{1}H NMR (299.94 MHz, D_2O): δ 0.07 (s, 9H, H-13), 2.64 (t, $^2J_{PH}$ = 18.6; 2H, H-10) 2.75–3.95 (bm, 24H; H-1-5, H-7, H-9); ^{13}C NMR (75.43 MHz, D_2O): δ 1.5 (s, C-13); 26.5 (d, $^1J_{CP}$ = 91.7; C-10); 50.5 (s, C-2); 51.6 (s, C-1,3); 51.8 (d, $^2J_{CP}$ = 98.3; C-9); 53.4 (s, C-4); 54.3 (s, C-7); 55.7 (s, C-5); 91.3 (d, $^3J_{CP}$ = 7.2, C-12); 102.8 (d, $^2J_{CP}$ = 10.5; C-11); 172.2 (s, C-6); 177.1 (s, C-8); ^{31}P

NMR (121.42 MHz, D_2O): δ 21.0–26.5 (br s); EA: calc. for $\mathbf{H_4L^1}\cdot 2HCl\cdot 1.5H_2O$, $C_{21}H_{44}Cl_2N_4O_{9.5}PSi$, M = 634.56: C 39.76; H 6.99; N 8.83; Cl 11.18; found: C 40.03; H 7.02; N 8.64; Cl 11.23; MS(+): 535.1 (51$[M+H]^+$); 557.1 (100$[M+Na]^+$); 573.1 (50$[M+K]^+$); MS(–): 532.9 (100$[M–H]^-$); 570.9 (21$[M+K–H]^+$).

(NH_4)[Gd($\mathbf{L^1}$)] complex

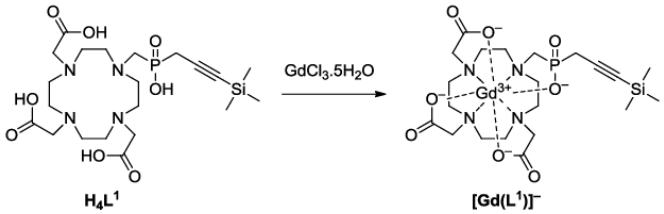

$GdCl_3\cdot 5H_2O$ (158 mg, 0.60 mmol) was added to a solution of $\mathbf{H_4L^1}$ (350 mg, 0.55 mmol) in water (10 ml) with stirring. The pH of the solution was adjusted to 4.8 with 5% aqueous NH_3 and the mixture was left at RT overnight. Solvent was then evaporated *in vacuo*, and the product was purified by reversed-phase chromatography (40 g YMC DispoPackAT 25-ODS cartridge) with a water–acetonitrile gradient and 10 ppm trifluoroacetic acid modifier. Fractions containing the product were collected and lyophilized to obtain (NH_4)[Gd($\mathbf{L^1}$)] (253 mg, ~60% yield) as a white powder.

MS(+): 712.1 (66[[Gd($\mathbf{L^1}$)]+H+Na]$^+$); 734.1 (100[[Gd($\mathbf{L^1}$)]+2Na]$^+$); 750.0 (97[[Gd($\mathbf{L^1}$)]+Na+K]$^+$); MS(–): 615.9 (15[[Gd($\mathbf{L^1}$)]–TMS]$^-$); 688.0 (100[Gd($\mathbf{L^1}$)]$^-$); HPLC: Program **A**: Retention time = 5.97 min.

Appendix E

Na[Gd($\mathbf{L^1}$)]–SS–N_3 complex

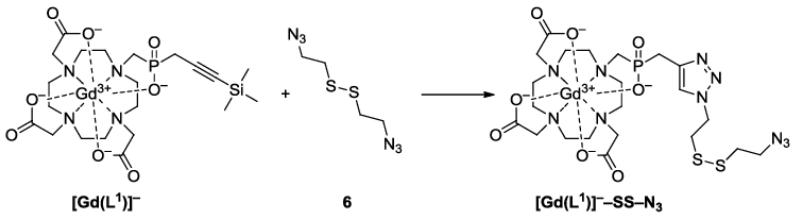

(NH_4)[Gd($\mathbf{L^1}$)] (250 mg, 0.36 mmol) was dissolved in a mixture of water (10 ml), *i*PrOH (5 ml) and THF (5 ml) in a 50-ml flask. Then 1,6-bis(azido)-3,4-dithiahexane (456 mg, 2.23 mmol), 1 M aqueous NaF (450 µl) and 1 M aqueous $CuSO_4$ (90 µl) were added, and the flask was sealed with a septum. Using a needle, a gentle stream of argon was passed through the reaction mixture for 3 min with sonication. Then, 1 M aqueous sodium ascorbate (225 µl) was added, and the reaction mixture was stirred for 12 h at RT under an argon atmosphere. The solvent was removed with a rotary evaporator, and the product was purified by reversed-phase chromatography (40 g YMC DispoPackAT 25-ODS cartridge) with a water–acetonitrile gradient and 10 ppm trifluoroacetic acid modifier. Fractions containing the product were collected and lyophilized to obtain Na[Gd($\mathbf{L^1}$)]–SS–N_3 (153 mg, approx. 50% yield) as a yellowish sticky solid.

MS(+): 822.2 ([[Gd($\mathbf{L^1}$)]–SS–N_3+2H]$^+$); MS(–): 819.1 ([[Gd($\mathbf{L^1}$)]–SS–N_3]$^-$); HRMS (ESI): calcd. for: $C_{33}H_{37}O_8N_{10}GdPS_2$ ([[Gd($\mathbf{L^1}$)]–SS–N_3+2H]$^+$): 822.12104; found: 822.12158; calcd. for: $C_{33}H_{36}O_{10}N_{10}GdNaPS_2$ ([[Gd($\mathbf{L^1}$)]–SS–N_3+H+Na]$^+$): 844.10298; found: 844.10355; HPLC: Program **B**: Retention time = 18.6 min.

Synthesis of pH sensitive complex $[Gd(L^2)]^-$–NHN–N_3

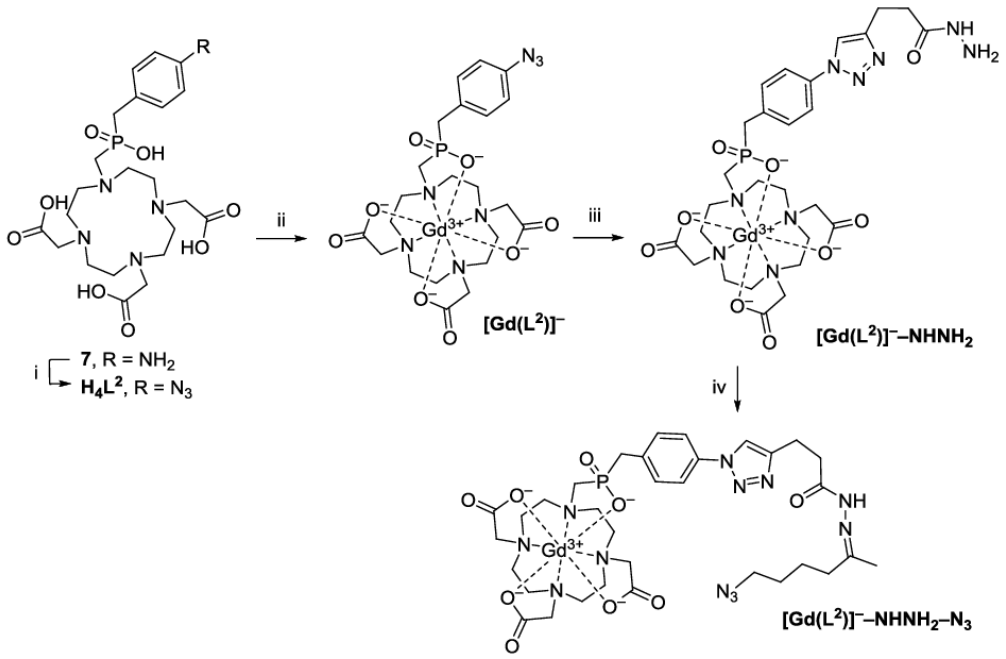

Reaction conditions and yields: i) 1. $NaNO_2$/aq. HCl 0 °C, 25 min; 2. NaN_3/aq. HCl 0 °C, 25 min, 70 % ii) $GdCl_3 \cdot 5H_2O$/aq. NH_4OH, pH 9, rt, overnight, ~70 % iii) pent-4-ynehydrazide (**8**), $CuSO_4$, Sodium Ascorbate/ THF:H_2O (1:1), rt, overnight, ~60 % iv) 6-azido-hexan-2-one (9), AcOH, $MgSO_4$/MeOH (dry), reflux, 3 days, ~30 %

10-({Hydroxy[4-azidobenzyl]phosphoryl}methyl)-1,4,7,10-tetraazacyclododecane-1,4,7-triacetic acid (H_4L^2)

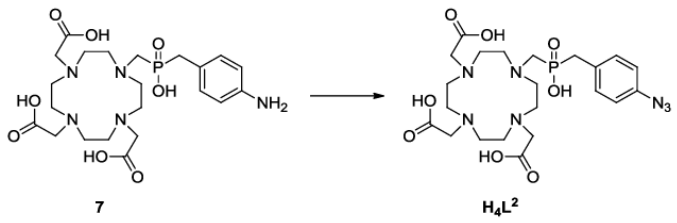

A solution of 10-({hydroxy[4-aminobenzyl]phosphoryl}methyl)-1,4,7,10-tetraazacyclododecane-1,4,7-triacetic acid tetrahydrochloride (**7**·4HCl, 653 mg; 0.97 mmol) in a mixture of deionized water (5 ml) and 6 M HCl (1 ml) in a 25-ml flask was cooled to 0 °C. Then, $NaNO_2$ (95 mg; 1.38 mmol) was slowly added, and the reaction mixture was stirred at 0 °C for 25 min. NaN_3 (104 mg; 1.60 mmol) was then slowly added, and the reaction mixture was stirred at 0 °C for another 25 min. The reaction

Appendix E

mixture was placed in a rotary evaporator and twice co-evaporated with water (3 ml) to remove excess HCl. The product was purified by reversed-phase chromatography (40 g YMC DispoPackAT 25-ODS cartridge) with a water–acetonitrile gradient and 10 ppm trifluoroacetic acid modifier. Fractions containing the product were collected, lyophilized and left for three weeks to equilibrate in ambient air in the dark to obtain (**H_4L^2**) (495 mg; 70% yield) as white powder, which turns brown when exposed to light.

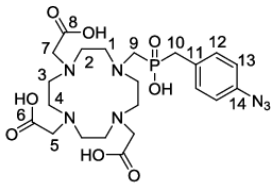

TLC: (EtOH:25% aq. NH_4OH = 8:2 v/v), R_f = 0.25, UV, $KMnO_4$ or $CuSO_4$; ^{1}H NMR (299.94 MHz, DMSO-d_6): δ 2.97–3.60 (bm, 24H; H-1-4, H-9, H-10); 3.64 (bm, 2H, H-5); 4.08 (bm, 4H, H-7); 7.03 (d, $^3J_{HH}$ = 7.9; 2H, H-13); 7.29 (d, J = 7.9 Hz, 2H, H-13); ^{13}C NMR (75.43 MHz, DMSO-d_6): δ 36.5 (d, $^1J_{CP}$ = 85.6; C-10); 49.9 (s, C-2); 50.8 (s, C-4); 51.3 (s, C-1); 50.6 (d, $^2J_{CP}$ = 105.1; C-9); 51.8 (s, C-3); 54.1 (s, C-5); 54.8 (s, C-7); 119.8 (d, $^4J_{CP}$ = 1.6; C-13); 130.2 (d, $^2J_{CP}$ = 10.0; C-11); 132.5 (d, $^3J_{CP}$ = 4.8; C-12); 138.3 (s, C-14); 170.1 (s, C-8); 172.6 (s, C-6); ^{31}P NMR (121.42 MHz, DMSO-d_6): δ 38.1 (s); EA: calc. for **H_4L^2**·3.4HCl·3H_2O, $C_{22}H_{43.4}Cl_{3.4}N_7O_{11}P$, M = 733.53: C 36.02; H 5.96; N 13.37, Cl 16.43; found: C 36.06; H 5.74; N 12.87, Cl 16.49; MS(+): 555.9 (100[M+H]$^+$); 577.9 (20[M+Na]$^+$); 593.9 (16[M+K]$^+$); MS(–): 553.7 ([M–H]$^-$); HPLC: Program **A**: Retention time = 5.79 min.

(NH_4)[Gd(L^2)] complex

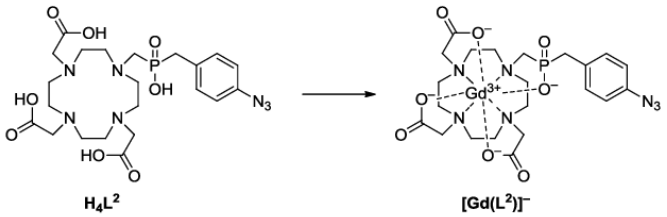

$GdCl_3 \cdot 5H_2O$ (126 mg, 0.49 mmol) was added to a solution of $\mathbf{H_4L^2}$ (300 mg, 0.41 mmol) in water (6 ml) with stirring. The pH of the solution was adjusted to 9.0 with 3% aqueous NH_4OH, and the mixture was left at RT overnight. The solvent was removed with a rotary evaporator, and the resulting solid was purified by flash chromatography (Buchi Sepacore® Silica 25 g cartridge) with an EtOH:25% aqueous NH_4OH (10:1 v/v) mobile phase. Fractions containing the product were collected and dried on a rotary evaporator. The product $(NH_4)[Gd(\mathbf{L^2})]$ (227 mg, ~70% yield) was obtained after lyophilization from water (10 ml) as a pale powder that turns dark when exposed to light.

TLC: (EtOH:25% aq. NH_4OH = 5:1 v/v), R_f = 0.65, UV, $KMnO_4$; MS(–):707.4 $(Gd(\mathbf{L^2})]^-$); HPLC: Program **A**: Retention time = 5.69 min.

$(NH_4)[Gd(L^2)]^-$–$NHNH_2$ complex

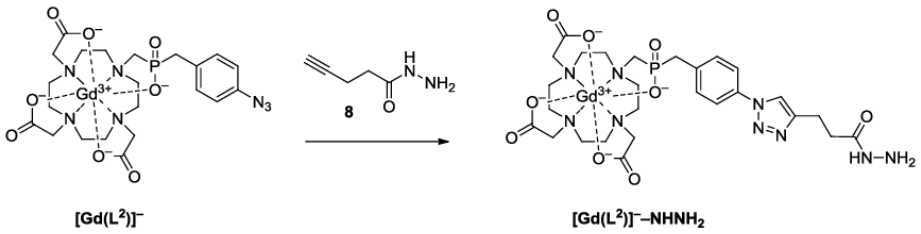

$(NH_4)[Gd(\mathbf{L^2})]$ (203 mg; 0.28 mmol) and pent-4-ynehydrazide **8** (62 mg, 0.55 mmol) were dissolved in a mixture of water (1.5 ml) and THF (1.5 ml) in a 4-ml vial equipped with a septum and magnetic stirring bar. Then, 1 M aqueous $CuSO_4$ (32 μl) was added, and the mixture was bubbled under a brisk stream of argon for 3 min. Subsequently 1 M aqueous sodium ascorbate (100 μl) was added, and the solution was stirred at RT overnight in the dark. The solvent was removed with a rotary evaporator, and the resulting solid was purified with reversed-phase chromatography (40 g YMC DispoPackAT 25-ODS cartridge) with a water–acetonitrile gradient and 10 ppm trifluoroacetic acid modifier. Fractions containing the product were collected and lyophilized to obtain $(NH_4)[Gd(\mathbf{L^2})]$–$NHNH_2$ (154 mg, ~60% yield).

Appendix E

MS(+): 821.5 (33[[Gd(**L**^{2})]–NHNH$_2$+2H]$^+$); 844.6 (66[[Gd(**L**^{2})]–NHNH$_2$+H+Na]$^+$); 866.6 (100[[Gd(**L**^{2})]–NHNH$_2$+H+K]$^+$); MS(–): 820.5 ([[Gd(**L**^{2})]–NHNH$_2$–H]$^-$); HPLC: Program **B**: Retention time = 10.5 min.

(NH$_4$)[Gd(L^2)]–NHN–N$_3$ complex

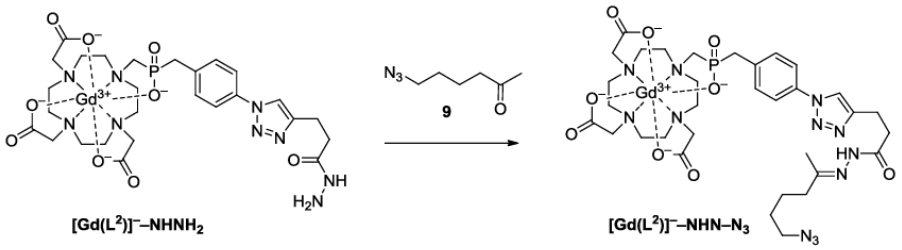

(NH$_4$)[Gd(**L**^{2})]–NHNH$_2$ (100 mg; 0.12 mmol) and 6-azido-hexan-2-one **9** (137 mg; 0.97 mmol) were dissolved in anhydrous MeOH (8 ml) in a 25-ml flask equipped with a reflux condenser with a chlorcalcium tube. Glacial acetic acid (22 mg; 0.37 mmol) and anhydrous MgSO$_4$ (1.00 g; 8.33 mmol) were added, and the reaction mixture was heated to reflux under chlorcalcium tube for 3 days. The solvent was removed with a rotary evaporator, and the resulting solid was purified with reversed-phase chromatography (40 g YMC DispoPackAT 25-ODS cartridge) with a water–acetonitrile gradient. Fractions containing the product were combined and lyophilized to obtain **(NH$_4$)[Gd(L^2)]–NHN–N$_3$** (33 mg, ~30% yield).

MS(–): 944.3 ([M–H]$^-$); HRMS (ESI): calcd. for: C$_{33}$H$_{47}$O$_9$N$_{12}$GdP ([[Gd(**L**^{2})]–NHN–N$_3$]$^-$): 944.25731; found: 944.25711; HPLC: Program **C**: Retention time = 18.9 min.

Preparation of ND-HPMA-Gd conjugates

Nanodiamonds (NDs) (MSY 0–0.05, Microdiamant, Switzerland) were oxidized by air in a furnace at 510 °C for 4 h; treated with a mixture of HF and HNO$_3$ (2:1) at 160 °C for 2 days; and washed with water, 1 M NaOH, 1 M HCl and water. Purified ND powder was irradiated in an external target holder for 21 hours with a 16.6 MeV electron beam (1.25×10^{19} particles cm^{-2}) from an MT-25 microtron.

The irradiated material was annealed at 900 °C for 1 h and subsequently oxidized for 4 h at 510 °C. The resulting powder was again treated with a mixture of acids and washed with NaOH, HCl and water, providing a colloidal solution of ND-COOH.

Poly(vinylpyrrolidone) (MW = 10,000, 136 mg) was dissolved in water (120 ml) and sonicated for 10 min in an ultrasonic bath. ND-COOH colloid (24 ml, 2 mg ml^{-1}, filtered using a 0.4 μm GMF filter) was added, and the mixture was stirred for 24 h. The colloid was then concentrated by centrifugation. NDs (in approximately 3 ml solvent) were resuspended in ethanol (48 ml). Tetraethyl orthosilicate (360 μl) and 3-(trimethoxysilyl)propylmethacrylate (120 μl) were added, and the mixture was sonicated for 20 s in an ultrasonic bath. Ammonia (25%, 2 ml) then was added. The reaction mixture was stirred for 14 h. The product was purified by centrifugation, washed with methanol and transferred to 0.3 ml of DMSO using a rotary evaporator. (2-Hydroxypropyl)methacrylamide (HPMA) (735 mg), N-propargyl acrylamide (315 mg) and 2,2-azobis(2-methylpropionitrile) (AIBN, 300 mg) were dissolved in DMSO (3 ml). The mixture was filtered using a 0.4 μm glass microfiber microfilter. Methacrylate-terminated NDs (48 mg) dispersed in 0.3 ml DMSO were added. The reaction proceeded for 3 days under argon at 55 °C. The particles were purified by centrifugation with methanol. Alkyne-modified HPMA-coated NDs were decorated with azide-modified Gd^{3+} complexes using Cu(I)-catalyzed azide-alkyne cycloaddition (CuACC). HPMA-coated NDs (10 mg in a final reaction volume of 12.8 ml 50 mM HEPES buffer, pH 7.4) were mixed with non-cleavable Gd^{3+} complex (**NH_4[Gd(L^2)]**), cleavable Gd complex with hydrazone (**NH_4[Gd(L^2)]–NHN–N_3**) or a disulfide linker (**Na[Gd(L^1)]–SS–N_3**) in final concentrations of 0.96, 1.92 and 2.4 mM, respectively, pre-mixed 0.32 mM $CuSO_4$ and 0.64 mM tris(3-hydroxypropyltriazolylmethyl)amine (THPTA) ligand and a freshly prepared solution of sodium ascorbate (5 mM). The reaction mixture was well-sealed, left for 1 h with no stirring and washed by centrifugation with water (Gd^{3+} conjugates with non-cleavable, ND-HPMA-Gd, and disulfide, ND@redox, linkers) or methanol (Gd^{3+} conjugates with hydrazone linker, ND@pH). The resulting nanosensors were stored in water (ND-HPMA-Gd and ND@redox) or in dry methanol (ND@pH) at 4 °C.

Appendix E

Characterization of ND-polymer-Gd nanosensors

The stability and surface charge of HPMA-coated NDs with Gd^{3+} complexes were tested in solutions later used for further experiments: 50 mM citric acid (pH 2.0), 50 mM acetate buffer (pH 4.5), 50 mM HEPES buffer (pH 7.4), 50 mM TRIS buffer (pH 8.5) and 10× concentrated PBS. Dynamic light scattering (DLS) and zeta potential were recorded with a Zetasizer Nano ZS system (Malvern Instruments) at 37 °C. Sample concentrations were 0.1 mg ml^{-1}.

To prepare the samples for transmission electron microscopy (TEM), carbon-coated copper grids were placed into a UV-ozonizing chamber (UV/Ozone Pro Cleaner Plus, Bioforce Nanosciences) for 15 min. Then, a droplet of jetPEI (Polyplus tranfection, cat no. 101-10) was placed on the grid. After 10 min incubation, it was removed with a piece of tissue. Then, a droplet of aqueous solution of NDs (0.05 mg ml^{-1}) was placed on the grid, and after 3 min incubation, liquid was removed with a piece of tissue. TEM pictures were captured using a JEOL JEM-1011 electron microscope operated at 80 kV.

Total amounts of Gd^{3+} complexes conjugated to HPMA-coated NDs were estimated using inductively coupled plasma atomic emission spectroscopy (ICP AES). The analysis was performed using a Spectro Arcos SOP ICP AES spectrometer, power 1450 W, sample flow 2 ml min^{-1}.

Kinetics of release of Gd^{3+} complex from the conjugate

ND@pH: A 5-µl aliquot of NDs colloid (20 mg ml^{-1} in water) was diluted with 95 µl buffer (either 50 mM citrate, pH 2.0; 50 mM acetate, pH 4.5 or 50 mM HEPES, pH 7.4). The mixture was incubated for a certain time (30 s, 1, 2, 4 and 60 min for pH 2.0; 2.5, 5, 10, 20, 40 min and 8 h for pH 4.5; and 2, 6, 12 and 24 hours for pH 7.4) at 37 °C. The cleavage reaction was then stopped by addition of HEPES buffer (300 mM, pH 8.0) to the mixture (100 µl for pH 2.0, 20 µl for pH 4.5). NDs were centrifuged (10 min 55,000 rcf, 4 °C), and the supernatant was removed and diluted with 2% HNO_3 for ICP MS measurements. A control representing time 0 s was set up with the opposite order of mixing: first, the NDs colloid was diluted in HEPES buffer, then cleavage buffer (acidic conditions) was added. The non-cleavable ND-HPMA-Gd conjugate was used as a control at the 0, 15, 30, 45 and

60 minutes and processed under the same conditions. All samples were prepared in duplicate. Concentrations of Gd^{3+} complexes in solutions were analyzed in duplicate (performed with two independent samples, where each was measured twice (4 results)) using an ICP MS 7700 (Agilent Technologies) instrument.

ND@redox: A 5-µl aliquot of NDs colloid (20 mg ml^{-1} in water) was diluted with 95 µl buffer (50 mM HEPES buffer, pH 7.4, or 50 mM TRIS, pH 8.5). A solution of glutathione (final concentrations of 1, 5 and 10 mM) was added. The mixture was incubated for a certain time (2, 5, 10, 30 and 60 min) at 37 °C under inert conditions. The cleavage reaction was then stopped by addition of 6-maleimidohexanoic acid (diluted in 10% DMSO in 0.5 M phosphate buffer, pH 7.0, final concentration 100 mM). NDs were centrifuged (10 min 55,000 rcf, 4 °C), and the supernatant was removed and diluted with 2% HNO_3 for ICP MS measurements. A control representing time 0 s was set up with the opposite order of mixing: 6-maleimidohexanoic acid was first added to NDs colloid diluted in buffer and then glutathione was added. The non-cleavable ND-HPMA-Gd conjugate was used as a control at the 0, 15, 30, 45 and 60 minutes and processed under the same conditions. All samples were prepared in duplicate. Concentrations of Gd^{3+} complexes in solutions were analyzed in duplicate (performed with two independent samples, where each was measured twice (4 results)) using an ICP MS 7700 (Agilent Technologies) instrument.

Preparation of Britton-Robinson buffers (measurements in Supplementary Figure 8)

Britton-Robinson buffers (with equal composition and ionic strength) were prepared according to the established procedure: 0.5 M Britton-Robinson buffer at pH 3.29 was prepared (by mixing 0.0667 g of NaOH, 0.0664 ml CH_3COOH, 0.114 ml H_3PO_4, 0.103 g H_3BO_3 and 1.729 g KCl). For T_1 measurements, stock buffer was diluted to 50 mM concentration and pH was adjusted to required pH (3.8, 4.5, 5.5, 6.2 and 6.9) by NaOH. The conductivity of all solutions was adjusted to the same value (6.40 mS) by addition of KCl.

Theoretical model of NV relaxometry influenced by the release of Gd^{3+} complex

The total NV relaxation rate is:

Appendix E

$$\Gamma_{total} = \Gamma_{int} + \Gamma_{external} \quad (1)$$

The intrinsic decay rate Γ_{int} is attributed to spin noise (impurities) in the diamond lattice like Orbach or Raman process[7]. The external part $\Gamma_{external}$ is attributed to the randomly distributed Gd^{3+} complex locating in the polymer shell surrounding ND, and can be written as[8]:

$$\Gamma_{extrernal} = 3g_{NV}\mu_B \sum_i \frac{g_i\mu_i}{\hbar^2} < B_i^2 > \frac{\tau_{c_i}}{1+\omega_0^2{\tau_{c_i}}^2} \quad (2)$$

Where g_i is the g-factor, μ_i the magneton and τ_{c_i} is the typical correlation time of the spin species with index i.

As in equation (1) the decay rates just sum up, we can also combine several decay channels that are kept constant over time. We therefore consider the sample ND-HPMA (without Gd^{3+} complex) has an intrinsic relaxation time, and add another decay channel induced by Gd^{3+} for other samples (with Gd^{3+} complex).

Starting with a spin S_j placed at the distance r_j to the NV to derive an expression for $< B_i^2 >$, the spin creates a time fluctuating magnetic field B_j at the position of the NV:

$$\mathbf{B_j} = \frac{\mu_0}{4\pi}\mathbf{g_j}\mu_j \cdot \frac{1}{r_j^3}\left(\mathbf{S_j} - \frac{3(\mathbf{S_j}\cdot\mathbf{r_j})\cdot\mathbf{r_j}}{r_j^2}\right) \quad (3)$$

Weak magnetic field components along the NV quantization axis (z) only lead to a detuning off the NV resonance, but don't introduce a change in the spin level populations, as the x and y components will do. Therefore we can neglect the z-component of the B field:

$$B_{\perp,j}^{\ 2} = < B_{x,j}^2 > + < B_{y,j}^2 > \quad (4)$$

We assume the spin to be in a purely mixed state. Its density matrix ρ can be written as:

$$\rho = \frac{1}{2S+1}\mathbf{E}_{2S+1} \quad (5)$$

Than $B_{\perp,j}^{\ 2}$ can be expressed as:

Appendix E

$$B_{\perp_j}^{\ 2} = Tr\left(\rho B_{x,j}^2\right) + Tr\left(\rho B_{y,j}^2\right) = \left(\frac{\mu_0}{4\pi} g_e \mu_B\right)^2 \cdot C_s \cdot \frac{2+3\sin^2(\alpha_j)}{r_j^6} \quad (6a)$$

with:

$$C_s = \frac{1}{2S+1}\sum_{m=-S}^{S} m^2 = \frac{S(S+1)}{3} \quad (6b)$$

In the following we consider spins randomly distributed in a layer with thickness δd and the volume density of σ_i on the surface of a spherical diamond with diameter d_o. The total magnetic field experienced by the NV center for all spin species can then be summarized in spherical coordinates:

$$< B_i^2 >= \sum_j B_{\perp,j}^2 = \left(\frac{\mu_0}{4\pi} g_i \mu_i\right)^2 \cdot C_s \cdot \sigma_i \int_{\frac{d_0}{2}}^{\frac{d_0}{2}+\delta d} dr' \int_0^{2\pi} d\phi \int_0^{\pi} d\theta \sin\theta \frac{2+3\sin^2(\alpha(\theta,\phi))}{r(r',\delta r,\theta,\phi)^4} \quad (7a)$$

With:

$$\sin^2\alpha = \sin^2\theta \quad (7b)$$

And

$$r = \sqrt{r'^2 - \delta r^2 \sin^2\theta} + \delta r\cos\theta \quad (7c)$$

When moving δr from the center of a spherical shaped nanodiamond along the NV spin quantization axis (parallel to the NV axis).

If the NV is moved on a path perpendicular to its quantization axis, then $\sin^2\alpha$ and r have the following expression[8]:

$$\sin^2\alpha = \cos^2\theta + \sin^2\theta\sin^2\phi \quad (7d)$$

And

$$r = \sqrt{r'^2 - \delta r^2 \sin^2\theta} + \delta r\cos\theta \quad (7e)$$

The total fluctuation rate of the Gd^{3+} complex is $R = 1/\tau_c = R_{dip} + R_{vib}$ where R_{dip} is due to the inter bath dipolar coupling while R_{vib} is caused by intrinsic vibrational spin relaxation of the Gd^{3+}

Appendix E

complex in solution. In current study, we adapted the typical value of $R_{vib} = 50\ GHz$ for Gd^{3+} complex[9].

In the following, we calculate the R_{dip}:

The spin-spin interaction of two spins k and l can be describe by the following Hamiltonian:

$$\mathbf{H_{kl}} = \frac{\mu_0}{4\pi} \mathbf{g_k \mu_k \cdot g_l \mu_l} \frac{1}{\mathbf{r_{kl}^3}} \left(\mathbf{S_k S_l} - \frac{3(\mathbf{S_k \cdot r_{kl}}) \cdot (\mathbf{S_l \cdot r_{kl}})}{\mathbf{r_{kl}^2}} \right) \tag{8}$$

And is connected to the interaction rate $R_{dip} = \mathbf{1}/\tau_c^{dip}$ with:

$$\hbar R_{dip} = \sqrt{\sum_{k \neq l} < H_{kl}^2 >} \tag{9}$$

By using (8) one finds[8]:

$$< H_{kl}^2 > = \left(\frac{\mu_0}{4\pi} \mathbf{g_k \mu_k \cdot g_l \mu_l} \right)^2 \cdot 6 C_s^2 \cdot \frac{1}{r_{kl}^6} \tag{10}$$

Spins in a thick layer:

For a layer with height of δd consisting of spins with the density σ we use the following approximation:

$$\sum_{k \neq l} \frac{1}{r_{kl}^6} \approx \sigma \int_0^{2\pi} d\phi \int_{d_{min}}^{\delta d - d_{min}} dz \int_{r_{min}}^{\infty} dr \, \frac{r}{(r^2+z^2)^3} = 2\pi\sigma \int_{d_{min}}^{\delta d - d_{min}} dz \int_{r_{min}}^{\infty} dr \, \frac{r}{(r^2+z^2)^3}$$

(11a)

Where $d_{\min}$ and r_{min} accounts for the minimal distance between neighbor spins since the spins later can't be infinitesimally dense packed. Now assuming homogeneous distributed spins each caged in a sphere with radius of r_s, we make the following approach for a thick layer: $d_{min} \approx r_{min} \approx \frac{1}{\sqrt{2}} \cdot r_s$ and $\delta d \gg r_s$.

Spins in the center of the layer will have more neighbors to interact then spins directly at the surface. As an approximation we modify Equation (11a) by average over all possible positions:

$$\sum_{k\neq l}\frac{1}{r_{kl}^6}\approx\frac{\sigma}{\delta d-2d_{min}}\int_0^{\delta d-2d_{min}}dh\int_{-h}^{\delta d-2d_{min}-h}dz\int_0^{2\pi}d\phi\int_{r_{min}}^{\infty}dr\,\frac{r}{(r^2+z^2)^3} \quad (11b)$$

$$\sum_{k\neq l}\frac{1}{r_{kl}^6}\approx 2\pi\sigma\cdot\frac{\pi}{2\sqrt{2}r_s^3}\approx 7\cdot\frac{\sigma}{r_s^3} \quad (11c)$$

And the average spin-spin interaction rate of a spin bath in a thick layer can be approximated by:

$$R_{dip}^{layer}\approx 0.5157\cdot\mu_0\cdot\frac{g^2\cdot\mu^2}{\hbar}\cdot C_s\cdot\sqrt{\frac{\sigma}{r_s^3}} \quad (12)$$

Supplementary Discussion

NV spin population readout in NDs

The charge state of the NV centers can be influenced by various quantities, such as the local environments, surface treatment of the diamond, excitation wavelength of laser and etc.[10,11,12,13]. In particular, the charge state of NV centers in NDs is highly depending on the surface passivation due to their high surface to volume ratio[12]. In addition, their charge state can adjust over time without illumination, and also differs under laser illumination. As a consequence, the NV centers can change their charge state on the time scale of several μs to ms, depending on the used laser power and wavelength[13], which can be directly observed as an increase or decrease of the NV fluorescence after turning on the laser[10]. A typical single T_1 measurement containing no additional control sequence will contain that information, diminishing the measured spin contrast significantly. If one now applies a second measurement (control), i.e., by an additional microwave pulse (e.g., square or linear chirp pulse) before read out, the NV sublevel population is inverted and the spin contrast can be calculated. In other words, one can extract the pristine spin contrast by subtracting the normalized T_1 measurement from the control[14].

Simulation of NV spin sublevel flip induced by microwave excitation

We simulated the evolution of the spin-state using the NV spin Hamiltonian[15,16] by applying a linear polarized microwave excitation along the x-direction of the NV reference frame, while its z-

direction is along the NV rotational symmetry axis. We introduced the desired broadening as a Zeeman-like term, which would be introduced by a magnetic field aligned along the NV quantization axis. Both transitions are split by the "Zeeman-like term" around 16 MHz (see Supplementary Fig. 10). In this scenario we only have to consider the angular dependence of the microwave excitation field versus the NV quantitation axis. To simplify the simulated model, we also intentionally discard the Zero field parameter E that is accounting for strain in the NDs crystal. After averaging over all possible angular orientations of the microwave driving field, we extract the average probability to flip NV sublevel.

Inhomogeneous ODMR linewidth broadening in NDs

From Hahn-echo measurements on a well dispersed NDs sample we estimated an average T_2 time around ~1μs (data not shown) for single to few NVs in an individual diamond nanocrystal. This is a typical value for NDs[17,18,19]. The corresponding natural line width of one ODMR line would be around several hundreds of kHz, and therefore cannot be the origin of the observed line-broadening (Supplementary Fig. 10a). Another possible broadening by laser excitation could be ruled out by checking its laser power dependent behaviors (data not shown). Therefore, we attribute the observed inhomogeneous ODMR line broadening to the variations of strain among different diamond nanocrystals[20,21]. In addition, a weak residual static magnetic field, e.g., the earth magnetic field, may also partially account for such splitting and broadening.

Supplementary References

1. Schaefer, M., Hanik, N. & Kilbinger, A. F. M. ROMP Copolymers for Orthogonal Click Functionalizations. *Macromolecules* **45**, 6807–6818 (2012).

2. Moore, D. A. Selective Trialkylation of Cyclen with tert-Butyl Bromoacetate. *Org. Synth.* 10–14 (2008).

3. Wang, Y. *et al.* Reduction-Degradable Linear Cationic Polymers as Gene Carriers Prepared by Cu(I)-Catalyzed Azide−Alkyne Cycloaddition. *Biomacromolecules* **12**, 66–74 (2011).

4. Rudovský, J. *et al.* Synthesis of a bifunctional monophosphinic acid DOTA analogue ligand and its lanthanide(III) complexes. A gadolinium(III) complex endowed with an optimal water exchange rate for MRI applications. *Org. Biomol. Chem.* **3**, 112–117 (2005).

5. Gilchrist, T. L., Wasson, R. C., King, F. D. & Wootton, G. Intramolecular cycloaddition of azoalkenes derived from terminal alkenoic and alkynoic acids. *J. Chem. Soc. Perkin Trans. 1*, 2511–2516 (1987).

6. Yau, H. M., Croft, A. K. & Harper, J. B. Investigating the origin of entropy-derived rate accelerations in ionic liquids. *Faraday Discuss.* **154**, 365–371 (2011).

7. Jarmola, A., Acosta, V. M., Jensen, K., Chemerisov, S. & Budker, D. Temperature- and magnetic-field-dependent longitudinal spin relaxation in nitrogen-vacancy ensembles in diamond. *Phys. Rev. Lett.* **108**, 197601 (2012).

8. Tetienne, J. P. et al. Spin relaxometry of single nitrogen-vacancy defects in diamond nanocrystals for magnetic noise sensing. *Phys. Rev. B* **87**, 235436 (2013).

9. Caravan P., Ellison J. J., McMurry T. J. & Lauffer R. B. Gadolinium(III) Chelates as MRI Contrast Agents: Structure, Dynamics, and Applications. *Chem. Rev.* **99**, 2293 – 2352 (1999).

10. Gaebel T, et al. Photochromism in single nitrogen-vacancy defect in diamond. *Appl. Phys. B* **82**, 243-246 (2006).

11. Hauf M, et al. Chemical control of the charge state of nitrogen-vacancy centers in diamond. *Phys. Rev. B* **83**, 081304 (2011).

12. Petráková V, et al. Luminescence of nanodiamond driven by atomic functionalization: towards novel detection principles. *Adv. Funct. Mater.* **22**, 812-819 (2012).

Appendix E

13. Aslam N, Waldherr G, Neumann P, Jelezko F, Wrachtrup J. Photo-induced ionization dynamics of the nitrogen vacancy defect in diamond investigated by single-shot charge state detection. *New J. Phys.* **15**, 013064 (2013).

14. Häberle T, Schmid-Lorch D, Reinhard F, Wrachtrup J. Nanoscale nuclear magnetic imaging with chemical contrast. *Nat. Nanotechnol.* **10**, 125-128 (2015).

15. Michl J, et al. Perfect alignment and preferential orientation of nitrogen-vacancy centers during chemical vapor deposition diamond growth on (111) surfaces. *Appl. Phys. Lett.* **104**, 102407 (2014).

16. Alegre TPM, Santori C, Medeiros-Ribeiro G, Beausoleil RG. Polarization-selective excitation of nitrogen vacancy centers in diamond. *Phys. Rev. B* **76**, 165205 (2007).

17. Tisler J, et al. Fluorescence and spin properties of defects in single digit nanodiamonds. *ACS Nano* **3**, 1959-1965 (2009).

18. Laraoui A, Hodges JS, Meriles CA. Nitrogen-vacancy-assisted magnetometry of paramagnetic centers in an individual diamond nanocrystal. *Nano Lett.* **12**, 3477-3482 (2012).

19. Trusheim ME, et al. Scalable fabrication of high purity diamond nanocrystals with long-spin-coherence nitrogen vacancy centers. *Nano Lett.* **14**, 32-36 (2013).

20. Bradac C, et al. Observation and control of blinking nitrogen-vacancy centres in discrete nanodiamonds. *Nat. Nanotechnol.* **5**, 345-349 (2010).

21. McGuinness L, et al. Quantum measurement and orientation tracking of fluorescent nanodiamonds inside living cells. *Nat. Nanotechnol.* **6**, 358-363 (2011).

Appendix F

Zemek, O.; Notni, J.; Kossatz. S. Syntéza ligandu odvozeného od PIDAZTA s pnutým cykloalkynem (dosud nepublikováno).

Appendix F

PIDAZTA-A-DBCO synthesis report

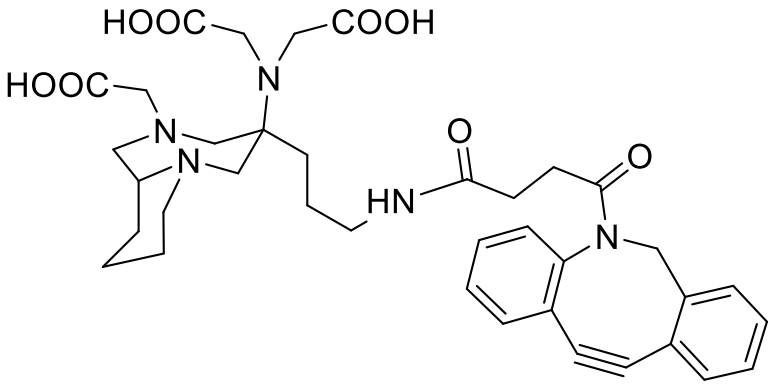

Discussion

N-(4-Bromobutyl)phthalimide was prepared from phthalimide *via* alkylation with excess of 1,4-dibromobutane to suppress formation of diphthalimide product[1]. Bromo- derivative was converted to Iodo- with Finkelstein reaction[2], to enhance reactivity in next step, and used without purification. Reaction with $NaNO_2$ in DMSO was chosen for substitution of iodo- to nitro- group. While it provided lower yields of (**I.**) than procedures described in literature[3,4] using $AgNO_2$ it uses much cheaper and readily available reagent. N-(Phenylmethyl)-2-piperidinemethanamine (**II.**) was prepared via reductive amination from racemic 2-aminomethylpiperidine according to[5] and reacted with N-(4-Nitrobutyl)phthalimide (**I.**) to obtain mixture of two enantiomeric pairs (**III.a**) and (**III.b**). While these diastereomers was firstly separated with chromatography (Hexane/Ethyl acetate) on silica gel column, it was found that desired (4R,10*R) + (4S,10*S) (**III.b**) enantiomeric pair partially crystalizes from solution of both products. Absolute configuration was determined with single-crystal X-ray diffraction analysis of both isomers. Only (4R,10*R) + (4S,10*S) (**III.b**) diastereomer was used in following reactions while retention of configuration was assumed. Catalytic hydrogenation provided reduction of nitro to amino group and debenzylation in one step. Presence of diluted HCl in reaction mixture was found to speed up reaction and drive it to completion. Resulting amine (**IV.**) was directly alkylated with excess of *t*-butyl bromoacetate and the product (**V.**) was purified with flash chromatography. In next step, phthalimide protective group was removed with hydrazine and free amine (**VI.**) separated with preparative HPLC chromatography.

Firstly, DBCO acid was coupled directly to this *t*-butyl ester derivative, but subsequent trials to remove *t*-butyl protective group failed. Various conditions were tried (trifluoroacetic acid neat or diluted, with radical scavengers like TIPS, formic acid of various concentrations) but satisfactory deprotection was not achieved. Instead, DBCO moiety detached invariably. While some literature[6,7] claims successful *t*-butyl ester deprotection with preservation of DBCO in molecule, our observation corresponded to lit.[8,9] where DBCO rearranges to strain-promoted azide–alkyne cycloaddition (SPAAC) nonreactive tetracyclic compound.

To address this problem, *t*-butyl esters was cleaved first from deprotected amine (tBu_3-PIDAZTA-A-NH_2) (**VI.**) to form free ligand (PIDAZTA-A-NH_2) (**VII.**) and subsequent reaction with active NHS ester of DBCO acid (**VIII.**) provided target compound (PIDAZTA-A-DBCO) (**IX.**).

Appendix F

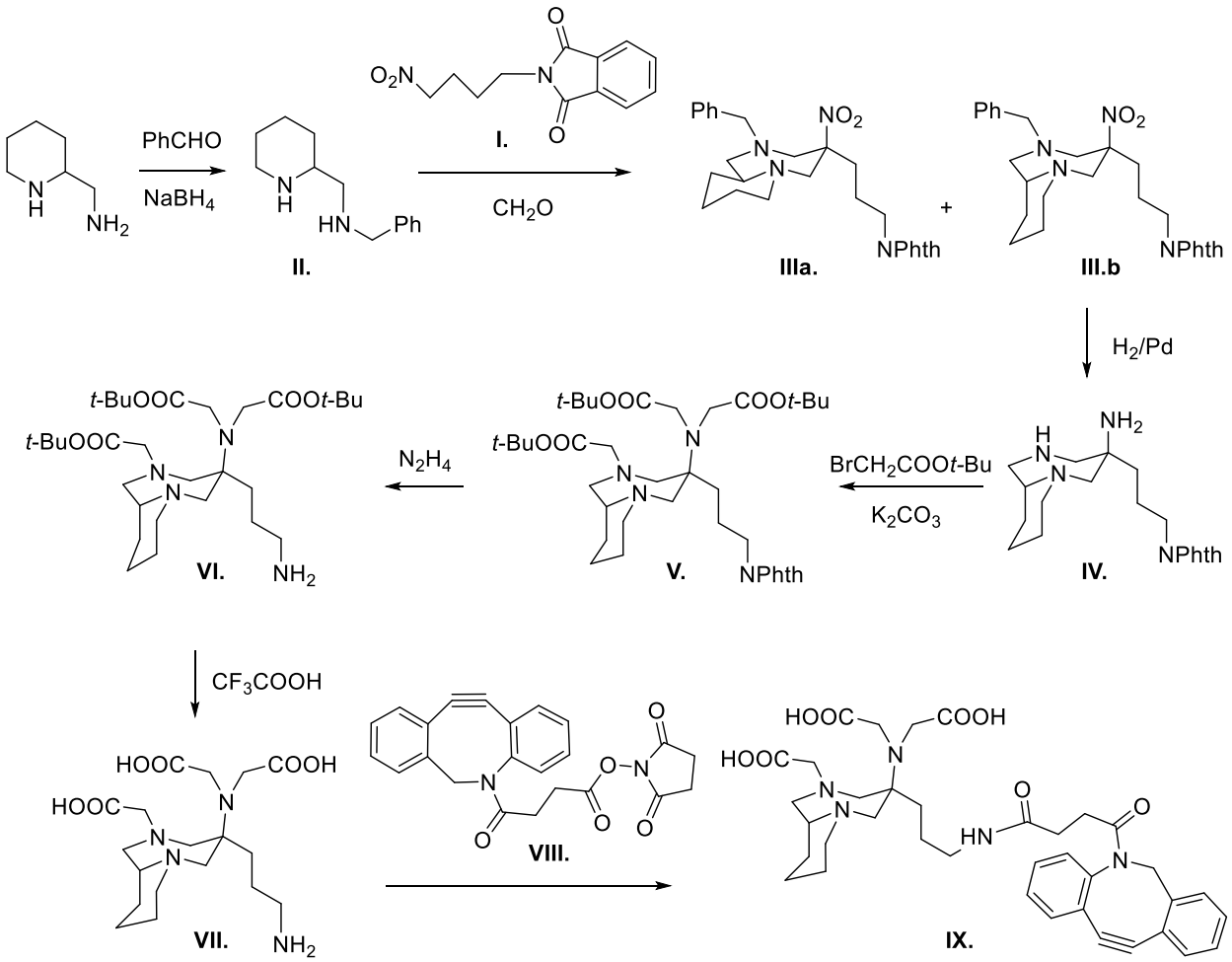
PhCHO
NaBH4
II.
I.
CH2O
IIIa.
III.b
H2/Pd
IV.
BrCH2COOt-Bu
K2CO3
V.
N2H4
VI.
CF3COOH
VII.
VIII.
IX.

Experimental

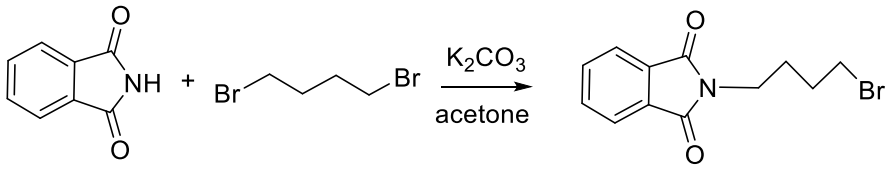

N-(4-Bromobutyl)phthalimide: Phtalimide (20 g; 136 mmol), K_2CO_3 (50 g; 362 mmol) were dissolved in acetone (250 ml). 1,4-dibromobutane (87 g; 403 mmol) was added and the reaction mixture was stirred under reflux and checked periodically with TLC. After 12 h the reaction was completed, inorganic salts were filtered off and filtrate was evaporated on rotary vacuum evaporator (RVE) (70 °C, 8 torr). Resulting product was recrystallized from Ethyl Acetate/Hexane and 34.5 g (90 % yield) of white crystalline product was obtained.

^{1}H NMR (400 MHz, Chloroform-*d*) δ 7.96 – 7.80 (m, 2H), 7.79 – 7.62 (m, 1H), 3.75 (t, $^3J_{HH}$ = 6.7 Hz, 2H), 3.46 (t, ^{3}JHH = 6.4 Hz, 2H), 2.01 – 1.79 (m, 4H).
^{13}C NMR (101 MHz, $CDCl_3$) δ 168.38, 134.01, 132.06, 123.28, 36.97, 32.79, 29.85, 27.26.

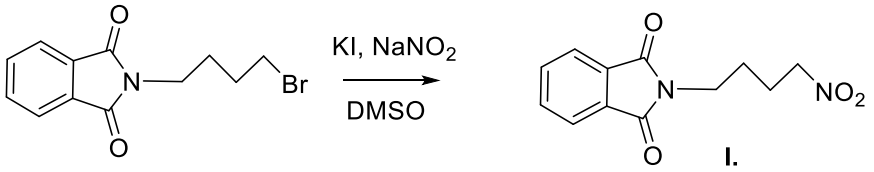

I.

N-(4-Nitrobutyl)phthalimide (I.): 4-bromobutylenphtalimide (34.5 g, 122 mmol) and KI (30 g, 181 mmol) were dissolved in acetone (200 ml) and heated under reflux for 11 hours. Then, inorganic solid was filtered off and solvent was evaporated on RVE. Resulting solid was dissolved in DMSO (200 ml), $NaNO_2$ (8.5 g, 123 mmol) was added and the solution was stirred at 30 °C for 15 hours. Reaction mixture was then diluted with water (500 ml) and extracted three times with ethyl acetate (3 x 150 ml). Joined organic fractions were washed with brine (2 x 100 ml), dried over $MgSO_4$ and evaporated on RVE. Thus obtained residue (about 25 g) was separated on silica gel chromatography with Hexane/Ethyl acetate gradient mobile phase. Fractions containing product were joined, evaporated and resulting white solid was recrystallized from hot MeOH. Product N-(4-Nitrobutyl)phthalimide (**I.**) (10.1 g, 40.7 mmol) was obtained as white crystals in 33.5 % yield.

^{1}H NMR (400 MHz, Chloroform-*d*) δ 7.75 (td, *J* = 5.3, 2.1 Hz, 2H), 7.70 – 7.61 (m, 2H), 4.41 (t, *J* = 6.9 Hz, 2H), 3.68 (t, *J* = 6.9 Hz, 2H), 2.14 – 1.89 (m, 2H), 1.84 – 1.65 (m, 2H).
^{13}C NMR (101 MHz, $CDCl_3$) δ 168.24, 134.08, 131.87, 123.23, 74.78, 36.71, 25.32, 24.48.

Appendix F

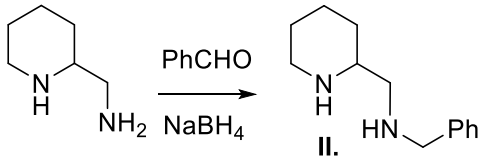

N-(Phenylmethyl)-2-piperidinemethanamine (II.): Racemic 2-aminomethylpiperidine (10.2 g, 89.3 mmol) was dissolved in dichloromethane (DCM) (30 ml) and solution of benzaldehyde (10.4 g, 98 mmol) in DCM (10 ml) was added slowly. The reaction mixture heated spontaneously and turned turbid. Anhydrous Na_2SO_4 (7 g, 49 mmol) was added to the solution and the mixture was stirred at 20 °C for 1.5 hours. Then, inorganic salt was filtered off and solution was evaporated on RVE. Resulting yellow oil (about 19 g) was dissolved in methanol (30 ml) and $NaBH_4$ (3.5 g, 92.6 mmol) was added during 30 minutes that resulted in intensive foaming. Methanol (10 ml) was added and the reaction mixture was stirred at 20 °C for 5 hours before more methanol (30 ml) was added and the reaction mixture was stirred under reflux for 1.5 hours. Then, reaction mixture was cooled down and excess of concentrated HCl (25 ml) was slowly added before the solution was evaporated on RVE (50 °C, 8 torr). Obtained residue was dissolved in 3% HCl (50 ml) and washed twice with DCM (25 ml), water phase was basified with NaOH (25 g) and extracted with DCM (3 x 30 ml). Joined organic fractions were dried with Na_2SO_4 and evaporated to obtain product (**II.**) as viscous pale yellow oil (17.0 g, 83 mmol) that solidifies to white mass during few days in fridge.

^{1}H NMR (400 MHz, Chloroform-*d*) δ 7.32 (s, 1H), 7.31 (s, 2H), 7.24 (ddd, *J* = 8.7, 5.1, 3.7 Hz, 1H), 3.78 (d, *J* = 2.6 Hz, 2H), 3.14 – 3.02 (m, 1H), 2.72 – 2.46 (m, 4H), 1.91 (s, 2H), 1.84 – 1.72 (m, 1H), 1.59 (dddt, *J* = 13.1, 8.1, 4.6, 2.2 Hz, 2H), 1.50 – 1.26 (m, 2H), 1.12 (tdd, *J* = 12.4, 10.4, 3.8 Hz, 1H).
^{13}C NMR (101 MHz, $CDCl_3$) δ 140.62, 128.36, 128.06, 126.87, 56.67, 55.38, 54.19, 46.79, 30.85, 26.59, 24.67.

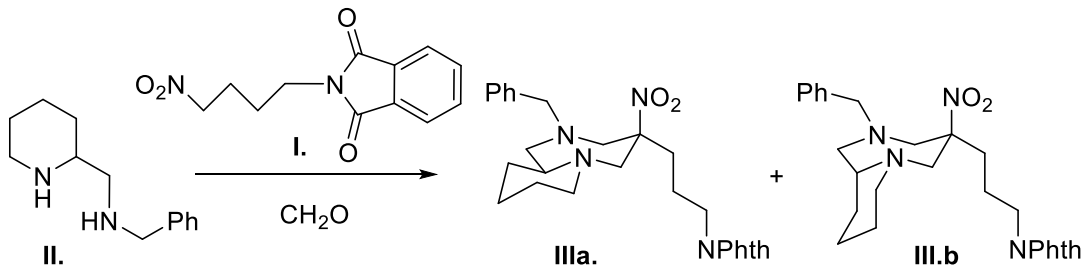

N-(Phenylmethyl)-2-piperidinemethanamine (**II.**) (8.0 g, 39 mmol), N-(4-Nitrobutyl)phthalimide (**I.**) (10.0 g, 40 mmol) and paraformaldehyde (4.0 g, 133 mmol) were dissolved in 1:1 mixture of toluene and ethanol (240 ml) and stirred at 60 °C while progress of the reaction was checked periodically with TLC. After 20 hours the reaction was completed, solvent was evaporated on RVE and the residue dissolved in ethyl acetate (100 ml) was filtered over short plug of silica. Filtrate was evaporated on RVE and obtained residue was dissolved in minimal volume of hot 1:1 mixture of methanol and ethyl acetate and left overnight to crystalize. Crystals were filtered off, washed with cold methanol and dried under vacuum to obtain wanted (4R, 10a*R) (**III.b**) diastereomer (3.8 g). After recrystallization from hot methanol product (3.4 g, 6.9 mmol) was obtained as colourless crystals in 17 % yield. To unambiguously determine chirality of both isomers, small portion of reaction mixture was separated

on flash chromatography silica gel column with Hexane/ethyl acetate (8:2). Each of separated isomers was crystalized from MeOH to obtain single-crystal suitable for X-ray diffraction analysis.

(**III.a**) (4R, 10a*S)

^{1}H NMR (400 MHz, Chloroform-*d*) δ 7.81 (dd, *J* = 5.5, 3.1 Hz, 2H), 7.70 (dd, *J* = 5.4, 3.1 Hz, 2H), 7.31 – 7.26 (m, 4H), 7.23 (p, *J* = 4.1 Hz, 1H), 3.67 (d, *J* = 13.0 Hz, 1H), 3.54 (d, *J* = 13.0 Hz, 1H), 3.44 (td, *J* = 6.8, 1.9 Hz, 2H), 3.26 (dd, *J* = 14.3, 6.7 Hz, 2H), 2.96 (t, *J* = 15.0 Hz, 2H), 2.89 – 2.74 (m, 2H), 2.38 – 2.25 (m, 1H), 2.19 (t, *J* = 11.7 Hz, 1H), 2.12 (s, 1H), 1.77 – 1.65 (m, 1H), 1.64 – 1.56 (m, 2H), 1.56 – 1.46 (m, 1H), 1.44 – 1.28 (m, 4H), 1.19 – 1.02 (m, 2H).
^{13}C NMR (101 MHz, $CDCl_3$) δ 168.18, 139.11, 133.99, 131.93, 129.14, 128.35, 127.32, 123.25, 93.67, 66.75, 64.58, 64.22, 63.81, 59.88, 57.66, 37.34, 34.54, 30.74, 25.97, 23.46, 22.49.
TLC (Hexane/ethyl acetate; 8:2) R_f : 0.42

MS (ESI): m/z$[M+H]^+$ = 477.4

(**III.b**) (4R, 10a*R)

^{1}H NMR (400 MHz, Chloroform-*d*) δ 7.86 (dd, *J* = 5.4, 3.1 Hz, 2H), 7.74 (dd, *J* = 5.5, 3.0 Hz, 2H), 7.32 – 7.19 (m, 5H), 3.74 (d, *J* = 13.3 Hz, 1H), 3.67 (t, *J* = 7.1 Hz, 3H), 3.57 (d, *J* = 13.3 Hz, 1H), 3.42 (d, *J* = 13.7 Hz, 1H), 2.88 – 2.65 (m, 4H), 2.39 – 2.25 (m, 1H), 2.20 – 2.11 (m, 1H), 2.11 – 1.90 (m, 3H), 1.77 – 1.60 (m, 1H), 1.60 – 1.46 (m, 2H), 1.40 – 1.25 (m, 3H), 1.21 – 1.07 (m, 1H), 1.06 – 0.93 (m, 1H).
^{13}C NMR (101 MHz, $CDCl_3$) δ 168.26, 139.26, 134.02, 132.02, 128.69, 128.23, 127.12, 123.29, 94.35, 65.35, 64.40, 63.35, 61.60, 58.59, 37.52, 33.80, 30.53, 26.01, 23.49, 22.73.

TLC (Hexane/ethyl acetate; 8:2) R_f :0.38

MS (ESI): m/z$[M+H]^+$ = 477.4

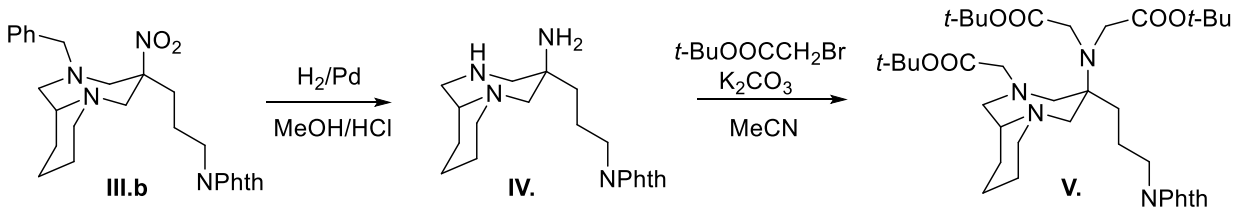

Nitro- derivative (**III.b**) (3.4 g, 6.9 mmol) was dissolved in autoclave in mixture of MeOH (50 ml) and 3% HCl (15 ml). 10% Pd@C (500 mg) was added, the vessel was pressurized to 9 atmospheres with hydrogen and the mixture was vigorously stirred at laboratory temperature for 3 days while progress of the reaction was checked with HPLC-MS and the pressure was kept at 9 atmospheres. After completion of the reaction Pd@C was filtered off and the solution was evaporated on RVE and the resulting residue was directly used in alkylation. The residue was dissolved in acetonitrile (50 ml), K_2CO_3 (8.0 g, 58 mmol) and *t*-butyl bromoacetate (5.0 g, 26 mmol) were added and the reaction mixture was stirred at 50 °C while periodically checked with HPLC-MS. After 3 days while the reaction was still not completed, more *t*-butyl bromoacetate (1.5 g, 7.7 mmol) and K_2CO_3 (2.0 g, 14.5 mmol) was added and the reaction was completed in next 2 days. Reaction mixture was filtered and evaporated on RVE and the resulting residue was separated with flash chromatography on silica gel column with CH_2Cl_2/MeOH/(28% aq.) NH_4OH 10:1:0.1 v/v mobile phase. Fractions containing pure

product, as detected with HPLC-MS, were joined and evaporated to obtain product (**V.**) (1.26 g, 1.8 mmol) as pale yellow oil.

^{1}H NMR (300 MHz, Chloroform-*d*) δ 7.84 (ddd, *J* = 5.5, 3.0, 1.2 Hz, 2H), 7.77 – 7.61 (m, 2H), 3.81 – 3.57 (m, 4H), 3.46 (d, *J* = 17.4 Hz, 2H), 3.20 (s, 2H), 2.92 (t, *J* = 12.7 Hz, 2H), 2.80 – 2.59 (m, 3H), 2.39 – 2.24 (m, 1H), 2.10 (d, *J* = 13.8 Hz, 3H), 1.76 (dd, *J* = 25.4, 10.9 Hz, 2H), 1.59 (d, *J* = 11.3 Hz, 1H), 1.46 (s, 9H), 1.45 – 1.40 (m, 18H), 1.38 – 1.01 (m, 6H), 0.94 (dd, *J* = 36.9, 9.9 Hz, 1H).
^{13}C NMR (101 MHz, $CDCl_3$) δ 169.35, 168.37, 134.05, 131.95, 123.30, 82.70, 63.60, 62.49, 60.90, 60.20, 59.26, 55.85, 53.16, 49.97, 37.84, 32.54, 28.33, 28.15, 27.98, 24.16, 22.43, 21.40, 19.22.

MS (ESI): m/z$[M+H]^+$ = 699.4

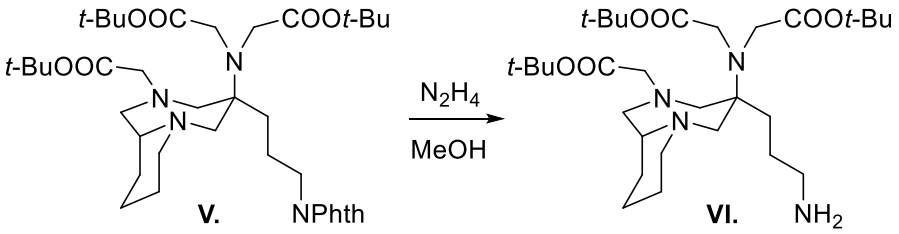

tBu_3-PIDAZTA-A-NH_2: Phthalimide derivative (600 mg, 0.86 mmol) was dissolved in MeOH (15 ml) and $N_2H_4 \cdot H_2O$ (64 mg, 1.28 mmol) was added. Reaction mixture was heated under reflux for 3 h. Then, solvent was evaporated on RVE and the residue was dissolved in CH_2Cl_2 (10 ml), insoluble hydrazine phthalimide was filtered off and washed with CH_2Cl_2 (5 ml). Joined organic parts were evaporated and thus obtained product was purified with preparative HPLC on C18 column (Luna 5µm 100Å 250 x 21.5 mm) with H_2O/MeCN (0.1% trifluoroacetic acid as modifier) gradient (35-85 %) mobile phase. Product (**VI.**) (410 mg, 0.46 mmol) was obtained as pale yellow glassy solid after lyophilisation of joined fractions with pure product.

^{1}H NMR (600 MHz, Chloroform-*d*) δ 8.33 (s, 3H), 3.63 (t, *J* = 19.8 Hz, 2H), 3.53 – 3.38 (m, 3H), 3.34 (d, *J* = 12.2 Hz, 2H), 3.25 (s, 2H), 3.19 (d, *J* = 14.0 Hz, 1H), 3.08 (dd, *J* = 15.7, 6.4 Hz, 2H), 2.94 (dd, *J* = 27.9, 15.0 Hz, 3H), 2.77 (t, *J* = 13.2 Hz, 1H), 1.94 (d, *J* = 13.1 Hz, 1H), 1.87 – 1.82 (m, 3H), 1.77 – 1.69 (m, 2H), 1.69 – 1.59 (m, 3H), 1.47 (s, 27H).
^{13}C NMR (151 MHz, $CDCl_3$) δ 169.36, 82.79, 82.65, 82.48, 63.12, 62.34, 60.70, 60.51, 59.09, 55.93, 52.46, 50.12, 39.84, 31.77, 28.10, 27.96, 23.94, 21.60, 21.22, 19.15.

Elemental analysis for $C_{30}H_{56}N_4O_6 \cdot 2.75$ TFA $\cdot 0.5$ H_2O – found: C-47.72 %; H-6.72 %; N-6.25 %

– calculated: C-47.83 %; H-6.76 %; N-6.29 %

MS (ESI): m/z$[M+H]^+$ = 569.2

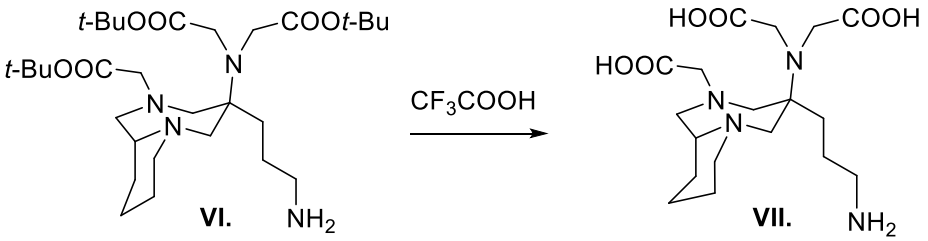

PIDAZTA-A-NH$_2$: *t*-butyl ester derivative (**VI.**) (250 mg, 0.28 mmol) was dissolved in cleavage mixture (3 ml) of trifluoroacetic acid/CH_2Cl_2/triisopropyl silane/H_2O 85:10:2.5:2.5 v/v and stirred at laboratory temperature overnight. Reaction mixture was then evaporated on RVE to dryness and five times dissolved in water (3 ml) and evaporated to dryness on RVE. Product (197 mg, 0.27 mmol) was obtained after lyophilisation from water (3 ml) as almost colourless glassy solid.

^{1}H NMR (600 MHz, D_2O) δ 3.76 (bs, 3H), 3.65 (s, 1H), 3.62 (s, 1H), 3.46 – 3.38 (m, 4H), 3.31 (d, *J* = 8.6 Hz, 2H), 3.20 (d, *J* = 14.8 Hz, 1H), 3.14 (dd, *J* = 15.4, 6.6 Hz, 1H), 3.02 (d, *J* = 14.5 Hz, 1H), 2.82 (t, *J* = 7.7 Hz, 2H), 2.76 (d, *J* = 14.8 Hz, 1H), 2.60 (dd, *J* = 15.5, 10.8 Hz, 1H), 1.81 (dq, *J* = 14.7, 7.6, 6.9 Hz, 1H), 1.78 – 1.74 (m, 2H), 1.71 – 1.66 (m, 1H), 1.65 – 1.56 (m, 1H), 1.50 (ddd, *J* = 12.6, 10.1, 7.7 Hz, 1H), 1.48 – 1.41 (m, 1H), 1.42 – 1.36 (m, 1H), 1.31 (dd, *J* = 9.9, 7.0 Hz, 2H).
^{13}C NMR (151 MHz, D_2O) δ 174.88, 174.85, 63.04, 62.25, 60.19, 58.74, 58.71, 55.23, 52.34, 39.44, 31.37, 23.53, 21.00, 20.89, 18.85.

Elemental analysis for $C_{18}H_{32}N_4O_6 \cdot 2.7\ TFA \cdot 0.5\ H_2O$ – found: C-39.13 %; H-5.06 %; N-7.84 %

– calculated: C-39.18 %; H-5.02 %; N-7.81 %

MS (ESI): m/z$[M+H]^+$ = 401.3

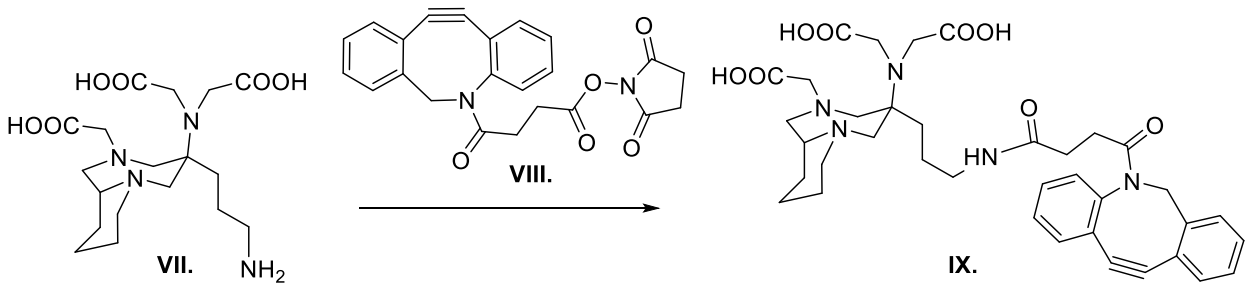

PIDAZTA-A-DBCO: 11,12-Didehydro-γ-oxodibenz[b,f]azocine-5(6H)-butanoic acid (DBCO acid) (91.5 mg, 0.30 mmol) was dissolved in CH_2Cl_2 (4 ml), N-hydroxysukcinimide (NHS) (34.5 mg, 0.30 mmol) and 1-Ethyl-3-(3-dimethylaminopropyl)carbodiimide (EDC) (60 mg, 0.39 mmol) was added and the reaction mixture was stirred at laboratory temperature for 4 hours. Then, reaction mixture was washed three times with brine (3 x 3 ml), dried with Na_2SO_4 and evaporated on RVE at 30 °C. White microcrystalline powder (115 mg) thus obtained was >98 % pure 2,5-Dioxo-1-pyrrolidinyl 11,12-didehydro-γ-oxodibenz[b,f]azocine-5(6H)-butanoate (**VIII.**) (DBCO–NHS) according to HPLC-MS and was used without further purification.
PIDAZTA-A-NH$_2$ 2.7 TFA ·0.5 H_2O (**VII.**) (120 mg, 0.17 mmol) was dissolved in DMSO (4 ml) with DBCO-NHS (**VIII.**) (80 mg, 0.20 mmol) freshly prepared as stated above and Et_3N (200 µl, 1.43 mmol). Reaction mixture was stirred for 3 hours and then evaporated on RVE (30 °C, 5 torr). Thus obtained

residue was dissolved in MeCN/H_2O 1:2 mixture (5 ml) and lyophilized overnight. Resulting solid was subjected to preparative HPLC on C18 column (Luna 5µm 100Å 250 x 21.5 mm) with H_2O/MeCN (0.1% trifluoroacetic acid as modifier) gradient (35-90 %) and fractions containing pure product according to HPLC-MS were joined and lyophilized. Product (**IX.**) (45 mg, 0.05 mmol) was obtained as fine white powder.

^{1}H NMR (400 MHz, Methanol-d_4) δ 7.67 (dt, J = 7.3, 2.3 Hz, 1H), 7.62 (ddt, J = 5.7, 4.5, 2.4 Hz, 1H), 7.51 – 7.45 (m, 3H), 7.41 – 7.32 (m, 2H), 7.27 (dd, J = 7.1, 1.9 Hz, 1H), 5.16 (dd, J = 14.0, 2.2 Hz, 1H), 3.81 (s, 2H), 3.73 (d, J = 14.0 Hz, 1H), 3.68 – 3.52 (m, 2H), 3.53 – 3.45 (m, 2H), 3.45 – 3.35 (m, 3H), 3.27 – 3.15 (m, 2H), 3.09 (d, J = 14.0 Hz, 2H), 3.00 (d, J = 6.5 Hz, 1H), 2.86 (d, J = 14.8 Hz, 1H), 2.81 – 2.66 (m, 2H), 2.35 (dtd, J = 15.2, 7.5, 4.9 Hz, 1H), 2.15 (dtd, J = 15.0, 7.3, 5.9 Hz, 1H), 1.97 (ddt, J = 16.4, 7.0, 5.8 Hz, 1H), 1.85 (d, J = 16.5 Hz, 2H), 1.80 – 1.71 (m, 2H), 1.71 – 1.60 (m, 1H), 1.53 (d, J = 14.4 Hz, 2H), 1.43 – 1.30 (m, 2H), 1.26 (dd, J = 11.7, 8.2 Hz, 2H).
^{13}C NMR (101 MHz, MeOD) δ 173.07, 173.05, 172.77, 151.28, 148.07, 132.04, 132.02, 129.20, 129.18, 128.60, 128.28, 127.78, 127.49, 126.72, 125.07, 122.99, 122.33, 114.16, 107.36, 63.28, 62.52, 60.12, 58.85, 58.62, 55.33, 54.96, 52.43, 39.10, 32.27, 30.47, 30.44, 29.84, 29.78, 23.59, 22.67, 21.31, 19.08.

Elemental analysis for $C_{37}H_{45}N_5O_8 \cdot 2.1$ TFA $\cdot 0.4$ H_2O – found: C-52.90 %; H-5.16 %; N-7.56 %

– calculated: C-52.96 %; H-5.17 %; N-7.49 %

MS (ESI): m/z$[M+H]^+$ = 688.2

References

1. Sestito, S. *et al.* Design and synthesis of H2S-donor hybrids: A new treatment for Alzheimer's disease? *Eur. J. Med. Chem.* **184**, 111745 (2019).
2. Gama, S. *et al.* Synthesis and Biological Studies of Pyrazolyl-Diamine PtII Complexes Containing Polyaromatic DNA-Binding Groups. *ChemBioChem* **13**, 2352–2362 (2012).
3. Keller-Schierlein, W., Mertens, P., Prelog, V. & Walser, A. Stoffwechselprodukte von Mikroorganismen 49. Mitteilung. Die Ferrioxamine A1, A2 und D2. *Helv. Chim. Acta* **48**, 710–723 (1965).
4. The First Conversion of Primary Alkyl Halides to Nitroalkanes under Aqueous Medium | The Journal of Organic Chemistry. https://pubs.acs.org/doi/10.1021/jo049048b.
5. Farkas, E. *et al.* PIDAZTA: Structurally Constrained Chelators for the Efficient Formation of Stable Gallium-68 Complexes at Physiological pH. *Chem. – Eur. J.* **25**, 10698–10709 (2019).
6. Wang, X., Gobbo, P., Suchy, M., S. Workentin, M. & E. Hudson, R. H. Peptide-decorated gold nanoparticles via strain-promoted azide–alkyne cycloaddition and post assembly deprotection. *RSC Adv.* **4**, 43087–43091 (2014).
7. Beck, S. *et al.* Site-Specific DBCO Modification of DEC205 Antibody for Polymer Conjugation. *Polymers* **10**, 141 (2018).
8. Shi, W. *et al.* Manipulating the Click Reactivity of Dibenzoazacyclooctynes: From Azide Click Component to Caged Acylation Reagent by Silver Catalysis. *Angew. Chem. Int. Ed.* **59**, 19940–19944 (2020).
9. Rearrangements and addition reactions of biarylazacyclooctynones and the implications to copper-free click chemistry - Organic & Biomolecular Chemistry (RSC Publishing). https://pubs.rsc.org/en/content/articlelanding/2013/ob/c3ob40683k#!divAbstract.